3-1-2013

Thermal and Electrical Transport in Ferromagnetic Metal Thin Films

Azure D. Avery
University of Denver

THERMAL AND ELECTRICAL TRANSPORT IN FERROMAGNETIC METAL THIN FILMS

A Dissertation

Presented to

the Faculty of Natural Sciences and Mathematics

University of Denver

In Partial Fulfillment

of the Requirements for the Degree

Doctor of Philosophy

---

by

Azure D. Avery

March 2013

Advisor: Professor Barry L. Zink

Author: Azure D. Avery
Title: Thermal and Electrical Transport in Ferromagnetic Metal Thin Films
Advisor: Professor Barry L. Zink
Degree Date: March 2013

Abstract

The recent emergence of spin caloritronics has focused considerable attention on the interplay between spin, charge, and temperature gradients in magnetic materials. A reliable and energy efficient method for generating pure spin currents would signify an important step toward future spin-based nano-electronics that may offer lower power consumption and greater processing capabilities. To develop new technology using thermoelectric effects in magnetic thin films, it is essential to understand thermal and electrical transport through these films. One possible source of pure spin currents is the so-called spin Seebeck effect (SSE) in which a thermal gradient (∇T) applied to a ferromagnet is thought to produce a pure spin current detectable by measuring a transverse voltage (V_T) generated by the inverse spin Hall effect. However, recent work on spin-dependent transport in thin film nanostructures supported by bulk substrates has underscored the difficulty in understanding ∇T in these systems due to uncertainty in the direction of the applied ∇T through a substrate with a thermal conductance several orders of magnitude larger than the sample conductance. These results suggest that early SSE experiments may have been strongly affected by other effects such as the anomalous Nernst effect. They may also have been affected by thermoelectric effects generated from planar thermal gradients such as the planar Nernst effect which develops a V_T in a film with a planar ∇T and magnetization.

In this dissertation, I introduce the concepts of thermal conductivity, the Wiedemann-Franz law, and thermoelectric effects including the Seebeck effect, the Peltier ef-

fect, and the planar Nernst effect (PNE). Next, I describe our experimental method for measuring thermal and electrical transport in non magnetic and ferromagnetic metallic thin films using suspended Si-N membrane structures. Our membrane method reduces the background thermal conductance contribution by 5 orders of magnitude when compared with similar experiments conducted on thin films supported by bulk substrates. This confinement to the plane of the platform and film ensures a ∇T in the x- or y-direction only. The experiment therefore enables exploration of thermoelectric effects in a completely 2-D configuration. Next, I present results of several experiments probing thermal conductivity and the Lorenz number in thin films. Both the thermal conductivity and electrical conductivity of metallic thin films is lower that bulk values from literature. The deviation of the Lorenz number from the theoretically predicted Sommerfeld value in all films indicates imbalances between the heat and charge currents in the films from scattering or additional thermal conductivity contributions from magnons and phonons. I also present results from experiments measuring the Seebeck effect or thermopower, and anisotropic magnetoresistance in ferromagnetic thin films. In these films, the thermopower scales with resistance as predicted by the Mott equation, and the magnetic field dependence of the thermopower results from the same spin-dependent scattering responsible for the AMR. I present the first results from experiments designed to probe the PNE and related effects such as the SSE in ferromagnetic thin films. The results share features previously attributed to the SSE such as linear $\triangle$T dependence and sign reversal on hot and cold sides of the sample, however, the voltage generated transverse to the applied ∇T is always even in applied field due to spin-dependent scattering. The data display a $\sin\theta\cos\theta$ angular dependence predicted by the PNE rather than the $\cos\theta$ angular dependence expected from the SSE. In

these experiments, we observe no evidence of a thermally generated spin current, and the upper limit on the SSE coefficient in our experiment is 15-30 times smaller than previously reported by experiments conducted using bulk substrates. Finally, I present first results from experiments designed to measure the Peltier effect in thin films and test the interdependence between the Peltier and Seebeck effects predicted by Onsager reciprocal relations. These are the first measurements of the Peltier effect and Onsager reciprocity in ferromagnetic thin films near room temperature, and are an important step to confirm the validity of the theoretically predicted Onsager reciprocity in these systems.

Acknowledgements

On a journey such as this, there are many people along the way who make a difference. I'd like to first acknowledge my PhD adviser, Barry Zink. Thank you for fielding my interminable questions and for sharing your candid comments, insight and thoughtful advice. I appreciate your guidance through my graduate career from the crazy first year to the last. I would also like to thank my committee members Davor Balzar, Gareth Eaton, Matt Pufall, and Sean Shaheen for the time they took to read my dissertation, write letters of recommendation, dole out helpful advice, and for their insightful comments and questions. Thanks to all my fellow graduate students who were always a source of laughs and sanity. In particular, I'd like to thank Rubina Sultan for showing me the ropes my first year in the lab, and Luke Sawle and Dain Bassett for interesting conversations and many laughs. I appreciate all of AJ Sigdel's consistent optimism and laid back approach to physics. I owe my graduate school sanity to Jamie Lomax. Our many candid conversations, cups of tea, bacon jokes, tooth pictures, and trips to Beans kept me from losing my mind over our six years in school together. I found the support of my family, both Averys and Logans, invaluable. My mother and father, James and Angela Avery, encouraged me to strive for the best, called me a 'doctor' from the beginning, and delighted in dancing on Saturn's rings. I can never express how much your love and support has meant to me my entire life. Finally, thank you to my husband William Logan, who recognized the importance of following your dreams no matter how challenging, and stood beside me through the entire journey, late night fills and all. Your insatiable drive to learn and grow was particularly inspiring. Your unwavering support meant the world. Thank you, my sweet love.

Contents

List of Figures

Chapter 1

Introduction

Studies of thermal and electrical transport in thin films have become increasingly important as components for next generation technological devices and alternative energy solutions are miniaturized to the micro- and nanoscale. As these components are scaled down into geometries such as nanowires, nanodots, and thin films, the effect of heating and heat flow through the constituent materials has important consequences that affect the efficiency and performance of the components. The branch of physics that focuses on temperature gradients and their effect on electron flow in a material is known as thermoelectrics.

Since the discovery of the Seebeck effect in the early 1800s (1), the pairing between heat and charge in thermoelectric materials has been extensively studied. From power generation and electric refrigeration, to electricity generated by automobile waste heat and the thermocouple, thermoelectric materials have had a sizable impact on everyday technology and its applications. One of the most important applications of thermoelectric research is in the energy sector where the search continues for renewable energy alternatives with high efficiency and low

cost. The dimensionless figure of merit $ZT = \alpha^2\sigma T/k$ represents the thermoelectric efficiency of a material. ZT is a function of the Seebeck coefficient or thermopower α, the electrical conductivity σ, and the thermal conductivity k of a material. Ideal thermoelectric materials will have high value for $\alpha^2\sigma$ and a low k for the highest ZT and therefore maximum efficiency. Some of the most promising candidates for high thermopower are low dimensional systems such as thin films, nanowires, and nanotubes. In one study, a single wall carbon nanotube exhibited a thermopower coefficient of 42 μW/K, an order of magnitude higher than simple metals Au and Cu which are $\approx$ 1 μW/K (2). However, as samples are scaled to smaller and smaller sizes, measurements of thermal transport become more challenging and experiments devised to probe thermal transport require new techniques and clever design to overcome these challenges.

Spintronics is another branch of physics that has had a profound impact on technological applications such as magnetic hard drives (3). Though long neglected in the field of charge based electronics, the importance and possible applications of the electron spin was finally recognized in the 1980s with the simultaneous discovery of giant magnetoresistance by Peter Grünberg and Albert Fert (4, 5, 6). Their discovery revolutionized magnetic hard drive storage and earned them the 2007 Nobel Prize in Physics. The development of hard drive read heads based on the GMR effect represents the most significant commercial application to date for the field of spintronics. However, new advances continue in the field and there is still great potential for groundbreaking new technologies. Two such developments being explored are improved sensing heads based on magnetic tunnel junctions (7, 8) and racetrack memory (9, 10), which uses the movement of domain walls in permalloy wires over read and write devices to generate a prototype computer that is non-

volatile and independent of motors and disks (11). Future spin based applications promise faster computing times, nonvolatility, and lower power consumption in next generation technological devices.

Combining the fields of spintronics and thermoelectrics yields a recently emerging sub-field of physics called spin caloritronics. The name originates from 'calor', the Latin word for heat. Research in the field of spin caloritronics focuses on the basic fundamental physics governing the coupling between spin, charge, and thermal transport in small samples. Recent experiments in the field have explored topics such as thermally induced spin transfer torque (12) and thermally induced domain wall motion (13). However, the spin caloritronics effect most often researched is the so-called spin Seebeck effect (14, 15, 16, 17, 18, 19). Purported to be the spin analog of the Seebeck effect, the spin Seebeck effect is thought to generate a pure spin current from an applied temperature gradient in a ferromagnetic material. Even though the spin Seebeck effect has been reported in ferromagnetic metals, semiconductors, and insulators, there is still no full theoretical explanation that explains the fundamental physics governing the effect in all three types of materials (20). In addition to the need for a satisfactory theoretical explanation, the original observations of the spin Seebeck effect in metals (14) have yet to be replicated. Spin caloritronics seeks to understand the basic physics behind thermomagnetoelectric effects in small samples and like spintronics, shares the ultimate goal of faster, smaller, and more energy efficient technological devices. All three fields are ripe for further exploration and share the urgent need for careful thermal transport measurements despite their experimental difficulties.

The goal of this dissertation is to present a series of experiments designed to explore thermal and electrical transport in ferromagnetic thin films. Chapter 2 in-

troduces the concepts of thermal conductivity and several different thermoelectric effects. Chapter 3 presents our technique for making thermal transport measurements of thin films using a suspended Si-N membrane structure. The remaining chapters present results from several experiments probing the thermal conductivity, electrical resistivity, the Lorenz number, the Seebeck effect or thermopower, the planar Nernst effect, the magneto-thermopower, the anisotropic magnetoresistance, and the Peltier effect in ferromagnetic and nonmagnetic metallic thin films.

Chapter 2

Thermal Conductivity and Thermoelectric Effects

Accurate characterization of thermal and electrical properties of thin films and other micro- and nanoscale samples such as nanowires has become increasingly important both for fundamental physics as well as industrial applications in which technological components continue to be miniaturized. Though electrical measurements are relatively straightforward as long as electrical contact to the sample is possible, thermal measurements have proven to be much more challenging. In this chapter we introduce the concepts of thermal conductivity, the Wiedemann-Franz law, and several relevant thermoelectric effects including the Seebeck, the Peltier, the spin Hall, and the Nernst effects.

2.1 Thermal Conductivity

Thermal conductivity (k) is an intrinsic material property that quantifies the material's ability to conduct heat. Thermal conductivity is defined as the heat flux through a cross section of a material generated in response to an applied thermal gradient or

$$k = -\frac{\vec{Q}}{\vec{\nabla} T} \tag{2.1.1}$$

All materials conduct heat energy, though the quantity of heat and the mechanism of transfer vary depending on whether the material is a metal, superconductor, semiconductor, or an insulator. Insulators conduct heat mainly through phonon vibrations. Phonons also transfer heat in metallic samples as well, although the main heat carriers in metals are electrons. Thermal conductivity and its temperature dependence vary considerably across different materials and between different samples of the same material due to a variety of properties including crystalline structure, differing grain sizes in polycrystalline materials, the inclusion of defects, alloy concentration, and scattering of the excitations responsible for heat transfer. This variation along with the importance of understanding k in thin films for technological applications such as thermoelectric devices, make k an important topic of research. In contrast with the straightforward methods for determining the electrical conductivity of a material, thermal conductivity in thin films is a difficult quantity to measure. Rather than making a direct measurement, one method used to gain insight into thermal transport is to estimate k using the Wiedemann-Franz law.

2.2 The Wiedemann-Franz Law

In the mid 1800s, Wiedemann and Franz demonstrated experimentally that k was proportional to σ in several metals including Ag, Cu, and Au. In equation form, they determined

$$\frac{k}{\sigma} = LT \tag{2.2.1}$$

where T was temperature and L was a constant called the Lorenz number. Originally thought to be a constant applicable to all metals, Lorenz noted in 1881 that L was specific to the metal being measured (21).

To derive the Wiedemann-Franz law mathematically, we begin by defining thermal conductivity and electrical conductivity while treating the electrons as a free electron Fermi gas. Using the kinetic theory of thermal conduction in gases, thermal conductivity can be expressed as a function of heat capacity,

$$k = \frac{1}{3} C \bar{v} \lambda \tag{2.2.2}$$

where C is the heat capacity per unit volume, $\bar{v}$ is the average velocity of a particle, and λ is the particle mean free path. The mean free path is the average distance traveled by an electron with velocity v given time between collisions τ ($\lambda = \bar{v}\tau$). When the electrons are treated as a Fermi gas, the heat capacity of an electron is dependent on the density of states, $D(\epsilon_F)$,

$$C = \frac{1}{3} \pi^2 D(\epsilon_F) k_B^2 T \tag{2.2.3}$$

Substituting in $D(\epsilon_F) = 3N/(2k_BT_F)$ for the density of states gives

$$C = \frac{1}{2}\pi^2 n k_B \frac{T}{T_F}. \tag{2.2.4}$$

In a free electron gas, an electron moving at the Fermi velocity, v_F, has a Fermi energy $k_BT_F = \frac{1}{2}mv_F^2$. Solving for $(1/2T_F)$ and substituting into equation 2.2.4, gives the following expression for thermal conductivity

$$k = \frac{1}{3}\frac{\pi^2 n k_B^2 T}{m}\tau. \tag{2.2.5}$$

Next, we develop an expression for electrical conductivity using the Drude model. After defining the electric current density, $J = -ne\bar{v}$ where n represents the number of electrons and e the electron charge, applying Ohm's law $\vec{J} = \sigma\vec{E}$, and solving for σ gives the well-known expression

$$\sigma = \frac{ne^2\tau}{m} \tag{2.2.6}$$

where m represents the electron mass and τ the time between collisions. Using Eqn. 2.2.5 and Eqn. 2.2.6, the ratio of thermal to electrical conductivity then becomes

$$\frac{k}{\sigma} = \left[\frac{\pi^2}{3}\left(\frac{k_B}{e}\right)^2\right]T. \tag{2.2.7}$$

The quantity in brackets in Eqn. 2.2.7 is a constant known as the Sommerfeld value ($L_o = 2.44x10^{-8}V^2K^{-2}$). L is equal to L_o when scattering events have the same effect on both the thermal and electrical currents.

2.2.1 Lorenz number and Scattering

If the heat carrier and charge carrier populations are not equal, the value of L will deviate from the expected L_o. For example, this occurs when phonons make a significant contribution to thermal conductivity of a material without contributing to electrical conductivity. It also occurs when electrons are removed from the thermal current but not the electrical current in a metal. Fig. 2.1 shows the density of states

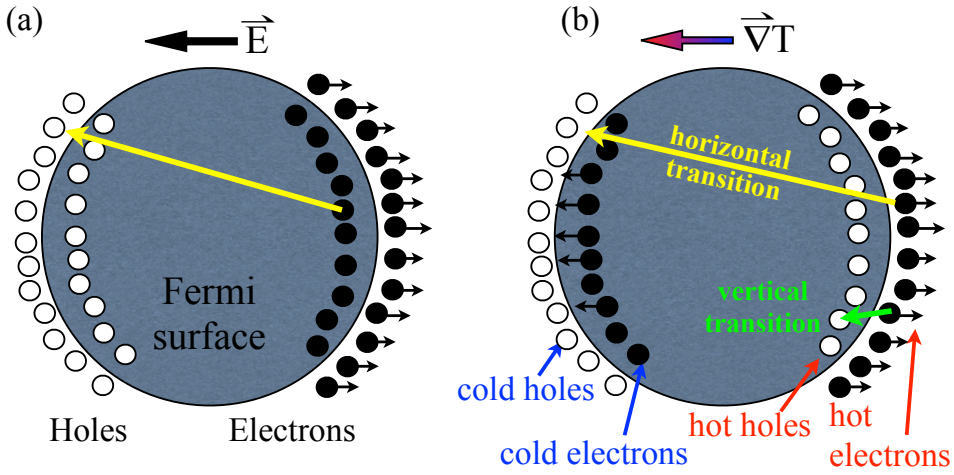

Figure 2.1: Illustration of horizontal and vertical transitions. (a) shows the distribution of electrons and holes in response to an applied electric field. (b) shows the Fermi surface and distribution of electrons and holes in response to a thermal gradient. During vertical transitions, electrons scattered just inside the Fermi surface are removed from the thermal current but not the electrical current. Horizontal transitions, in which the scattering occurs across the Fermi surface, remove the electrons from both currents.

and Fermi surface for the (a) electrical conduction and (b) thermal conduction in a typical metal. An applied electric field shifts the Fermi surface equally, causing more electrons to move to one side of the Fermi surface and leaving holes on the opposite side. However, the electron distribution for thermal conduction shown in Fig. 2.1 (b) is quite different. "Hot" electrons gain additional energy and travel down

the thermal gradient causing more electrons outside the Fermi surface away from the heat source. "Cold" electrons travel in the opposite direction and are distributed inside the Fermi surface near the heat source. This distribution places "hot" holes just inside the Fermi surface on the cold side and "cold" holes outside the Fermi surface on the hot side. Scattering through small angles, known as vertical processes or transitions, removes electrons from the thermal current without affecting the electric current. Thus vertical processes are responsible for observed deviations from L_o. Scattering through large angles, or horizontal processes, removes electrons from both currents equally causing no change to the ratio of thermal to electrical conductivities (22).

At very low temperatures, where the lattice phonons no longer contribute to resistivity, scattering events are dominated by elastic impurity scattering. The elastic impurity scattering generates horizontal transitions in this regime, and $L \approx L_o$ (21). At high temperatures, where the temperature of the material is much higher than the Debye temperature ($T >> \Theta_D$), the amount of heat carried by electrons increases as the phonon density increases. The energy exchanged by phonon-electron scattering is greater than $k_B\Theta_D$, therefore elastic scattering causes $L \approx L_o$ as well (22). In the intermediate temperature regime, electron-phonon and electron-electron interactions generate vertical transitions that scatter electrons from the thermal current but not the electric current. Due to its sensitivity to scattering events, direct measurements of the Lorenz number are useful for determining if inelastic scattering processes are present or if k has an additional contribution from other excitations such as phonons or magnons.

2.3 The Seebeck Effect

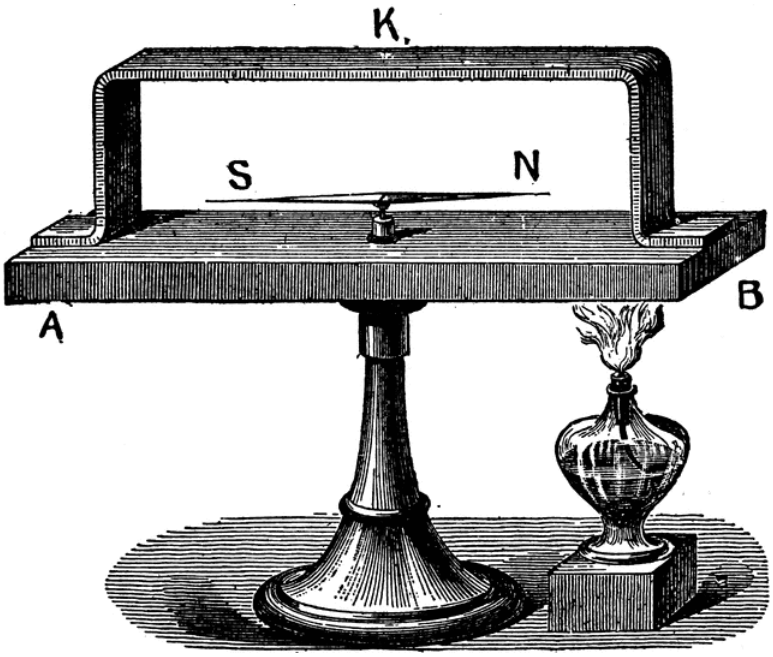

Figure 2.2: An illustration of the original apparatus used by Thomas Seebeck to discover the thermoelectric effect. A and B represent the two junctions formed by a block of bismuth and a u-shaped strip of copper (K). The compass needle moved in response to heating or cooling junctions A or B.

In the mid-1800s Thomas Seebeck discovered the thermoelectric effect, or thermopower, using an apparatus similar to the one shown in Fig. 2.2. The original experiment was composed of a circuit of copper and bismuth with a compass needle in the loop formed by the Bi and Cu circuit. Heating one of the junctions between the two metals deflected the compass needle in one direction and cooling deflected it in the opposite direction (23). Seebeck originally attributed this deflection to a magnetic response to the applied temperature difference. However, it is now known that the deflection of the compass needle is due instead to the generation of a steady state current by a temperature gradient.

A thermoelectric material is one that generates a voltage in response to a temperature difference across the material. There is a wide range of applications for thermoelectric materials from metals used in thermocouples for temperature detection to radioisotope power systems that convert the heat released from nuclear decay into electricity for space exploration (24). One of the most commonly explored research directions is the application of thermoelectric materials to renewable energy processes such as converting waste heat into electricity and generating additional electricity from the heat generated from photovoltaics.

Thermopower is an intrinsic material property, therefore the thermopower coefficient must describe the electric response of a material to an applied temperature gradient. To define the thermopower coefficient, we start with the coupling between the electric field and a thermal gradient in a metal. This can be expressed as a matrix

$$\begin{pmatrix} \vec{J} \\ \dot{\vec{Q}} \end{pmatrix} = \sigma \begin{pmatrix} 1 & \alpha \\ \Pi & k/\sigma \end{pmatrix} \begin{pmatrix} \nabla V \\ -\nabla T \end{pmatrix} \tag{2.3.1}$$

where $\dot{\vec{Q}}$ is the heat current density, $\vec{J}$ is the electrical current density, σ is the electrical conductivity, and k is the thermal conductivity (25, 22). By applying different initial conditions such as $\nabla T = 0$, we can define the remaining coefficients, α and Π.

When the sample is in an open circuit, no current flows and $\vec{J} = 0$. Therefore $\sigma \nabla V - \sigma \alpha \nabla T = 0$. Solving for α gives $\alpha = \nabla V / \nabla T$. This coefficient, which quantifies the voltage developed per change in temperature, is known as the Seebeck coefficient or thermopower.

For a deeper understanding of the fundamental physics governing thermopower,

we must take into account the chemical potential (ς) of the electron system. ς is a function of temperature and therefore will vary throughout the metal. This can result in the diffusion of charge without an electric field and the flow of heat which may not be equal to the energy flux. After accounting for these variations, and noting that $\varsigma \approx E_F$ for metals, rewriting the equations for heat and current flow gives an equation for the thermopower

$$\alpha(E) = \frac{\pi^2 k_B^2 T}{3e}\left[\frac{1}{\sigma(E)}\frac{\partial\sigma(E)}{\partial E}\right]_{E=E_F} \tag{2.3.2}$$

where σ is the electrical conductivity, E_F is the Fermi energy, and e the electron charge (22). Using the rules for natural log, this Eqn. 2.3.2 can be simplified to

$$\alpha(E) = \frac{\pi^2 k_B^2 T}{3e}\left[\frac{\partial ln\sigma(E)}{\partial E}\right]_{E=E_F}. \tag{2.3.3}$$

The expression for σ from kinetic theory applicable for Fermi surfaces that are not necessarily spherical is

$$\sigma = \frac{e^2 \lambda A}{12\pi^3 \hbar} \tag{2.3.4}$$

where A is the area of the Fermi surface and λ is the mean free path of a charge carrier, whether electron or hole. Substituting σ into the bracketed expression in Eqn. 2.3.3, using the product rule for the partial derivatives, and rewriting using the natural log gives

$$\left[\frac{\partial ln\sigma(E)}{\partial E}\right]_{E=E_F} = \left[\frac{lnA}{\partial E} + \frac{ln\lambda}{\partial E}\right]_{E=E_F}. \tag{2.3.5}$$

This equation offers insight into the dependence of the thermopower coefficient on

energy E. The sign and the magnitude of α are dependent on electron scattering and how the Fermi surface interacts with the first Brillouin zone (FBZ) boundary. In a metal, the energetic electrons are difficult to scatter due to their high energy value. This results in a long average mean free path. Therefore the second term in Eqn. 2.3.5 is typically positive. The first term is dependent on how the interaction between the Fermi surface and the FBZ changes with respect to energy. For example, if the surface is expanding to the FBZ, the area is increasing and this term is positive. When the surface reaches the FBZ and beyond, the area inside the Fermi surface begins to decrease and this term is negative. The balance of the first and second terms of Eqn. 2.3.5 determines whether α is positive or negative.

2.4 The Peltier Effect

Another effect related to the thermal and electrical transport properties of a material is known as the Peltier effect. The Peltier effect was discovered by Jean-Charles Peltier shortly after the discovery of the Seebeck effect and is essentially the conjugate of the Seebeck effect. In the Peltier effect, a current flowing through a material will absorb heat at one end and generate heat at the opposite end. The direction of current flow dictates whether heat is absorbed or generated.

We can define the Peltier coefficient (Π) using Eqn. 2.3.1 by setting $\nabla T = 0$. Dividing the heat current density by the charge current density gives

$$\frac{\dot{\vec{Q}}}{\vec{J}} = \frac{\Pi\sigma\nabla V}{\sigma\nabla V} = \Pi \tag{2.4.1}$$

Therefore, Π represents the heat evolved per unit area per unit current or the magni-

tude of heating (or cooling) generated from a current. Though it is a direct result of the applied current, when compared with Joule heating the Peltier heating exhibits striking differences. The Joule effect always results in sample heating where the Peltier absorbs or liberates heat depending on the current direction. The heat absorbed or generated is proportional to the applied current in the Peltier effect, where the heat generated from the Joule effect depends on the current squared. Reversing the current reverses the Peltier effect from heating(cooling) to cooling(heating) but has no effect on the heat generated through the Joule effect. Experiments probing the Seebeck and Peltier effects can directly test the relationship between α and Π ($\Pi = \alpha T$) predicted by the Onsager symmetry theorem for which Lars Onsager won the 1968 Nobel prize in chemistry.

2.5 The 'Spin' Seebeck Effect

Just as the Seebeck effect, or thermopower, can be employed to generate charge imbalance from a temperature gradient, spin caloritronics seeks to generate a spin imbalance from a temperature gradient through the so-called 'spin' Seebeck effect. The spin Seebeck effect (SSE) was first reportedly observed in permalloy in 2008 and since then there have been several reports of the SSE in a variety of materials using a variety of experimental geometries (14, 15, 16, 17, 18, 19). Though there is not a comprehensive theoretical explanation for the SSE in metaIs, semiconductors, and insulators, if a spin analog of the thermopower exists, one mechanism for spin separation could be through the Seebeck coefficients for the different spin populations. In a material with two spin populations, "spin-up" and "spin-down", spin imbalance would occur if the up spins had a thermopower coefficient of oppo-

site sign when compared with the down spin's Seebeck coefficient. A temperature gradient along the material would then result in the up and down spins moving in opposite directions and generating spin imbalance across the material. Fig. 2.3 is a

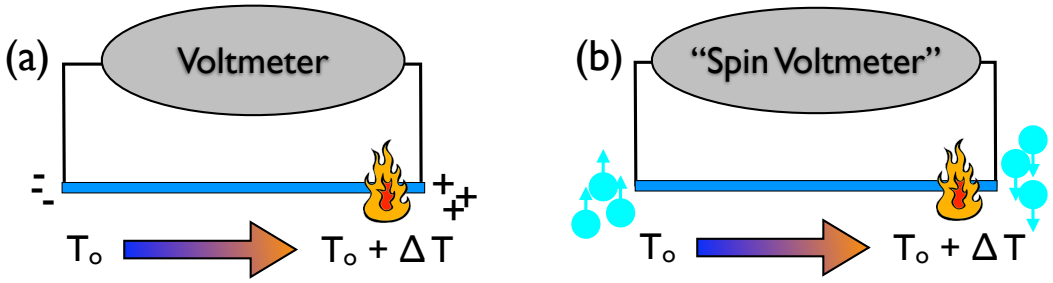

Figure 2.3: An illustration comparing the Seebeck effect (a) and the supposed spin Seebeck effect (b).

schematic comparing the charge and spin separation predicted by the Seebeck effect and SSE.

One challenge presented by SSE experiments is the need to detect a spin current or spin imbalance once generated in a material. In an open circuit, the potential drop generated by a material's thermopower is measurable using a conventional voltmeter. An ammeter is all that is necessary to measure a charge current generated through the Seebeck effect in a closed circuit. To infer the presence of a spin current, previous SSE experiments borrowed a technique from spin pumping experiments. In experiments where spin currents are generated through microwave excitation, for example, the inverse spin Hall effect converts the spin current into a measurable voltage through the mechanism of spin-orbit scattering.

2.5.1 The Inverse Spin Hall Effect

To understand the inverse spin Hall effect, we begin by explaining the spin Hall effect. Like the Hall effect where electrons are preferentially deflected to one side of a material through the Lorentz force on the moving charges, in the spin Hall effect the charges are preferentially deflected by spin-orbit scattering events such as skew scattering by phonons and impurities. The up spins and down spins are scattered in opposite directions giving rise to a spin imbalance or current. Fig. 2.4 compares the

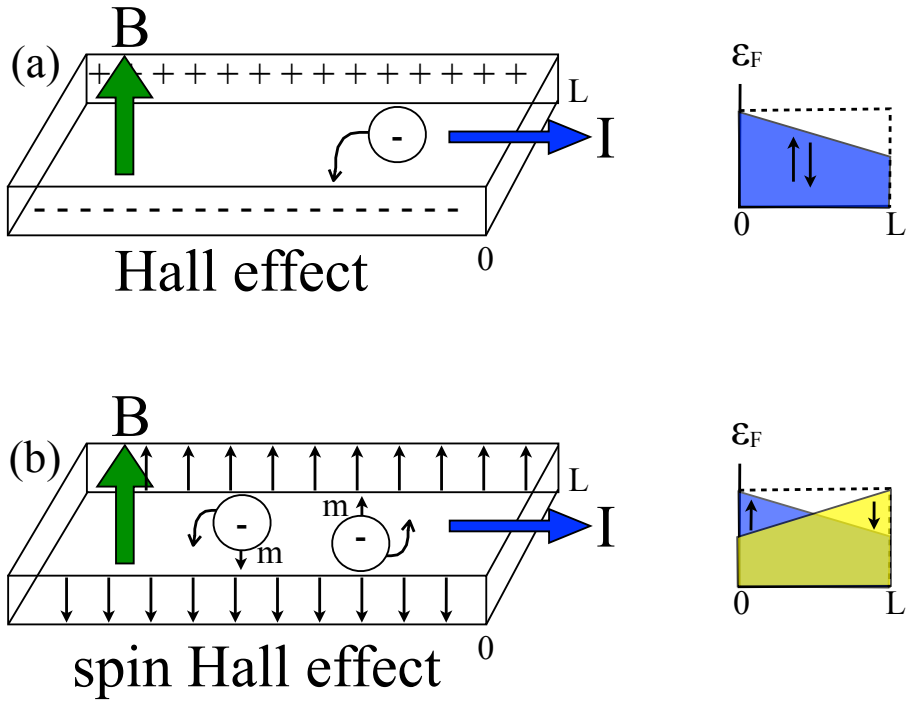

Figure 2.4: An illustration comparing the Hall effect and the spin Hall effect. Top: the Hall effect and resulting Fermi levels representing a potential difference created by electrons and holes. Bottom: the spin Hall effect and resulting Fermi levels representing a spin potential difference created by separation of the up and down spins in a material.

Hall effect with the spin Hall effect. Thus, in the spin Hall effect a charge current

moving in the x-direction generates a spin voltage or current in the y-direction (26). The inverse of this process generates a charge current or potential drop from an existing spin current and is known as the inverse spin Hall effect (ISHE).

2.6 The Nernst Effect

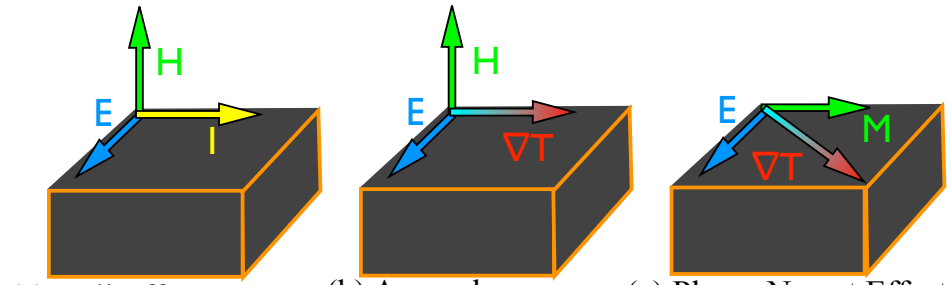

Figure 2.5: A diagram comparing (a) the Hall effect with (b) the anomalous Nernst effect and (c) the planar Nernst effect.

Along with the thermoelectric effects discussed in previous sections, there are additional effects that arise from the additional spin degree of freedom found in magnetic materials. One of the most pertinent effects for the group of experiments presented in this dissertation is the Nernst effect. The Nernst effect is the thermal analog of the Hall effect. In the Nernst effect, rather than a current in the x-direction, a temperature gradient in the x-direction coupled with an external magnetic field in the z-direction gives rise to an electric field in the y-direction. Like the Hall effect, the Lorentz force is responsible for deflecting the electrons to one side of the material/sample. In ferromagnetic materials, there is an additional term in the Nernst effect equation arising from the magnetization of the material. This is the anomalous Nernst effect, ANE. Fig. 2.5 shows a comparison of the Hall effect

and the ANE. When a magnetic field is present, the Lorentz force also results in the deflection of electrons from the original current direction. The electrons begin to orbit around the applied field and will no longer contribute to the current flow. This change in resistance with applied magnetic field is known as "ordinary" magnetoresistance.

In magnetic materials, the spin-orbit interaction is responsible for several effects that are often larger in magnitude than their counterparts generated through the Lorentz force. One example of an effect generated through the spin-orbit interaction is the anisotropic magnetoresistance (AMR). In a magnetic material, spin dependent scattering is responsible for resistance changes resulting from changes in the magnetization of the material. When the electrons move parallel to the direction of magnetization in a sample, the scattering rates are higher than they are if the electrons move perpendicular to the magnetization. This results in higher resistance for parallel magnetization and lower resistance for perpendicular magnetization. Another effect generated through the spin-orbit interaction is the planar Nernst effect (PNE). The PNE is present in samples where the temperature gradient and the magnetization are in the plane of the sample. The PNE is the thermoelectric equivalent to the AMR in ferromagnetic materials. Like AMR, the PNE is generated through spin-dependent scattering, rather than the Lorentz force that is responsible for the Nernst effect.

2.7 Summary

In this chapter, we have introduced the concepts of thermal conductivity, the Wiedemann-Franz law, the Lorenz number and how it is affected by various scatter-

ing events, and several thermoelectric effects including the Seebeck effect. A thorough comprehension of the basic physics governing these effects in low-dimensional geometries such as thin films is imperative for basic research and future applications to thin film technology where heat flow is important. In the next chapter we discuss the difficulties associated with measuring heat flow in these geometries and present our technique for measuring thermal transport in these challenging systems.

Chapter 3

Thermal Conductivity and Thermopower Measurement Technique

This chapter focuses on experimental techniques for measuring thermal conductivity and Lorenz number in thin films. We discuss a few of the challenges associated with measuring thin film thermal conductivity and outline our method for measuring thermal properties of thin films.

3.1 Introduction

Although the Wiedemann-Franz law is useful for estimating the k of bulk metals, it is not valid for samples such as bulk insulators and semiconductors or reduced dimension samples such as thin films. The next few paragraphs will address exist-

ing methods for measuring k in thin films and the challenges associated with these measurement techniques.

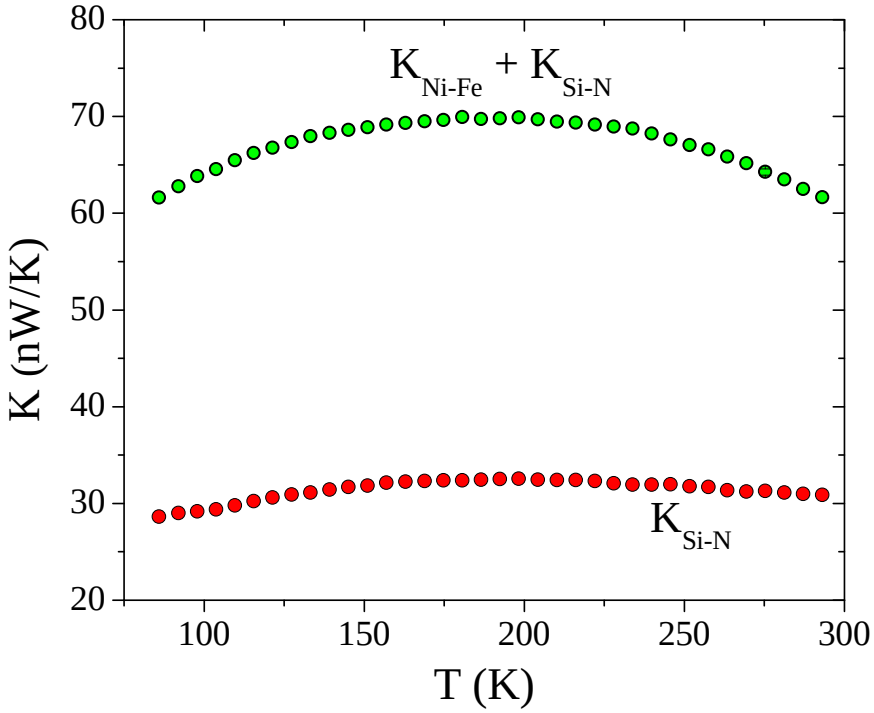

Figure 3.1: Thermal conductance as a function of temperature for our Si-N supporting membrane (K_{Si-N}) and the total conductance of a thin permalloy film supported by the membrane.

In materials where there are contributions to k in addition to the electronic contribution, and in non-bulk samples such as thin films and nanowires where k is dramatically different than the bulk value of the same material, it is necessary to measure k directly. It is not accurate to assume $k_{bulk} = k_{film}$ because thin films are often morphologically very different from their bulk crystalline and polycrystalline counterparts. For example, a thin film may exhibit disruption in phonon propagation due to polycrystalline grain boundaries formed during film growth. Sample defects

and impurities can scatter electrons, and in very thin films where the thickness is on the order of the mean free path of the heat carriers, surface effects can scatter the heat carriers. Though necessary to measure directly, there are challenges associated with these measurements. Thin films are often deposited on a bulk substrate for support, but bulk substrates typically have a large background thermal conductance that can overwhelm the thermal conductance of the film of interest.

Fig. 3.1 shows the background thermal conductance of a 500 nm thick supporting Si-N membrane (K_{Si-N}) and the total thermal conductanceof a 20 nm Ni thin film (K_{Total}) deposited on a similar membrane. [1] At 300 K, $K_{Si-N} \approx 30$ nW/K. The addition of a thin film adds another 30 nW/K. In comparison, the thermal conductance of a typical bulk substrate is 5 orders of magnitude higher. Even if a technique is sensitive enough to measure the additional contribution of a small film deposited on the substrate, subtracting off a K_{bulk} this large to determine the thin film contribution to K_{Total} introduces enormous error. The substrate can also draw heat away from the film, making it difficult to determine the thermal gradient in the plane of the film correctly. Additionally, thin film k is typically anisotropic so the in-plane thermal conductivity ($k_{\parallel}$) is not equal to the cross-plane thermal conductivity ($k_{\perp}$). Finally, radiation effects are problematic at base temperatures over 100 K where the heat intended to flow through the material will radiate instead. Over the last 30 years there have been several well-established techniques to developed to overcome some of these thermal measurement challenges. Two of the most commonly applied techniques are the 3-ω method and the membrane technique.

The 3-ω method is predominately used to measure $k_{\perp}$ in thin films down to 20

[1] Data shown in figure 3.1 are for the 20 nm thick SSEflavors E3LL Ni-Fe sample and the 500 nm thick Si-N platform B1LL from the low temperature wafer.

nm thick (27). One of the most widely applied techniques for measuring thin film k, the 3-ω technique is an ac technique developed to reduce radiation effects. In the 3-ω method, a single metallic wire deposited on the sample acts as both heater and thermometer. An ac current with frequency ω passed through the wire generates the power necessary to establish a thermal gradient. The increase in sample temperature has both dc and ac components, where the ac component has a frequency of 2ω. The voltage drop across the heater can be solved for the 3ω component which is proportional to the temperature of the heater and detectable using a lock-in amplifier (27, 28). Although the 3-ω technique is useful for measuring film $k_{\perp}$ without a radiation contribution, it is not as easy to measure $k_{\parallel}$. There is also uncertainty associated with determining the background thermal conductance contribution from the supporting substrate. In order to determine the value for a thin film only, a reference background can be used that may introduce error from using two different background samples. The background can also be calculated, however, the equations used for this method are approximations only and can also introduce error into the measurement (27).

Time-domain thermoreflectance is a technique for measuring thermal conductivity in nanoscale samples such as nanowires. Also known as picosecond thermoreflectance, this technique involves splitting a laser into a beam that pumps heat in to the system and a beam that probes the effect of the laser heating. Changes in the reflected energy at the surface of the sample during a series of pulses indicates the changing temperature of the sample. Thermal conductivity is determined by comparing the measured cooling curve with a theoretical heat flow model. The picosecond timescale offers nanometer length resolution. Unlike the 3-ω method, time-domain thermoreflectance offers a method for separating interface thermal

conductance from the thermal conductance through a small sample such as a thin film. Some limitations of thermoreflectance include the difficulty interpreting thermal decay for times less than 50 ps and the diffusion equation breaks down at length scales on the order of charge carrier mean free paths (29).

Fabrication techniques such as deep-trench etching of Si, anisotropic Si etching, and electron beam lithography have enabled the development and application of the membrane technique for measuring $k_{\|}$. In the membrane technique, a low K membrane supports a thin film rather than a thick substrate. Each membrane has separate heaters and thermometers, compared to the one strip used in the 3-ω method. A surrounding bulk substrate supports the membrane and film and acts as a heat sink. Although the membrane method eliminates the large substrate thermal conductance to thin film k measurements, radiation in these membrane structures can still be problematic (27).

Our technique for measuring $k_{\|}$ is an adaptation of the membrane technique. We use a micromachined suspended silicon nitride (Si-N) membrane structure to measure $k_{\|}$ of thin films. The Si-N is a strong, low stress, insulating material that contributes a low background thermal conductance to thin film $k_{\|}$ measurements. Therefore, the additional thermal conductance contributed by a thin film is on the order of the background contribution or higher, making it possible to subtract out the background Si-N K contribution to a film measurement with minimal error. The area of the thermal isolation platform containing the heaters and thermometers is small and therefore radiation contributions over 100 K are eliminated in this technique. Our technique for measuring $k_{\|}$ is a robust technique with several advantages over other methods including the ability to measure thermal and electrical transport of the same sample, small background K contribution for subtraction, no radiation

contribution, and the ability to measure a wide variety of films from thick insulating films to thin ferromagnetic films.

3.2 Thermal Isolation Platform Technique

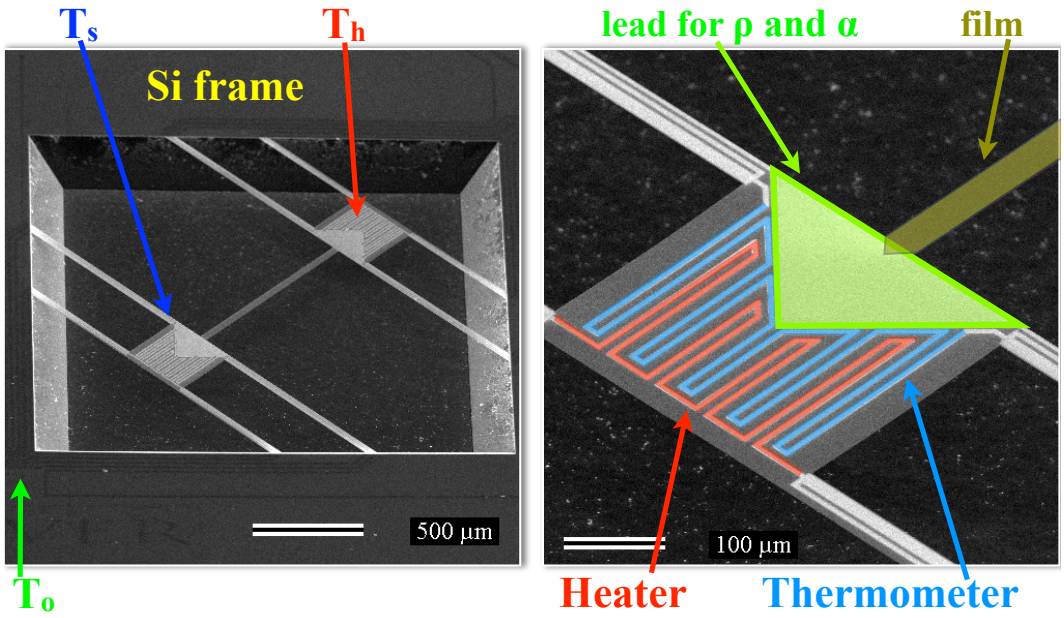

Figure 3.2: Left: SEM micrograph of a thermal isolation platform. The micrograph shows the two islands, bridge, and 8 legs that make up the platform. The platform is suspended from a Si frame. T_h, T_s, and T_o represent the hot island temperature, the cold island temperature, and the frame reference temperature respectively. Right: SEM micrograph zoom of one island showing the heater, thermometer, and triangle shaped lead for making electrical measurements in false color. The film, also highlighted in false color, is deposited on the bridge.

For thermal measurements, we use a suspended Si-N membrane structure or thermal isolation platform. Fig. 3.2 shows an example thermal isolation platform. Each platform has 2 islands that are mirror images of each other. We pattern both islands with heater and thermometer wires. A 35 μm x 806 μm Si-N bridge con-

nects the islands to each other. Four Si-N legs connect each island to the Si frame which serves as a heat sink. The eight total legs provide a link to the thermal bath. The only thermal link between the two islands is the Si-N bridge. We can generate a thermal gradient along the bridge by heating one island, reverse the thermal gradient by heating the opposite island, or heat both islands simultaneously to remove the bridge thermal gradient. This also creates thermal gradients along the legs that connect the islands to the frame whenever one or both islands are heated.

3.2.1 Platform Fabrication

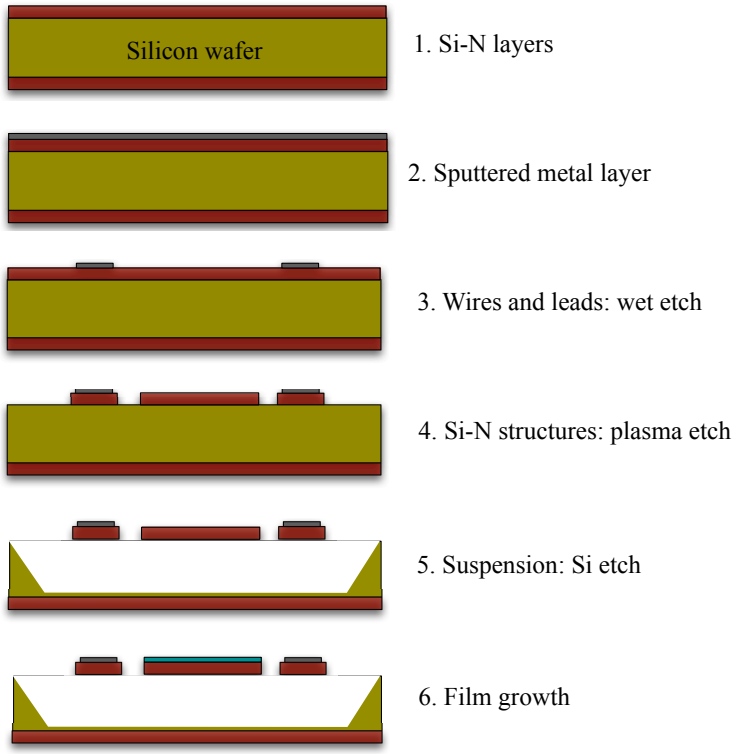

Figure 3.3: Steps in the fabrication process for the thermal isolation platform membrane structures.

Fig. 3.3 steps through the sequence for fabricating the thermal isolation plat-

forms. Fabrication begins with a 3" <100> silicon wafer. We coat the top and bottom of the layer with a layer of 500 nm thick low-stress amorphous silicon nitride, Si_3N_4, using low pressure chemical vapor deposition (LPCVD) at 835^o C at a pressure of 25 mTorr. Next we RF sputter a metal layer onto the front of the wafer. For the platforms used in the current experiments, we deposited a 200 nm Mo layer. We pattern the metal layer into heaters, thermometers, and leads using optical lithography. Next, we remove the unwanted Si-N using a plasma etch. We leave the Si-N that will become the islands, bridge, and legs and expose the Si to be removed around and underneath the remaining Si-N structure. Finally, we immerse the entire wafer in a potassium hydroxide solution (KOH) at 70^o C for 5 hours. We protect all Si-N platform structures and metal wiring with a layer of photoresist.

The KOH etch is an anisotropic Si etch that etches to the <111> plane. The entire patterned structure is oriented at a 45 degree angle so that the KOH etches the exposed Si. This removes the Si underneath the Si-N pattern and releases the island, bridge, and legs of the suspended membrane structure. Fig. 3.4 shows an early version of the platform without a bridge. The platform was not exposed to KOH for long enough. This resulted in an under-etched platform that still had small pillars of Si beneath each island.

3.2.2 Thermal Model

Heat flow through the thermal isolation platform is confined to conduction only. The small area of emissivity of the islands where the heating power is dissipated eliminates the radiation contribution typically problematic over 100 K in DC thermal measurements and all measurements are conducted at or below 1 x 10^{-5} mbar to eliminate convection. The thermal conductance through the platform is expressed

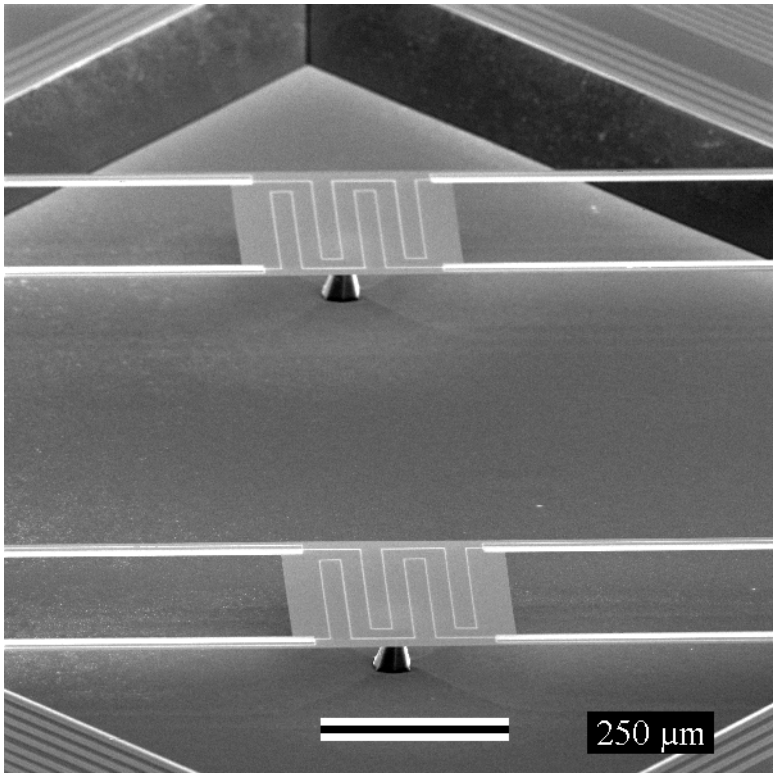

Figure 3.4: Si pillars underneath a first generation platform without a bridge that did not etch completely. Given sufficient time, these pillars are eventually removed through the KOH etch process leaving a smooth surface below the structure, and the islands and bridge freely suspended

mathematically using the steady-state heat flow equations

$$C_h \frac{\partial T_h}{\partial t} = -K_L(T_h - T_o) - K_B(T_h - T_s) + P_h, \tag{3.2.1}$$

$$C_s \frac{\partial T_s}{\partial t} = -K_L(T_s - T_o) - K_B(T_s - T_h) + P_s. \tag{3.2.2}$$

In these equations, C is the specific heat, T the temperature, K the thermal conductance, and P the applied power. The h, s, and o subscripts represent the hot island, the cold island, and the frame while the B and L subscripts represent the bridge and legs respectively. The time dependence vanishes in a steady state measurement, so

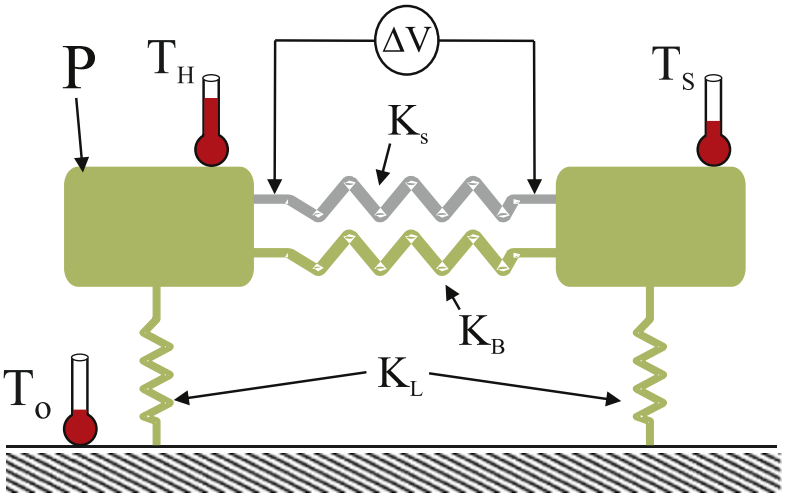

Figure 3.5: A schematic showing the simple thermal model used to describe the micromachined thermal platforms. Before deposition of a sample, the only connection between the two islands is the background thermal conductance of the Si-N bridge, K_B. Adding a sample adds the thermal link K_S, modifying the thermal model.

the left hand sides of Eqn. 3.2.1 and Eqn. 3.2.2 are equal to zero. In our thermal conductivity experiments, only one island is heated at a time, so only one power term remains, $P_h = P$ and these two equations can be simplified to identify K_L and K_B

$$K_L = \frac{P}{T_h - T_s + 2T_o}, \tag{3.2.3}$$

$$K_B = \frac{1}{2}\left[\frac{P}{T_h - T_s} - K_L\right]. \tag{3.2.4}$$

Fig. 3.5 is a schematic showing the simple thermal circuit for the thermal isolation platforms. To measure the background conductance of the bridge, we regulate the temperature of the bath. We clamp the Si frame of the platform to the Cu cold finger of a Janis sample-in-vacuum cryostat. Once regulated, we use resistance thermometry to determine the temperature of either side of the bridge (and film if

present) and the temperature on the frame. To determine the temperatures on the platform, we make a 4-wire resistance measurement of each metal thermistor, one on the frame and one on each island. Next we repeat the resistance measurements for a range of increasing heating powers for the heated island and the cold island while monitoring the frame thermistor.

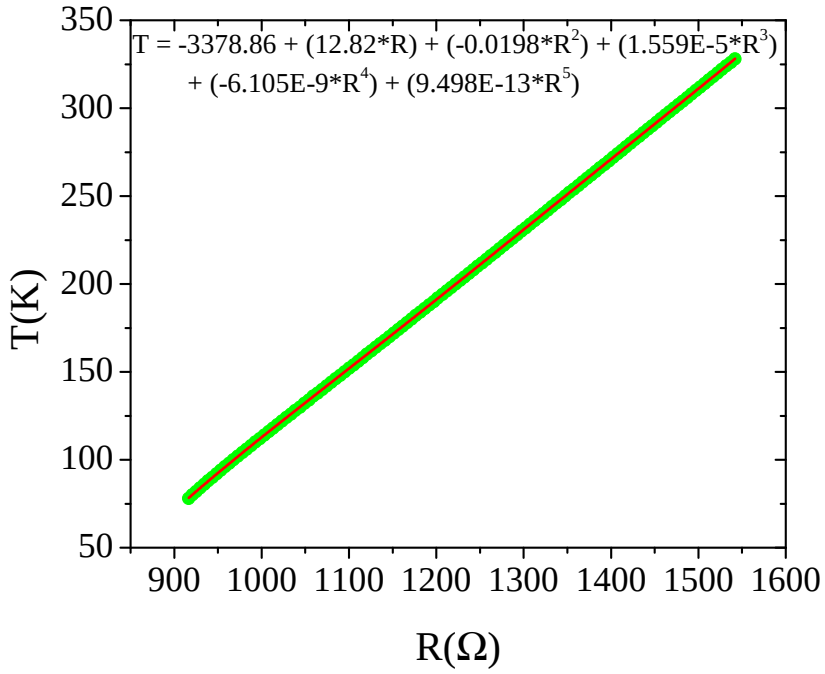

Figure 3.6: Temperature versus resistance data and the calibration fit (solid line) for an example resistor. The polynomial fit for $T(R)$ is displayed at the top of the plot.

To determine the $T(R)$ relationship we plot a T as a function of the measured resistances and fit a polynomial to generate a calibration curve for each experiment for all three thermistors. An example calibration curve is shown in Fig. 3.6. Once we have generated the calibration curves, we determine the temperature difference $(T_h - T_s)$ generated across the bridge as a result of the heating power. We also convert the frame resistance values to temperatures T_o. After converting all

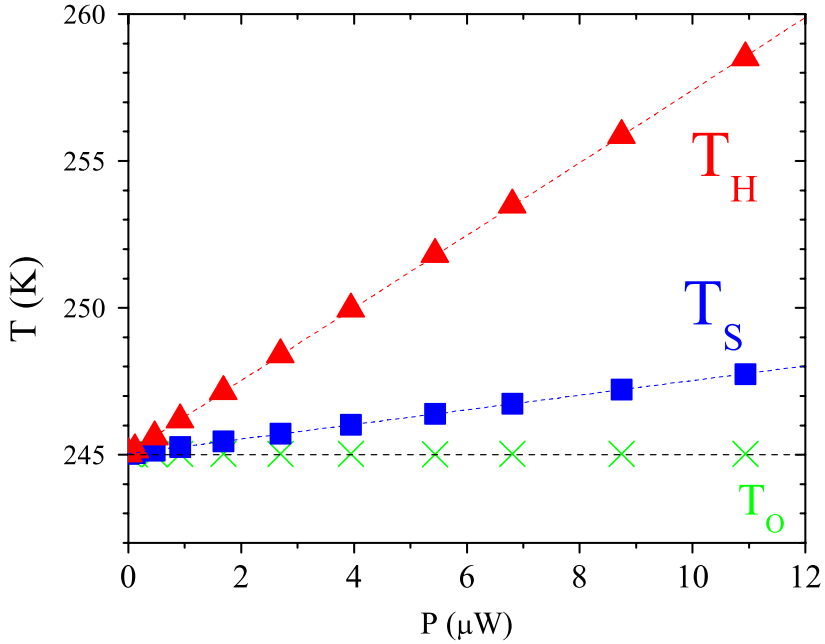

Figure 3.7: Temperature versus measured power for the Si frame, T_o, the heated island, T_h, and the island heated by the thermal conductance through the Si-N bridge, T_s at a thermal bath temperature of 245 K.

the resistances to T_h, T_s, and T_o values, plotting them with respect to measured P generates a linear plot as shown in Fig. 3.7. Eqn. 3.2.3 and 3.2.4 can be rearranged

$$T_h = \frac{(K_L + K_B)}{(2K_B + K_L)K_L} P + T_o, \tag{3.2.5}$$

$$T_s = \frac{(K_B)}{(2K_B + K_L)K_L} P + T_o, \tag{3.2.6}$$

and linear fits to these equations yield K_B and K_L.

Using the T_o values, we can also monitor the thermal stability of the frame. Fig. 3.8 shows an example of the thermal drift typical in a thermal conductance experiment exhibited by the frame thermometer T_o at 77 K. The thermal drift indicated through the base temperature in our thermal conductance experiments is minimal

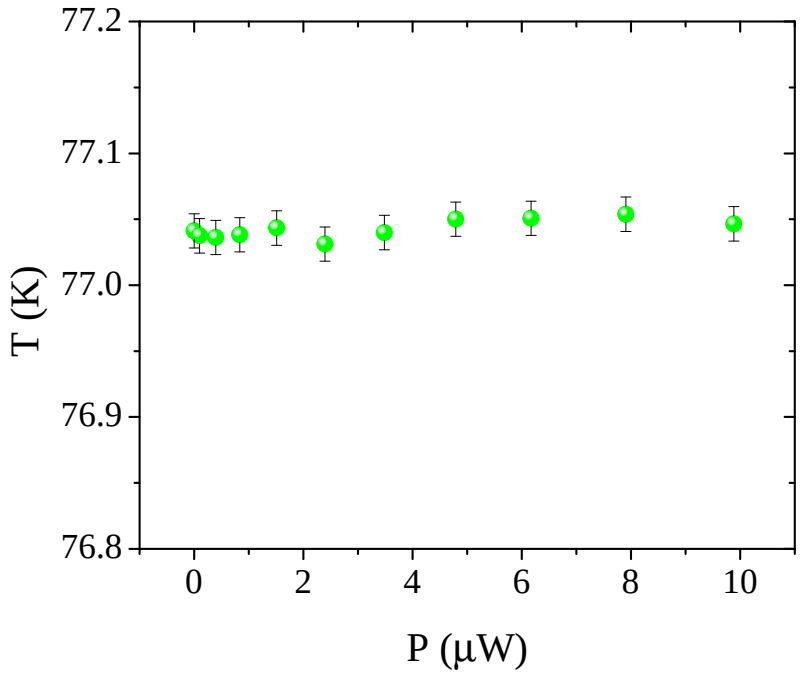

Figure 3.8: Temperature as a function of measured power for the Si frame, T_o, at a thermal bath temperature of 77 K. The frame temperature is stabilized to within 30 mK.

and the frame temperature is stabilized to within 30 mK.

3.2.3 Heat Flow Modeling with MatLab

The next important steps in our methodology were to confirm our thermal model and to understand the heat flow through our thermal isolation structure. We generated a model of the heat flow through the Si-N membranes using the Partial Differential Equation (PDE) toolbox from MATLAB. The PDE toolbox uses a finite element method which approximates a PDE solution using a piecewise linear function. To generate a model, the first step is to draw the geometry of the system. The

next step is to define a solution mesh. The complicated mesh and membrane geometry we used is shown in Fig. 3.9. For this model, we used a mesh growth rate of

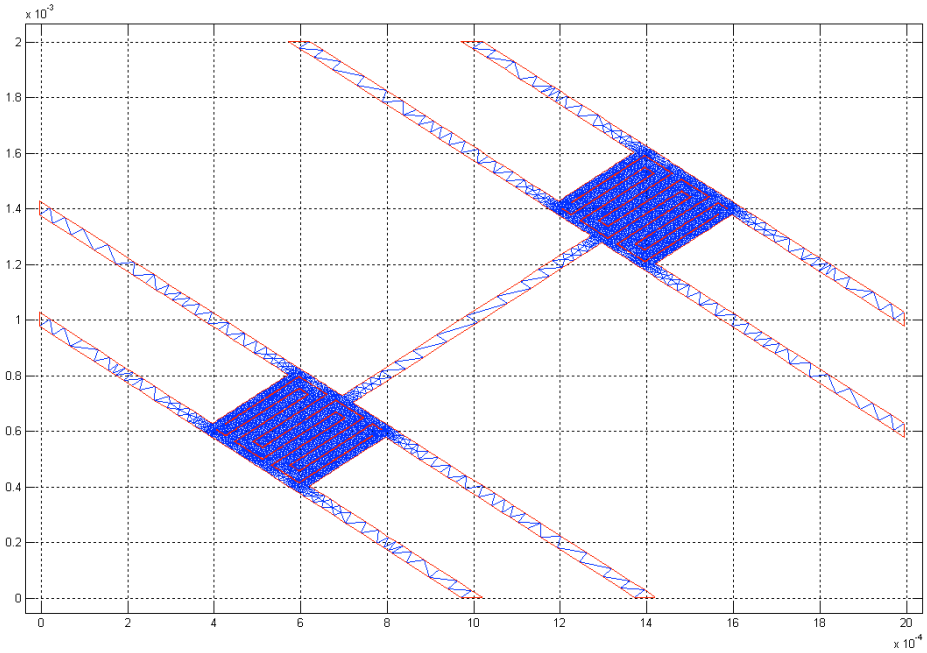

Figure 3.9: Thermal mesh for computing heat flow through a thermal isolation structure

1.7 and the longest refinement method. After establishing the mesh, we then select the correct equation to determine the heat flow. The heat transfer equation in steady state is an elliptic PDE,

$$-\nabla \cdot (k\nabla T) = Q + h(T_{ext} - T).$$

In this equation, k is the thermal conductivity, Q is the heat source or power per unit area, h is the coefficient of convective heat transfer, and T_{ext} is the external temperature. We conduct our experiments in vacuum so h = 0. The heat source $Q = P/L(w)$ is defined as the applied power, which in this case was 1.3 x 10^{-7} W,

divided by the length (l) and the width (w) of the heater wire. Therefore Q = 78 W/m^2. Since this is a 2-D model, we convert k values to k_{2D}. To determine k_{2D}, we multiply k by the thickness of the material, t. The membrane structure is Si-N with molybdenum wiring, so the total k_{2D} will be equal to the sum of both material's k_{2D}. Adding both contributions, $k_{2D,Si-N} + k_{2D,Mo}$ = 1.65 μW/K + 11.4 μW/K, gives k_{2D} = 13.05 μW/K. Finally, we set the boundary conditions for the system. For this model, we selected the Dirichlet boundary conditions which allowed us to specify the temperature on the boundary. The boundary in our model is where the 8 legs connect to the Si frame, and we set T = 300 K.

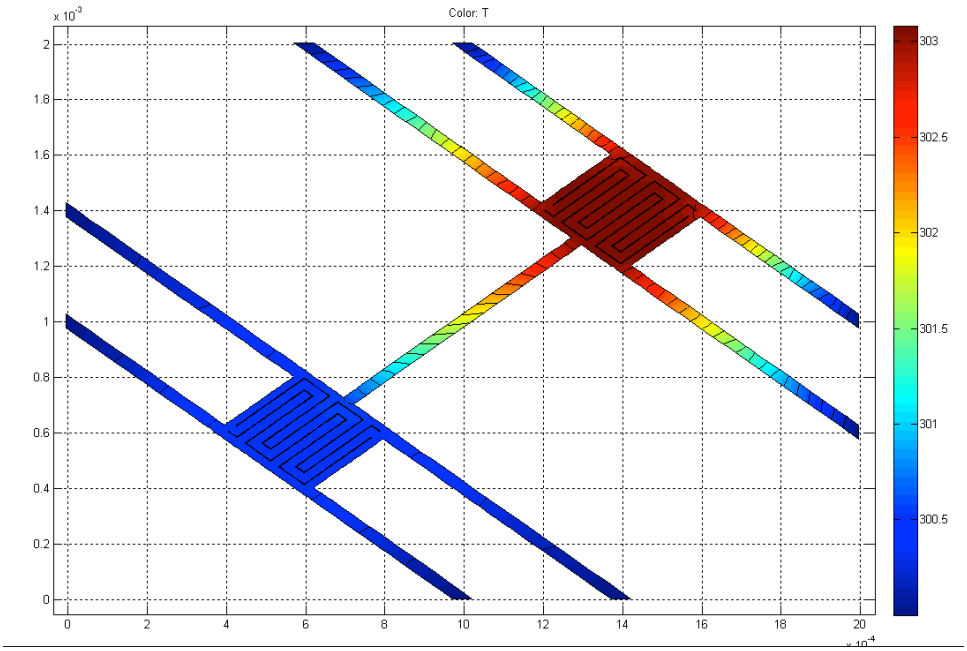

Figure 3.10: Model of the heat flow through a thermal isolation platform. This model was generated using the PDE Toolbox from MATLAB and assumes 2-D heat flow through the structure.

With these inputs we generated the heat flow model shown in Fig. 3.10. Our modeling confirms the heat flow across the bridge and confirms each island is

isothermic to within 0.1 K. It is therefore valid to use the island thermometer values as an indicator of the temperature at each end of the bridge or bridge plus film.

3.2.4 Additional Thermal Conductivity of a Thin Film

After measuring the background conductance of the bridges on several thermal isolation platforms, we deposit thin film samples on the bridges. These films add additional conductance K_{film}. We determine the contribution of the film thermal conductance by repeating the measurement technique applied to the Si-N bridge conductance. Now the conductance between the islands is $K_{total} = K_B + K_{film}$. We subtract the previously measured background conductance from the total conductance to isolate the film thermal conductance, $K_{total} - K_B = K_{film}$. Finally, using the known geometry of the film, we convert the thermal conductance to thermal conductivity, $k = K_{film}(l/wt)$, where l and w are the length and width of the bridge, and t is the thickness of the sample film.

3.3 Lorenz Number Measurement Technique

One of the major advantages of directly measuring thermal conductance using a thermal isolation platform is the ability to measure both thermal conductance and electrical resistance of the same film. Each film deposited on the bridge overlaps the triangle shaped leads pictured in Fig. 3.2. Because the film is in electrical contact with these triangle shaped leads, we can make resistance measurements of the film. In early versions of the platforms, there are 4 metal wires connecting the film through the triangle shaped leads to the external current source and voltmeter. Since the voltage and current leads are separate, the 4 wires remove the lead resistance

typically contributed in 2-wire methods. However, since there are only 2 contacts to the film rather than 4, the contribution of contact resistance, even if small, will still be a source of error in any resistance measurement conducted on early version platforms. Therefore, our method for measuring resistance in early platforms is a quasi-4-wire method. Later versions of the platform include 2 additional contacts to the film enabling a true 4-wire measurement.

Directly measuring thermal and electrical properties of the same film eliminates the error associated with measuring different films when determining the Lorenz number value. The geometry in k and $\rho = 1/\sigma$ cancel leaving measurable extrinsic properties. Since $K = kA/L$ and $R = \rho L/A$,

$$L = \frac{k}{\sigma T} = \frac{k\rho}{T} = \frac{KR}{T}.$$

Therefore, we directly measure the L and compare to L_o predicted by the Wiedemann-Franz law. This gives insight into both the validity of the Wiedemann-Franz predictions for metals and insight into deviations when $L \neq L_o$.

3.4 Thermopower

The sensitivity of our thermal measurements coupled with the ability to measure electrical transport in the same films enables measurements of thermopower as well. The absolute thermopower of a material is very difficult to extract from a measurement because the wires used to measure voltage also have a Seebeck coefficient. One way to measure the absolute thermopower is to measure the sample at low temperatures where the voltage leads are superconducting. However, I conducted

all the experiments presented in this dissertation at temperatures above the critical temperature for molybdenum, and therefore measured relative thermopower. In a relative thermopower measurement, the total thermopower is the difference between the film thermopower (α_{film}) and the thermopower contribution from the leads (α_{leads}), $\triangle V = \int_{T_c}^{T_h}(\alpha_{film} - \alpha_{leads})dT$. Comparison between our measured values for thermopower and literature bulk values indicates that the lead contribution to the thermopower is small. We are planning a series of experiments to infer the thermopower contribution from the Mo leads in order to isolate the film thermopower in previous and future experiments.

To measure relative thermopower, we apply a series of powers and measure the voltage developed in response to the thermal flow through the film. Next we plot $\triangle V$ versus $\triangle T$. The slope of the linear fit to the data is the thermopower, α.

3.5 Summary

We have presented a suspended membrane technique for measuring thermal conductivity, thermopower, and the Lorenz number of thin films. This membrane technique eliminates several sources of error common to thin film k measurements such as radiation effects over 100 K, and isolates the thermal transport in the system to parallel conduction through a low thermal conductance support membrane and the thin film. This is a powerful technique for making sensitive measurements of thermal and electrical transport in thin films.

Chapter 4

Thermal Conductivity and Lorenz Number in Metallic Thin Films

In this chapter we present thermal conductance results for Si-N support bridges as well as electrical resistivity, Lorenz number, and in-plane thermal conductivity results for several ferromagnetic and non-magnetic metallic thin films.

4.1 Si-N Membrane Thermal Conductivity Measurements

4.1.1 Introduction

The first step in our experimental technique to determine thin film $k_{\|}$ is to measure the background thermal conductance contributed by the supporting Si-N membrane bridge. This is a critical step in this measurement technique since we subtract the $K_{\mathrm{Si-N}}$ contribution to the total thermal conductance of a film on membrane

system to determine K_{film}. Although $k_{\mathrm{Si-N}}$ has been measured for bulk samples, $k_{\mathrm{Si-N}}$ for low dimensional geometries such as thin films deviates significantly from bulk values (29, 30, 31). Although $k_{\mathrm{Si-N}}$ is an intrinsic material property, $K_{\mathrm{Si-N}}$ is extrinsic and dependent on the morphology of the material, thus the background $K_{\mathrm{Si-N}}$ can vary widely. One way K can vary is through surface scattering in thin films. This scattering is dependent on the geometry of the thin film and the mean free path of the excitations responsible for heat transfer. In our experiments we have observed variations up to 80% when all our previously measured background $K_{\mathrm{Si-N}}$ values are compared.

4.1.2 Methodology

Both the technique we used to fabricate the Si-N membrane bridges and the experimental method for measuring $K_{\mathrm{Si-N}}$ are described in the previous chapter and by Sultan et al. (32).

4.1.3 Results and Discussion

Fig. 4.1 shows $K_{\mathrm{Si-N}}$ values as a function of temperature for 3 example platforms originating from 3 different Si wafers. The first is an early version of our thermal isolation platform fabricated from 500 nm thick Si-N deposited using LPCVD at the University of California Berkeley. The second platform is a 250 nm thick Si-N membrane deposited using LPCVD at NIST Boulder. The third platform, an updated design for low temperature (LT) measurements, is a 500 nm Si-N membrane deposited using LPCVD at NIST Boulder. In the updated LT platforms we replaced the molybdenum metal thermometers of previous versions with semicon-

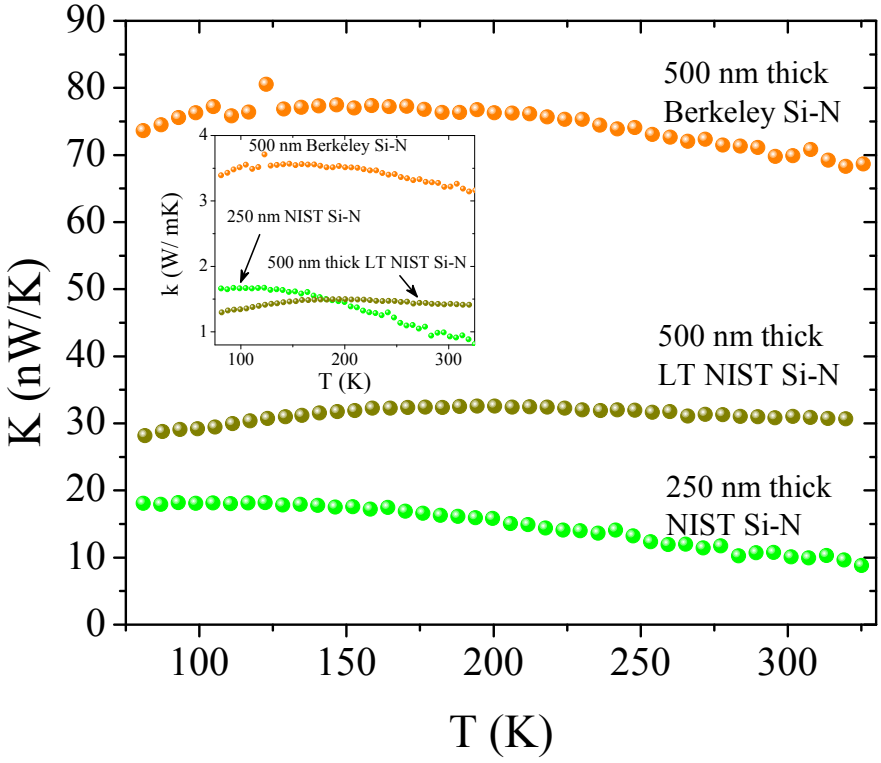

Figure 4.1: Thermal conductance versus temperature of 3 Si-N samples from 3 different wafers. This plot compares K for a 250 nm thick Si-N bridge, a 500 nm thick Si-N bridge, and a 500 nm thick Si-N bridge designed for low temperature (LT) measurements. The room temperature K values range from 10 to 70 nW/K. The inset compares thermal conductivity as a function of temperature for the 3 Si-N bridges.

ducting niobium-silicon thermometers.

The 250 nm NIST Si-N platform has the lowest K as expected, since K is an extrinsic property and the Si-N platform is half the thickness of the other two 500 nm thick membranes. Both versions of the platforms fabricated from NIST Si-N have a lower thermal conductance than the Berkeley Si-N platform. In fact, K values for the 500 nm thick Berkeley platform are roughly 2 times higher than the 500 nm thick NIST LT platform K even though the geometry is the same. The

temperature dependence of the 500 nm thick Berkeley platform is similar to the 250 nm thick NIST platform. However, the temperature dependence of the 500 nm thick LT NIST platform deviates slightly from the other two platforms and appears to flatten out rather than decrease at higher temperatures.

4.1.4 Conclusion

The wide variation in $K_{\mathrm{Si-N}}$ temperature dependence and magnitude exhibited by the various Si-N thermal isolation platform versions underlines the necessity of performing background measurements on each Si-N platform before each subsequent film deposition. Pre-measuring each Si-N platform ensures a more accurate $K_{\mathrm{Si-N}}$ value and significantly reduces the error associated with subtracting this background thermal conduction contribution from $K_{\mathrm{total}} = K_{\mathrm{film}} + K_{\mathrm{Si-N}}$.

4.2 Cu and Fe films

In this section, we present measurements of thermal conductivity, electrical resistivity, and Lorenz number from 77 to 325 K for a 75 nm thick Cu film and compare these results to measurements of a 75 nm thick Fe film.

4.2.1 Methodology

After determining the values for the background $K_{\mathrm{Si-N}}$ contribution using the methodology outlined in the previous sections, we applied the same technique to measure two different 75 nm films. We chose a simple divalent metal, Cu, and a standard ferromagnetic metal, Fe, in order to compare their thermal conductivity, resistivity, and Lorenz number values. We deposited both films via electron beam,

or e-beam, evaporation through micromachined shadow masks in our ultra high vacuum (UHV) deposition chamber. The base pressure of the chamber during Cu film growth was 6 x 10^{-10} torr and increased by a factor of 20 by the end of the deposition. The base pressure of the chamber during Fe film growth was 2.2 x 10^{-8} and increased by a factor of 0.2. Based on the differences in base pressure of the films, the Cu film should be a less disordered film.

4.2.2 Results and Discussion

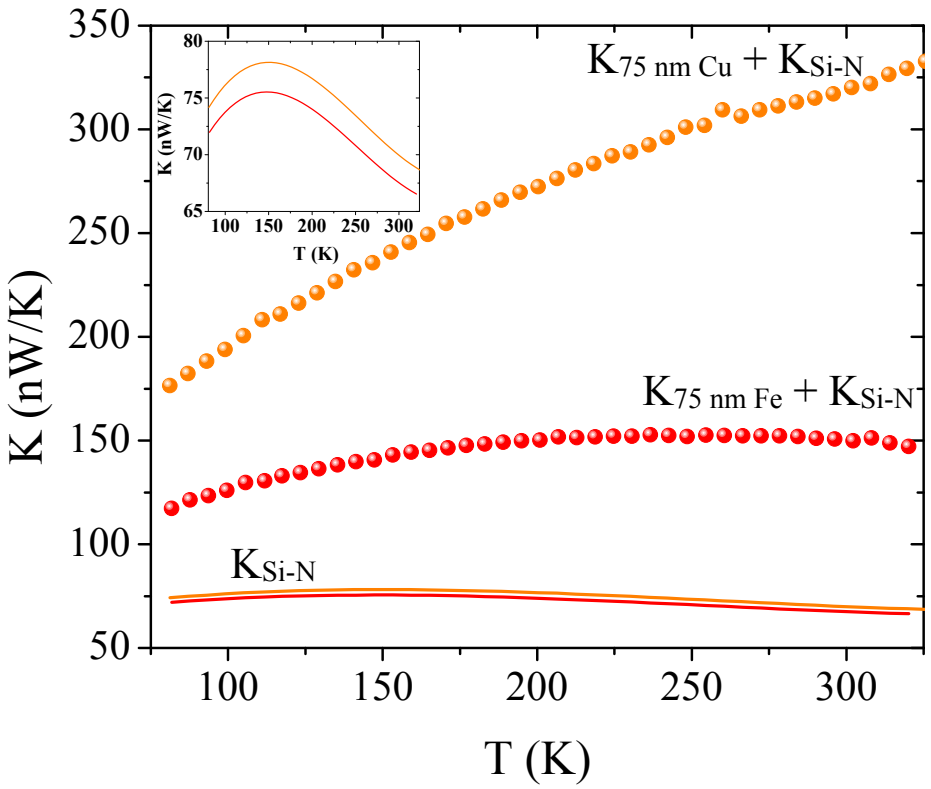

Figure 4.2: Thermal conductance versus temperature for a 75 nm thick Cu film with Si-N background compared to a 75 nm thick Fe film with Si-N background. The inset shows zoomed in data for $K_{\mathrm{Si-N}}$. The $K_{\mathrm{Si-N}}$ polynomial fit generated for each film is represented by a solid line the same color as the K_{total} data for each film.

Fig. 4.2 shows $K_{\mathrm{Si-N}}$ versus temperature for both pre-measured Si-N platforms and K_{total} for both films. The temperature dependence of $K_{\mathrm{Si-N}}$ for both thermal isolation platforms is nearly identical and the difference between the two thermal isolation platform background $K_{\mathrm{Si-N}}$ magnitudes never exceeds 2.5 nW/K. The inset plot in Fig. 4.2 shows a zoomed in view of the background $K_{\mathrm{Si-N}}$. The solid lines in both plots represent the polynomial fits to the measured $K_{\mathrm{Si-N}}$ values.

The additional K contributed by each metal film on both platforms is apparent from the K_{total} values. Although both 75 nm thick films add a large contribution to K_{total}, the magnitude and temperature dependence of the additional K_{Cu} and K_{Fe} vary. K_{Cu} is more than double the value of the supporting Si-N bridge alone and displays a steeper temperature dependence than K_{Fe}. When compared to the cleaner Cu film, the temperature dependence of K_{Fe} appears to flatten out around 150 K. The $K_{\mathrm{Fe}} + K_{\mathrm{Si-N}}$ value at room temperature is less than half that of $K_{\mathrm{Cu}} + K_{\mathrm{Si-N}}$. The nearly identical values for $K_{\mathrm{Si-N}}$ argue that the variation in both the K_{total} temperature dependence and magnitude is a direct result of the additional K_{film}. The increase in K with increasing temperature exhibited by the Cu film is typical of a clean metal film. The Fe appears to have additional scattering that decreases the K value when compared to Cu. We attribute this increase in scattering to increased disorder and the inclusion of defects from the increased base pressure of the UHV chamber during deposition. Finally, due to the ferromagnetic exchange interaction, there are additional spin excitations in Fe known as magnons. These magnons interact with electrons and lower K_{Fe} through electron-magnon scattering.

Fig. 4.3 shows the temperature dependence of $k_{\|}$ for the Cu and Fe films. We determine $k_{\|}$ using K_{film} and the known geometry of the films. The $k_{\|}$ values for both films are typical of ferromagnetic and non-magnetic metallic films of similar

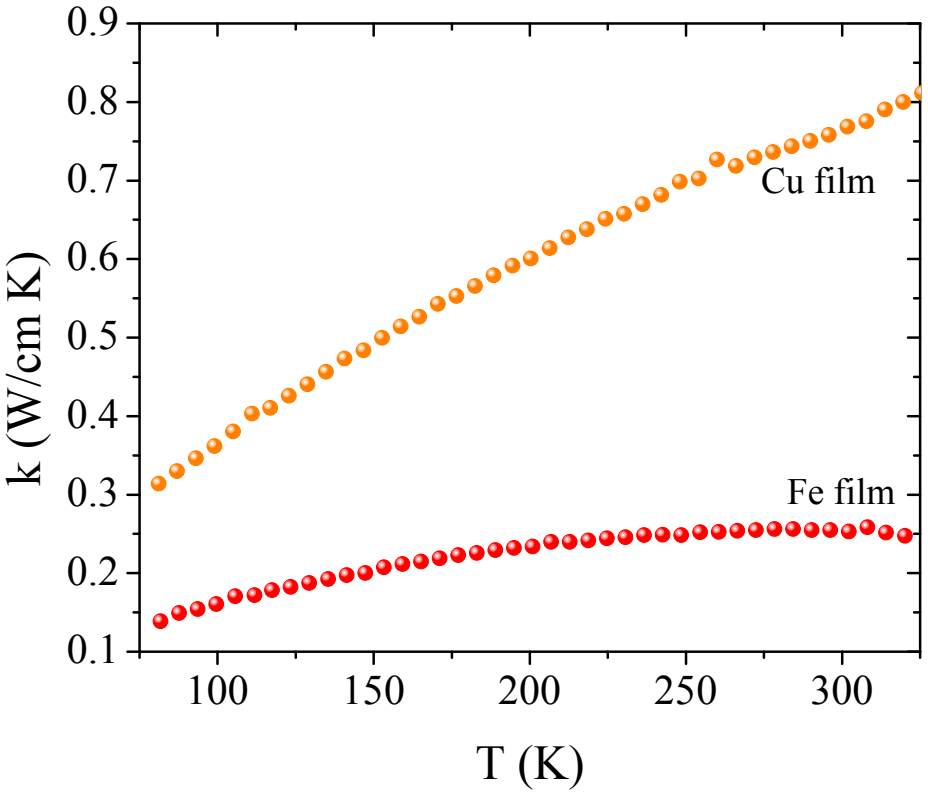

Figure 4.3: In-plane thermal conductivity versus temperature for a 75 nm thick Cu film and a 75 nm thick Fe film.

thicknesses measured using the same technique with $k_{\|}$ values ranging from 0.1 - 0.5 W/cm K (some published in (33)).

For further evidence of additional scattering introduced by magnons and variation in film quality we inspect the resistivity of the films and the Lorenz number values. Fig. 4.4 shows Lorenz number versus temperature with an inset plot of resistivity versus temperature for the Cu and Fe films. As expected from both the UHV chamber conditions during film deposition and the difference in k values for Cu and Fe, the Fe film ρ is greater than the Cu film ρ. The resistivity for Fe also has a steeper temperature dependence than Cu indicating additional scattering that scales with temperature in the Fe.

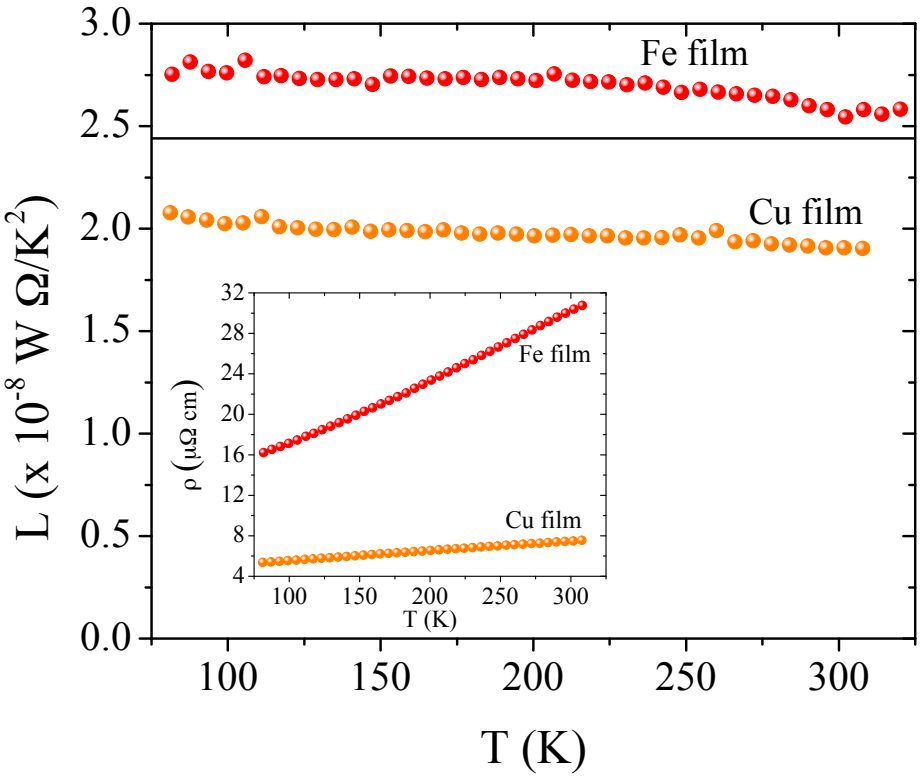

Figure 4.4: Lorenz number versus temperature for a 75 nm thick Cu film and a 75 nm thick Fe film. The solid line represents the Sommerfeld value (L_o), $L_o = 2.44$ x $10^{-8} W\Omega/K^2$. The inset shows resistivity versus temperature.

Comparing the Lorenz number values to the theoretical Sommerfeld value gives insight into the origin of the additional scattering that affects both the electrical resistivity and the thermal conductivity of Fe. Cu exhibits a very slight increase in L with decreasing temperature and has an average value around 2.0 x $10^{-8} W\Omega/K^2$. We have observed L values around 1.9 x $10^{-8} W\Omega/K^2$ in several other metallic thin films with a nominal thickness around 75 nm. The Cu film does not display the expected decrease in L normally observed in bulk metals as a result of an increase in vertical transitions. We currently do not have an explanation for the apparent temperature independence observed in the Cu film. L for Fe is higher than the

Table 4.1: Properties of FM films measured in K and L experiments

Symbol	Material	Method	Thickness (nm)	Growth Rate (nm/s)	Base Pressure (torr)
(a)	Ni	sputtered	50		
(b)	Ni	sputtered	100		
(c)	Ni	evaporated	75	0.1	1.0 x 10^{-8}
(d)	Ni-Fe*	evaporated	75	0.4	2.8 x 10^{-9}
(e)	Ni-Fe*	evaporated	75	1.3	2.4 x 10^{-9}
(f)	Ni-Fe*	evaporated	75	0.52	7.8 x 10^{-9}
(g)	Co	evaporated	75	0.1	3.3 x 10^{-9}

$*$Note: approximate Ni-Fe composition was $\mathrm{Ni_{80}Fe_{15}Mo_5}$

Sommerfeld value. This increase results from an addition contribution to K_{film} from excitations, most likely magnons, in the Fe film. Fe exhibits a slight increase in L with decreasing temperature when compared with the Cu film L rather than the expected drop in L value observed in bulk metals.

4.2.3 Conclusion

In summary, both the magnitude and temperature dependence of k, ρ, and L for the Cu film are typical of a clean non magnetic metal. The increased ρ and resulting k decrease exhibited by the Fe film suggests additional scattering due to increased disorder or inclusion of defects during growth and magnons. Although magnons will scatter electrons, they still transport heat through the film. This is apparent from the shift in Fe L above L_o. Even though the electrical resistivity for Fe is higher than Cu and the thermal conductivity is lower, Fe still showed $L > L_o$.

4.3 Co, Ni, and Ni-Fe Films

In this section, we present measurements of thermal conductivity, electrical resistivity, and Lorenz number from 77 to 325 K for several Ni, Co, and Ni-Fe films with thicknesses ranging from 50 to 100 nm.

4.3.1 Methodology

All of the ferromagnetic films listed in Table 4.1 except for films (a) and (b) were deposited on the thermal platforms via e-beam evaporation through micromachined shadow masks in our UHV deposition chamber. The chamber pressure increased less than a factor of 10 for all films during growth. We sputtered Ni films (a) and (b) on the platform and patterned using photoresist liftoff before we released the platforms during the KOH etching step. To provide the most accurate measurements of film k, we deposited one of the Ni-Fe films after the bridge thermal conductance was already measured. This eliminated any uncertainty in the background conductance which has been shown to vary by several percent even among platforms fabricated on the same wafer (32). We deposited the remaining films in table 4.1, and most of the films measured after these experiments were deposited on pre-measured bridges to enable as accurate a measurement as possible.

4.3.2 Results and Discussion

Fig. 4.5 shows k versus temperature for Ni, Co, and Ni-Fe films compared to literature values for bulk stainless steel (34), bulk Co (35, 36), bulk Ni_3Fe (37), bulk Ni (38), and a Ni nanowire (39). Fig. 4.6 shows resistivity versus temperature

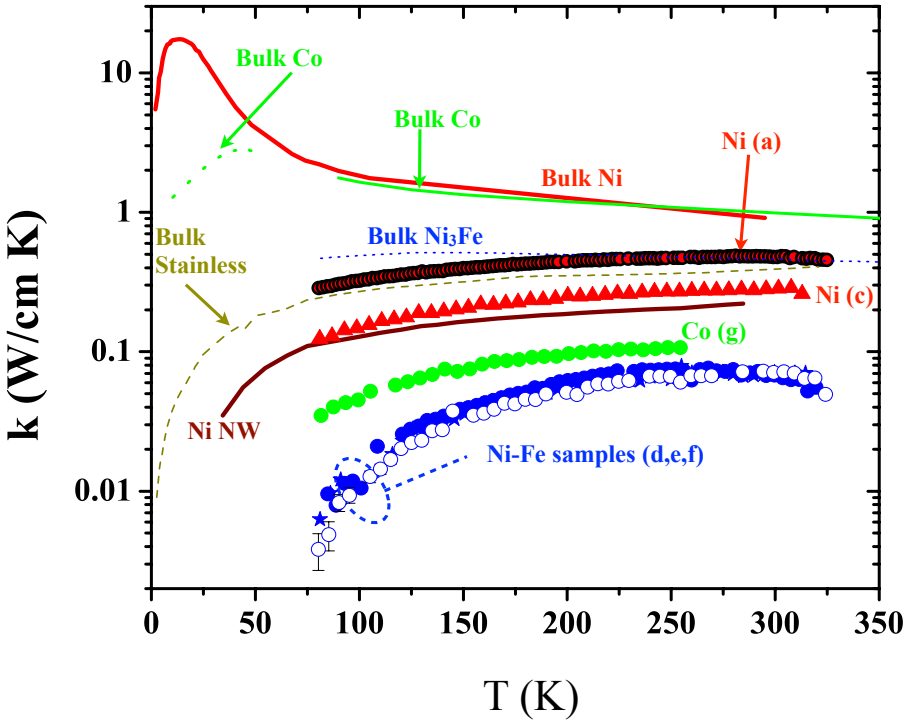

Figure 4.5: Thermal conductivity versus temperature for Ni, Co, and Ni-Fe films from 50 to 100 nm thick compared to literature values.

for the same films compared to a Ni nanowire (39) and bulk Ni (40). k for the Ni films is lower than the bulk Ni k and higher than the k for the Ni nanowire. The resistivity of the 50 nm and 75 nm films is higher than the bulk resistivity and lower than the Ni nanowire resistivity. Since electrons are responsible for the majority of thermal transport in metals, the fact that k for both 2-D Ni films falls between a 3-D bulk Ni sample and nanowire Ni sample is to be expected from the resistivity values. The temperature dependence of k for the Ni films is similar to the temperature dependence of the Ni nanowire but exhibits a large deviation from the bulk temperature dependence. This is further evidence illustrating the inequality between k_{bulk} and k_{film}.

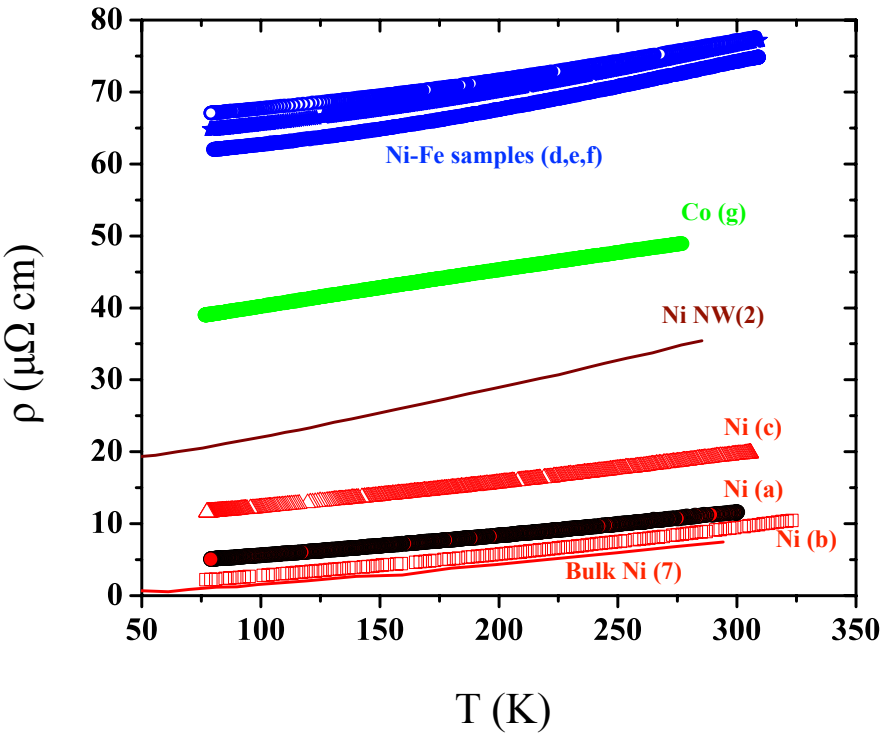

Figure 4.6: Resistiviy versus temperature for Ni, Co, and Ni-Fe films compared to bulk literature resistivity for Ni and a Ni nanowire.

Thermal conductivity for the Co film is lower than bulk Co value reported in the literature and lower than the Ni films as well. ρ for the Co film is higher than ρ for the Ni films. This suggests that the Co has more defects or scattering centers than the cleaner Ni films. These scattering centers introduce additional electrical and thermal resistance. The films with the lowest k values are the Ni-Fe samples. These films also have the highest ρ values when compared to the other films. Though not the same chemical composition, we compare k for the Ni-Fe films to bulk stainless and bulk Ni_3Fe in Fig. 4.5. The values for the Ni-Fe films fall below bulk values

once again. The additional scattering evident from Ni-Fe k values, which were the lowest of all films measured, originates from the inclusion of Fe and Mo atoms which act as additional scattering centers.

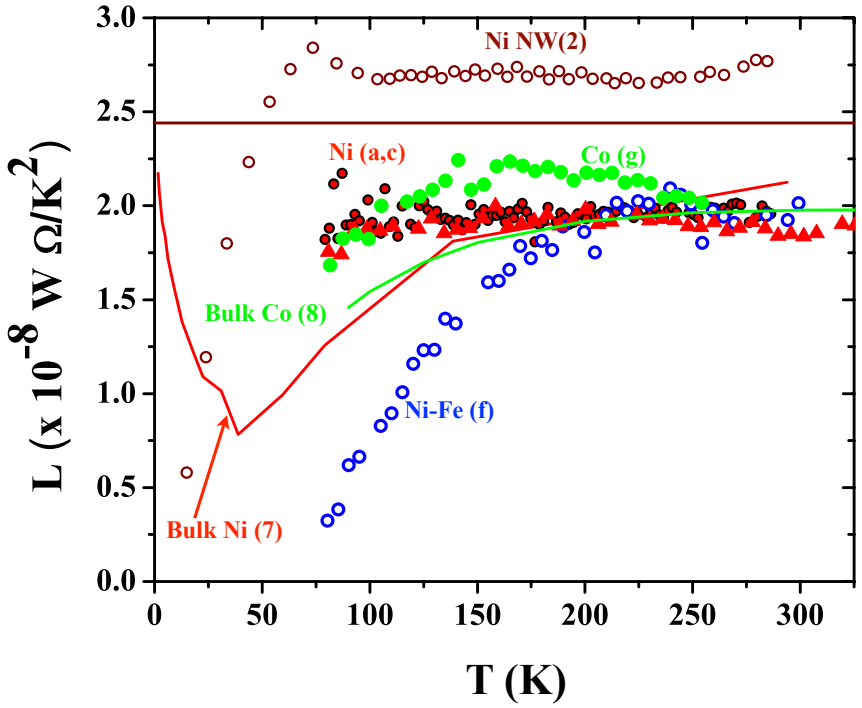

Figure 4.7: Lorenz number versus temperature for Ni, Co, and Ni-Fe films compared to literature values for bulk Ni, bulk Co, and a Ni nanowire. Although the temperature dependence of all 3 Ni-Fe films was almost identical, we display only one sample film for clarity.

Fig. 4.7 shows the temperature dependence of the Lorenz number for Ni, Co, and Ni-Fe films compared to bulk Ni (40), bulk Co (35), and a Ni nanowire (39). The decrease in L from the Sommerfeld value exhibited by bulk metals in the intermediate temperature range due to an increase in vertical transitions is apparent in the bulk Ni data. These vertical transitions affect thermal conduction more strongly than electrical conduction and reduce the k/σ ratio accordingly. Bulk Ni L begins

to return to L_o where horizontal transitions are dominate in the residual resistivity regime through impurity scattering and at high temperatures through scattering from high temperature phonons.

L values for the Ni film match the bulk Ni temperature dependence reasonably well at high temperatures, though the dip in L is not apparent at the low temperatures achievable in a LN_2 cryostat. In fact, L for this 50 nm thick sputtered Ni film is remarkably temperature independent with a value near 1.9 x 10^{-8} $\mathrm{W\Omega/K^2}$. The origin of these behaviors is not immediately apparent. It is possible that either K_{film} or R for the Ni film could be underestimated. However, the 75 nm evaporated Ni film we deposited on a pre-measured background displays a strikingly similar temperature independence at similar value of L. This argues against a randomly underestimated K_{film}. In fact, the similarities in the temperature dependence and magnitude of L for the 50 nm sputtered Ni and 75 nm evaporated Ni films suggest instead that the dominant scattering processes in these films, whether electron-phonon or electron-magnon, are significantly different than those dominant in the bulk sample.

L for the disordered Co film also deviates from the observed temperature dependence of bulk Co. However, in contrast with the temperature independence displayed by the Ni samples, the Co film exhibits a slight increase in L with decreasing temperature. This increase in L could indicate an additional thermal conductance contribution from magnons or phonons, or a reduction in vertical transitions around 175 K.

Finally, the Ni-Fe films exhibit the most dramatic temperature dependence of the films measured in these experiments. Only one 75 nm evaporated Ni-Fe film is plotted in Fig. 4.7 for clarity. However, the other 2 Ni-Fe films omitted from this

figure displayed a virtually identical temperature dependence and L magnitude. L for the Ni-Fe films is the same as as the Ni films from 200 K to 300 K. This is an important result since values of permalloy film k required to model thermal effects in various magnetic devices could be significantly overestimated by using the Wiedemann-Franz law with the typical value of L_o. However below 200 K, the Ni-Fe films exhibit a dramatic drop in L with decreasing temperature. Though we first attributed this drop to an increase in electron-magnon scattering, additional experiments have suggested the drop from 200 K to 77 K could be an artifact due to an underestimation in K_{film}. This underestimation is thought to be generated from a decrease in the bridge background conductance due to additional scattering of heat transporting long wavelength phonons through the Si-N membrane when a film is deposited on the bridge. This reduction in background K will affect films with a low K more dramatically than films with a much higher K. The reduction in background conductance and its effect on the background subtraction will be addressed in the next section.

4.3.3 Conclusion

We have presented thermal conductivity, electrical resistivity and Lorenz number results for several Ni, Ni-Fe, and Co films and compared these to results experimental values for bulk ferromagnets found in the literature. All films exhibited the expected increase in electrical resistivity when compared to their bulk values. All films also displayed the corresponding reduction in thermal conductivity. This decrease in thermal conductivity results from electron scattering since electrons are the dominant heat transport carriers in metals. Finally, all films exhibited a lower Lorenz number value than the theoretical Sommerfeld value. This decreased Lorenz

number indicated the presence of vertical scattering events that affected the thermal current in the ferromagnetic films more strongly than the electrical current.

4.4 Thickness Series Experiments and Background Reduction Effects

In this section, we present experiments designed to probe the drop in thermal conductance observed with the intentional surface roughening of the Si-N supporting membrane bridge. We measure this thermal conductance decrease through a series of experiments designed to gradually reduce the thermal conductance and explore the effect of this $K_{\mathrm{Si-N}}$ reduction on the value determined for K_{film}.

4.4.1 Introduction

In insulators like Si-N, thermal transport is predominately through the propagation of phonons, or lattice vibrations, through the material. Heat transport through disordered insulators is expected to be dominated by short wavelength phonons at our high experimental temperature range, 77 to 325 K. The phonon-phonon collisions experienced by these short wavelength phonons reduces their mean free path to less than microns and they are more likely to be scattered by other phonons than the surface of a micron-scale sample. However, phonons with longer wavelengths are predicted to interact with the sample surface when the wavelengths are of the same length scale. When long wavelength phonons interact with a smooth sample surface, they scatter specularly. Their mean free path is unchanged and they continue through the sample with the same energy. In contrast, a long wavelength

phonon scattering off of a rough sample surface experiences diffuse scattering and a subsequent reduction or change in the value of the mean free path. Previous studies have explored this boundary effect at temperatures below 10 K where long wavelength phonons are expected to be dominant. In these experiments, a Si-N surface was intentionally roughened by depositing particles of silver on the surface. The deposition of the Ag particles caused a significant reduction in $K_{\mathrm{Si-N}}$ (41).

The motivation for this series of experiments comes from the unexpected temperature dependence of L displayed by Ni-Fe and early experiments that explored a reduction in a previously measured value of $K_{\mathrm{Si-N}}$ after a thin film deposition. We first observed this $K_{\mathrm{Si-N}}$ reduction in an experiment designed to measure the k of an amorphous Si (a-Si) film that was expected to have a low K. However, after deposition on a pre-measured Si-N bridge, the K_{total} values for the Si-N bridge plus the a-Si film together were lower than the original thermal conductance of the Si-N bridge alone.

After observing this reduction in the total thermal conductance, we conducted a more thorough examination of this effect by intentionally introducing roughness to the surface using a discontinuous Au film. Depositing 1 nm of Au reduced the background Si-N by 15 to 25%. We then used this reduced background value to determine the conductance of two subsequent Au continuous film depositions 3.5 nm and then 100 nm thick. The results from these studies suggest that there are a larger percentage of long wavelength phonons responsible for thermal transport at our high experimental temperatures than previously thought. A full description of this experiment is in preparation for submission to Physical Review B.

If a reduction in the background thermal conductance is occurring with each film deposition, this will affect the $K_{\mathrm{Si-N}}$, K_{film}, and L values. The error intro-

duced by an overestimated background will have a more significant effect on a low K film than a high K film because it will constitute a larger fraction of the K_{total} value contributed by a low thermal conductance film. The following sections describe two experiments conducted to understand further the impact a deposition will have on $K_{\mathrm{Si-N}}$. We designed the first experiment to determine the $K_{\mathrm{Si-N}}$ reduction threshold using Au particles to add scattering centers to the Si-N surface. The second experiment explored the effect of this reduction on the k and L values determined for a series of Ni-Fe films deposited on the same Si-N bridge using Ni-Fe particles as scattering centers.

4.4.2 Au Methodology

We executed this experiment in a series of steps. In step 1, we began the experiment by measuring $K_{\mathrm{Si-N}}$ of the bare Si-N bridge. After the pre-measurement, we deposited a discontinuous 1.5 nm thick Au layer to intentionally add small scattering centers on the surface of the nitride and remeasured the total background, $K_{\mathrm{total}} = K_{\mathrm{Si-N}} + K_{\mathrm{1.5nmAu}}$ for step 2. For step 3, we repeated the previous step by depositing an additional 1.0 nm of Au, bringing the total to 2.5 nm Au, and remeasured the background. Next, we deposited an additional 3.5 nm discontinuous Au layer. This brought the total thickness of the discontinuous Au layer to 6 nm. We repeated the background measurement again for step 4. In the final step we deposited a 25 nm continuous Au film on top of the 6 nm thick discontinuous layer and measured the K_{total}. We conducted all Au depositions for this experiment in a high vacuum thermal evaporator at 1 x 10^{-7} torr base pressure. For all depositions, the pressure inside the chamber increased no more than a factor of 10. We verified the discontinuity of the Au films by measuring the electrical continuity.

4.4.3 Au Results and Discussion

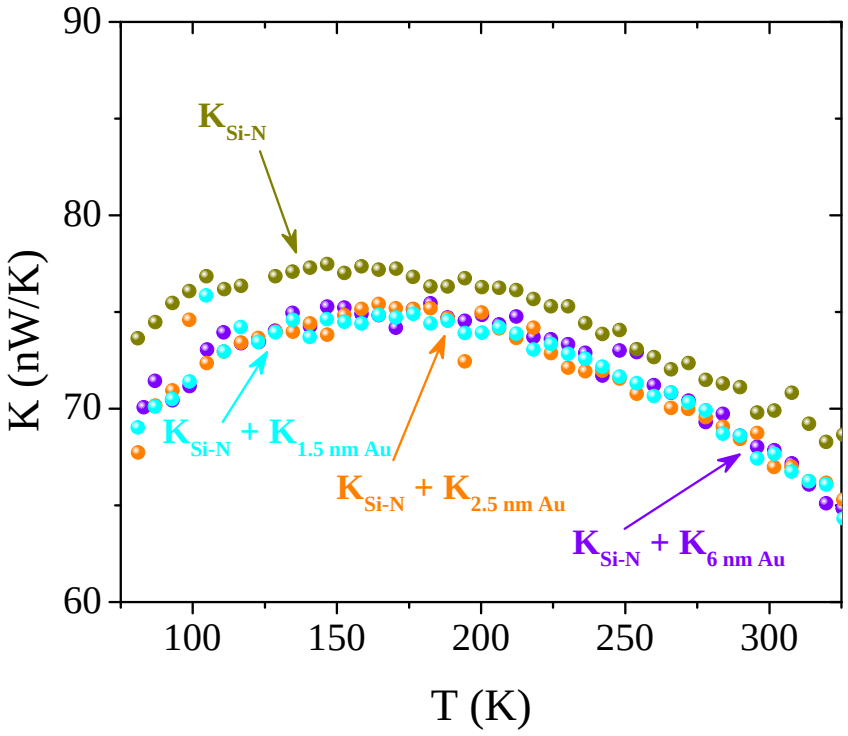

Figure 4.8: Thermal conductance versus temperature for a series of Si-N background measurements after several repeated depositions of discontinuous Au layers.

Fig. 4.8 shows the temperature dependence of the repeated background $K_{\mathrm{Si-N}}$ measurements. The first 1.5 nm Au deposition reduces the $K_{\mathrm{Si-N}}$ background by no more than 7% over the entire experimental temperature range. The next two depositions, 1.0 nm and 3.5 nm, add additional material to the discontinuous Au layer but result in no further reduction of the background K value. The temperature dependencies exhibited by the bare Si-N and all 3 measurements of Si-N with Au particles of increasing thickness up to 6 nm are nearly identical. We attribute this

consistency to the fact that the Au deposited on the Si-N bridge is still discontinuous even at a 6 nm total thickness. Therefore the observed temperature dependence of the background measurements results from the Si-N insulator. The slight decrease in K magnitude is the result of a disruption in the heat transported by long wavelength phonons. Even though a total deposition of 6 nm of Au results in a discontinuous layer that reduces the $K_{\mathrm{Si-N}}$ value, the first deposition of 1.5 nm of material is sufficient to reach the maximum reduction observed for $K_{\mathrm{Si-N}}$.

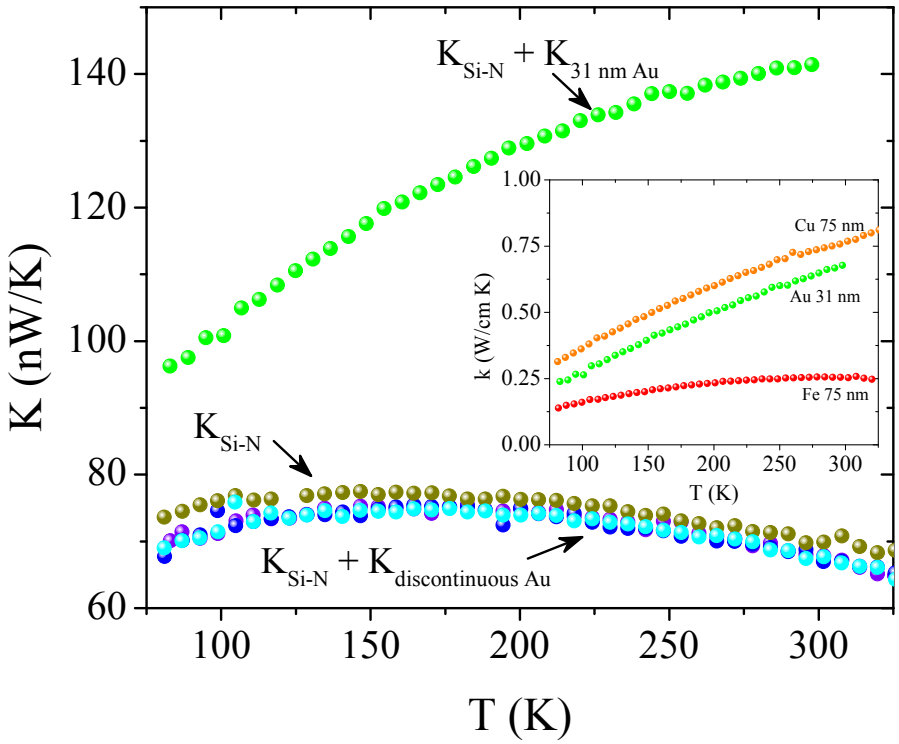

Figure 4.9: Thermal conductance versus temperature for a series of Si-N background measurements after several repeated depositions of discontinuous Au layers and K for an additional 25 nm continuous Au film. The inset is a k versus temperature plot comparing k_{Au} to previously measured 75 nm thick Cu and Fe films.

Fig. 4.9 shows K_{total} after a 25 nm Au film deposition and the background thermal conductances resulting from the discontinuous Au layer versus temperature.

The final 25 nm Au deposition combined with the previous 6 nm thick discontinuous layer add to total a 31 nm thick continuous Au film on the supporting Si-N bridge. The continuous Au film added a significant contribution to K_{total}. The additional K of the metal film is obvious from the modified temperature dependence, which is consistent with the temperature dependence exhibited by similar metals such as Cu. The inset in Fig. 4.9 inset highlights the similarities between $k(T)_{\mathrm{Au}}$ and previously measured $k(T)_{\mathrm{Cu}}$ compared to $k(T)_{\mathrm{Fe}}$. At 80 K where the difference between the backgrounds is most pronounced, K_{film} determined by subtracting the original background value is 22.6 nW/K. In comparison, K_{film} determined by subtracting the reduced background value is 28.5 nW/K, or 26% higher than K_{film} from the overestimated background thermal conductance.

4.4.4 Au Conclusion

From these experiments, we conclude the deposition of a 1.5 nm Au layer is sufficient to reduce the background thermal conductance to the minimum value for this platform. Depositing two subsequent discontinuous Au layers, 1.0 nm and 3.5 nm thick, resulted in no appreciable reduction in the background thermal conductance for this platform. The total reduction of the $K_{\mathrm{Si-N}}$ contribution resulted in a value for K_{film} that was 26% higher than the value determined using the original $K_{\mathrm{Si-N}}$ value measured before reduction. In future experiments of thin films expected to have low K values, at least 1.5 nm of material should be deposited on the Si-N bridge in order to intentionally add scattering centers and reduce $K_{\mathrm{Si-N}}$ to its minimum value. Pre-measurements of the background K should only be conducted after ensuring a thin film deposition will not further diminish $K_{\mathrm{Si-N}}$.

4.4.5 Ni-Fe Methodology

Figure 4.10: Schematic representation of the deposition series performed to evaporate Ni-Fe films of various thicknesses on the same supporting membrane platform. The series of depositions resulted in a permalloy film with a final thickness of 104 nm.

The final series of experiments in this chapter explore the effect of a background K reduction on Ni-Fe k and L measured values. We conducted this experiment in a series of steps similar to the previous Au experiment. In step 1 we measured $K_{\mathrm{Si-N}}$ of a bare Si-N membrane bridge. Next, in step 2, we deposited 4 nm of Ni-Fe on a Si-N platform and repeated the measurement. In step 3, we deposited a 25 nm thick continuous Ni-Fe film, for a total 29 nm of material, and measured K_{total}. For step 4 we deposited an additional 25 nm of Ni-Fe, for a total of 54 nm of Ni-Fe, and remeasured K_{total}. In the final step, we deposited another 50 nm thick Ni-Fe film bringing the total film thickness to 104 nm, and measured K_{total}. We deposited all Ni-Fe films in our UHV chamber through micromachined shadow masks onto a single thermal isolation platform via e-beam evaporation. We measured all films

from 77 to 325 K with the exception of the last 104 nm film. The thermal platform suffered a catastrophic break after 112 K and we were unable to complete the last K measurement.

4.4.6 Ni-Fe Results and Discussion

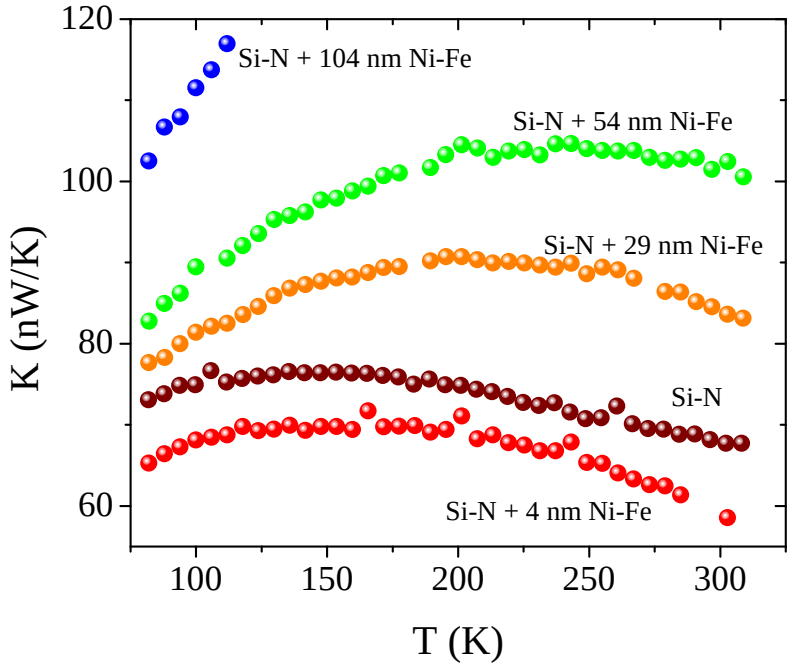

Figure 4.11: Thermal conductance versus temperature for a bare Si-N bridge, the Si-N bridge with 4 nm thick discontinuous Ni-Fe film, with a 25 nm Ni-Fe continuous film, an additional 25 nm Ni-Fe film, and finally a 50 nm film. The final deposition brings the total film thickness to 104 nm.

Fig. 4.11 shows K versus temperature for the entire series of Ni-Fe experiments. The 4 nm thick Ni-Fe particles lower $K_{\mathrm{Si-N}}$ as expected from previous experiments using Au particles to introduce long wavelength phonon scattering resulting in a reduced $K_{\mathrm{Si-N}}$. The total K values resulting from the series of Ni-Fe

film depositions increase as the thickness of the total Ni-Fe increases. The ratio of 104 nm K_{Ni-Fe} to 54 nm K_{Ni-Fe} is approximately 2, as expected since the amount of Ni-Fe on the supporting Si-N was roughly double. The K_{film} value for the 29 nm Ni-Fe film appears high for a film of this thickness when compared to the other two film conductances. The larger K values for the 29 nm film result from this film being cleaner than the 54 nm and 104 nm films deposited later. The difference in

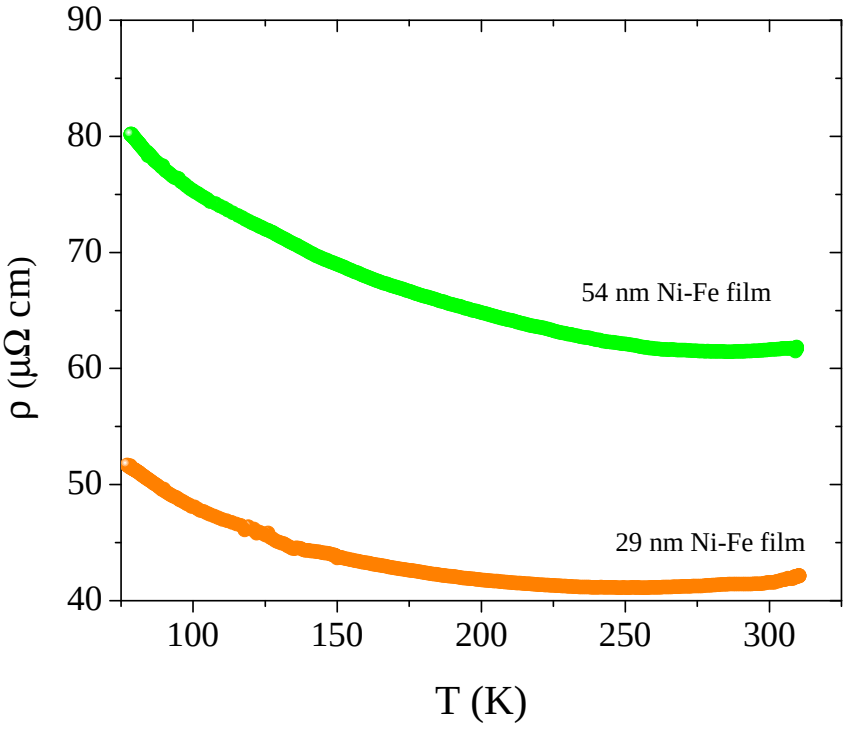

Figure 4.12: Resistivity as a function of temperature for a 29 nm Ni-Fe film compared to a 54 nm film.

film quality is evident from comparing the resistivity values of the 29 nm film and the 54 nm film shown in Fig. 4.12. This results in lower ratios when comparing 104 nm K_{Ni-Fe} to 29 nm K_{Ni-Fe} and of 54 nm K_{Ni-Fe} to 29 nm K_{Ni-Fe}.

It is difficult to comment on the temperature dependence of the 104 nm film

without the full temperature range, but $K(T)$ appears to be scaling as expected for a film of this thickness from 77 to 112 K. The 29 nm and 54 nm thick films also appear to have a temperature dependence typical of metallic alloys of these thicknesses.

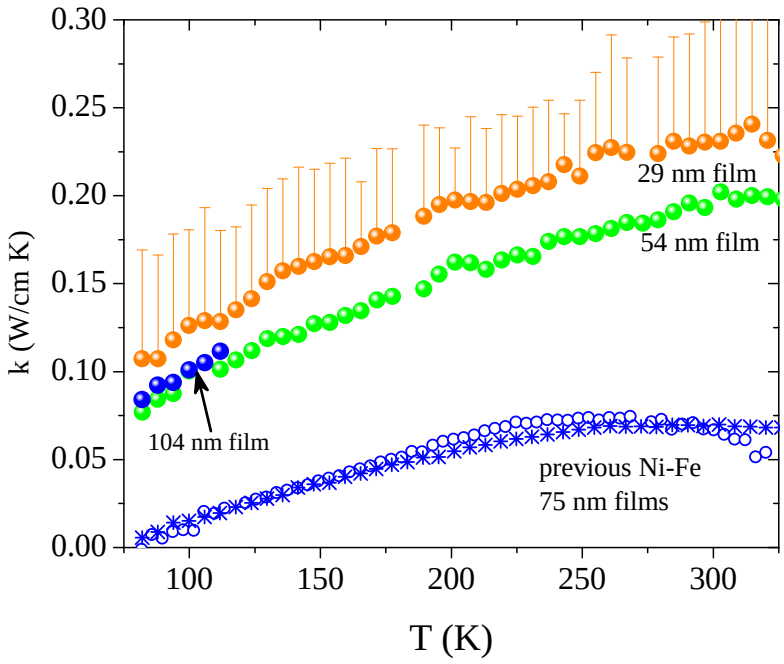

Figure 4.13: Thermal conductivity versus temperature for a series of Ni-Fe films of various thicknesses compared with previously measured 75 nm Ni-Fe films. Error bars represent the possible error generated by subtracting the original Si-N K values rather than the reduced K_{Si-N}

The dramatic impact of the background thermal conductance reduction in these experiments is obvious when comparing k values for this series of films with previous 75 nm thick Ni-Fe k measurements. It is immediately apparent that the overestimation of $K_{\mathrm{Si-N}}$ due to an undetermined background reduction from film deposition results in an underestimation of K_{film}. The thermal conductivity of the 54 nm and 104 nm films is 3 times the value for the previously measured Ni-Fe films.

k for the 29 nm film appears high due to the error associated with measuring this particular film. Contact resistance between the Mo leads for electrical measurements and the Ni-Fe film series prevented us from making an accurate resistance measurements of the films. However, it is evident from the k comparison that this more accurate value for k will have a profound impact on the values determined for the Lorenz number of Ni-Fe films using this methodology.

4.4.7 Ni-Fe Conclusion

In this section, we have presented a series of experiments designed to probe the effect of a reduction in background contribution on the measured k values of Ni-Fe films of increasing thickness. Although K for the 29 nm film was high when compared to the scaled K of the 2 thicker films deposited later, the K values for the 54 nm and 104 nm films scaled with the thickness of the Ni-Fe addition as expected. This improved accuracy in K yielded a higher value for k that was 3 times higher than previously measured Ni-Fe films. If k is underestimated, L will be underestimated and lower L values will appear to be generated through additional vertical transitions that may not be present in the films. In the future, experiments probing Ni-Fe thin films and other films with a low K must account for reduced $K_{\mathrm{Si-N}}$ background effects.

Chapter 5

Thermopower and Resistivity in Ferromagnetic Thin Films Near Room Temperature

5.1 Introduction

Both the established field of spintronics and newly emerging field of spincaloritronics are exploring the next generation of logic and memory devices. Often designed with micro- and nanoscale magnetic samples, these devices are being developed both to improve energy efficiency and increase performance speed. This recent interest has generated increased focus on research into magnetic and thermal effects in a variety of sample types including nanowires used for racetrack memory (9), in multilayered films and nanowires (42, 43, 44), and to manipulate spin degrees of freedom in thin films (45, 46, 14). In order for these new technologies to advance, a thorough understanding of thermoelectric effects in candidate magnetic materials

is necessary.

One important thermoelectric quantity being explored is the traditional Seebeck effect, or thermopower (α), which is the voltage generated across a material when a difference in temperature is maintained at each end. When a temperature bias is applied across a sample, the electrons from the hot end of the sample diffuse into available energy states at the cooler end, setting up a potential difference. The theoretical equation describing α in the free-electron model is the Mott equation

$$\alpha(E) = \frac{\pi^2}{3}\frac{k_B^2 T}{e}\left[\frac{\partial ln\sigma(E)}{\partial E}\right]_{E=E_F} \tag{5.1.1}$$

where

$$\frac{\partial ln\sigma(E)}{\partial E} = \frac{\partial lnA}{\partial E} + \frac{\partial ln\lambda}{\partial E} \tag{5.1.2}$$

In the preceding equation σ is the electrical conductivity of a material, T the temperature, A is the area of the Fermi sphere, and λ is the electron mean free path (47). This equation relates changes in conductivity with changes in energy at the Fermi level and is sensitive to the changes in the number of available scattering centers and in the shape of the Fermi surface. For a more detailed discussion of Eqn. 5.1.2, see chapter 2.

We have recently developed a micromachined thermal isolation platform that is a versatile and powerful tool for probing thermal properties and thermoelectric transport in a wide range of systems,(32) and is particularly well-suited for studies of polycrystalline films ranging in thickness from $\sim 10 - 200$ nm. Though α in thin films can be measured by less involved means, this platform offers several advantages for thermopower measurements. Both the small size of the platform and the ability to make measurements of ρ on the same sample removes uncertainties

related to inhomogeneities between different samples. The small platform size also reduces radiation losses and offers better confidence that thermal gradients are controlled and measured with accuracy. Finally, the symmetry of the thermal platform greatly minimizes or eliminates any additional thermovoltage contribution from the leads that bridge the temperature gradient.

In the following sections, we first explain our measurement technique and layout of the thermal platform. We then present recent thermopower and electrical resistivity results for nickel, iron, permalloy (Ni-Fe), cobalt, and copper films with thicknesses ranging from 60 - 167 nm. Finally, we discuss these results and future directions for probing the fundamental physics governing thermoelectric transport in thin films and other nanostructures.

5.2 Experimental Details

Fabrication of the thermal isolation platform shown in Fig. 5.1, begins with a 500 nm thick layer of amorphous silicon nitride (Si-N) deposited on both sides of a Si wafer by low pressure chemical vapor deposition. A molybdenum layer is sputtered on the top of the wafer and then etched to form heaters, thermometers, and leads. Next, we etch the Si-N layer underneath the metal to form the platform features including two thermal islands, a Si-N bridge, and eight legs. The bridge serves as the thermal link between the two islands, and the legs connect the islands to the thermal bath, or frame. Finally, the entire platform is released by removing the bulk Si below the platform with an anisotropic Si etch. This leaves the Si-N structure suspended over a Si etch pit. Further fabrication details are published elsewhere (32). Each island is patterned with a heater, a thermometer, and a lead for measur-

ing thermopower and resistivity. The frame is also patterned with a thermometer for measuring the reference temperature. At each reference point, a calibration reading is taken of all three integrated thermometers. All resistors, both heating and thermometry, have four wires running to them to allow four-wire measurements.

The first step in our technique is to establish a well-controlled thermal gradient across the platform. We create thermal gradients across the bridge using Joule heating provided by applying a series of currents to the heater on one island. After allowing sufficient time for thermal equilibrium, we measure the resistance of the thermometers on both islands and the frame. We convert from resistance (R) to temperature (T) for each of the thermometers by curve-fitting the T vs R plot for each thermometer. $\triangle T$ is the temperature difference between the two islands. To measure the relative thermopower of a film, we measured the thermoelectric voltage developed across the sample in response to the $\triangle T$. Thermopower is given by the slope of the $\triangle V$ versus $\triangle T$ plot at each reference temperature. For all measurements, we mount the platforms to a temperature-regulated OFHC copper block in a sample-in-vacuum cryostat. The block is surrounded by a copper radiation shield that provides an isothermal environment. The small area of the heated island dramatically reduces radiative heating that is usually problematic over 100 K (32).

The magnetic films were deposited onto the thermal platform and additional separate Si-N substrates using electron-beam evaporation in an ultra high vacuum evaporation (UHV) chamber. The Cu film was thermally evaporated in the same UHV chamber and the 50 nm Ni film was rf sputtered at NIST Boulder. Each film was deposited onto the bridge through a micromachined shadow mask that was aligned to allow the film to overlap the leads for measuring thermopower and electrical resistivity. The samples were grown at pressures between 10^{-7} and 10^{-8}

torr. Resistivities of the substrates were measured using the Van der Pauw method and the film thicknesses were verified using profilometry.

Although the platform design removes lead resistance, it does not eliminate contact resistance. There are only two physical contacts for measuring film thermopower and resistivity on the platform. We have seen evidence of contact resistance after making measurements of the film on the bridge and comparing the film resistivity to the resistivity of a concurrently grown substrate. Successive measurements of resistivity over time have shown a time dependent increase in resistance as well. However, subsequent measurements of film thermopower over time are repeatable. Therefore we do not think this additional resistance is affecting the thermopower of the films.

5.3 Results and Discussion

Fig. 5.2 compares literature values for bulk Ni (48) and Ni-Fe (49) measured thermopower and resistivity results for the following films: 50 nm Ni, 83 nm Ni, two 75 nm Ni-Fe alloys, and a 60 nm Ni-Fe alloy. Both the sputtered and evaporated Ni films display thermopower with the same sign as the bulk Ni (48) and exhibit a temperature dependence similar to that of the bulk, but with smaller magnitude. Of the two Ni films measured, the film with greater disorder, as indicated by resistivity values, showed the smallest values for thermopower. In contrast, the thermopower measurements of Ni-Fe films display dramatically different temperature response when compared to a bulk Ni-Fe alloy reported by Ho et al. (49). The thermopower for these films is negative as predicted, has a smaller magnitude, and a weaker temperature dependence than the bulk sample. One reason for this more complicated

comparison between film and bulk may be the Ni-Fe composition of the films. The experimental permalloy films were not 80% Ni 20% Fe like the literature bulk sample, but evaporated from a ternary alloy with approximate composition 80% Ni, 15 % Fe, and 5% Mo. This difference in thermopower with respect to temperature could be due to additional scattering centers introduced by the Mo. The greater disorder in the alloys contributes additional electron scattering resulting in lower observed thermopower for these films. This smaller thermopower could also be due to changes in the shape of the Ni Fermi surface caused by the Fe and Mo impurities.

Thermopower and resistivity measurements for two Co films, 75 nm and 167 nm, and a 75 nm Cu film are presented in Fig. 5.3 with bulk literature thermopower values for Co (50) and Cu (51). The Co film grown at a base pressure of 6 x 10^{-10} torr has a lower resistivity and larger thermopower than the second Co film grown at a base pressure of 1 x 10^{-10}. The Co film that was grown at a lower base pressure also has a temperature dependence closer to its bulk counterpart. Cu was chosen for its properties as a simple divalent non-magnetic metal. Thermopower for Cu is predicted to be positive because its Fermi surface intersects the boundary of the first Brillouin zone. The measured thermopower for this Cu film is small, positive thermopower as expected. Both Cu and Co films, like the Ni, have smaller thermopower than bulk.

The 65 nm and 75 nm Fe films exhibit positive thermopower with a well defined peak that we attribute to magnon drag. Similar to phonon drag, magnon drag appears when interactions between electrons and the magnon thermal current increase the voltage drop across a material at a given temperature. The two Fe films are plotted with several Fe and Fe alloys from Blatt et al. (48) in Fig. 5.4 illustrating this effect. In the paper by Blatt et al. both magnetic and non-magnetic

metallic impurities diminished but did not destroy the magnon drag effect in bulk Fe. Similarly, our experiments show that magnons in Fe are far less sensitive than phonons to the disorder inherent in our films. Our results are a good indication that magnon drag still makes a clear contribution to thermopower even in disordered thin films. Magnons in the Fe films may also be responsible for the much smaller observed reduction in thermopower magnitude when compared to the other ferromagnetic films in this study. Although magnon drag seems to peak around 175 K in these films, magnons are still present throughout this temperature regime, resulting in larger film thermopower magnitudes in general.

These measurements clearly demonstrate coupling between resistivity and thermopower in magnetic films. Though tempting to explain the reduction in thermopower with changing resistivity using a constant offset or multiplier, the observed differences in both thermopower magnitude and slope illustrate a more complicated relationship between the two quantities.

5.4 Conclusion

We have presented a robust technique for making sensitive measurements of both thermopower and electrical resistivity on a thin film sample. We have discussed experimental results for a simple metal film (Cu) as well as several ferromagnetic films with thicknesses ranging from $60 - 167$ nm. All films measured displayed positive or negative thermopower in agreement with predicted theoretical values. With the exception of the Fe films, the magnitude of thermopower in the films was considerably reduced from values exhibited by similar bulk materials. The Fe films exhibited a smaller reduction in thermopower compared to bulk and

a peak that were attributed to magnon effects in Fe. Along this temperature range, disorder reduces the thermoelectric response to the influx of energy introduced by application of a thermal gradient across the film.

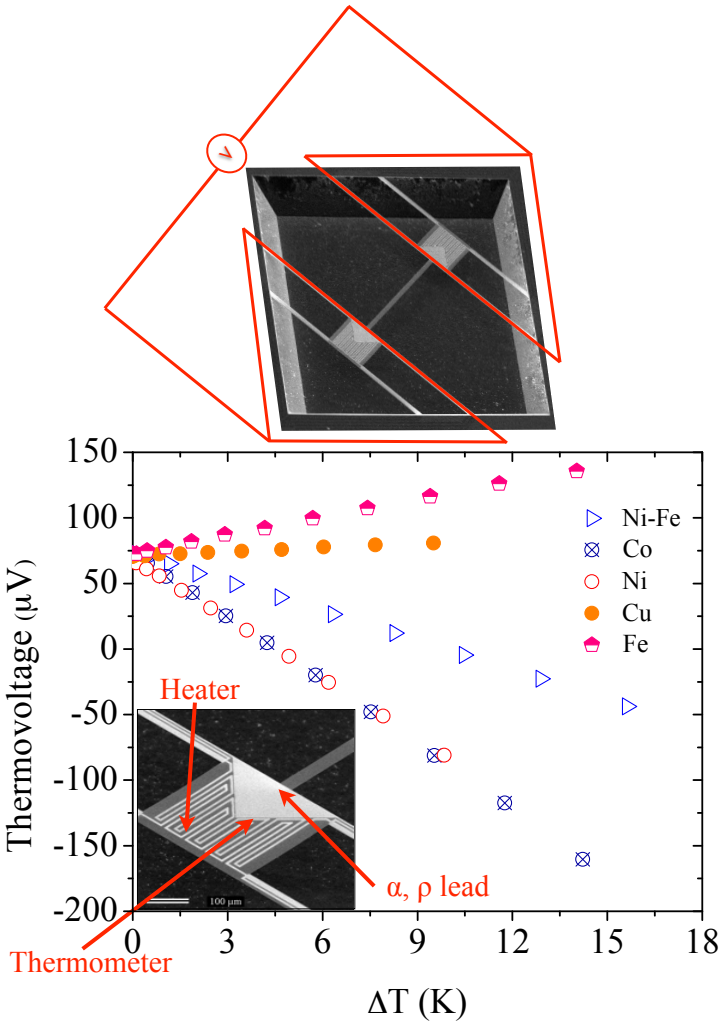

Figure 5.1: Above- Suspended thermal isolation platform with a schematic view of the circuit for measuring thermovoltage. Below- Thermovoltage ($\triangle V$) vs temperature change across the bridge ($\triangle T$) at 299 K for Fe, Cu, Co, Ni, and Ni-Fe films. Inset - close up of the island structure with heater and thermometer wires and the lead for measuring thermopower and resistivity.

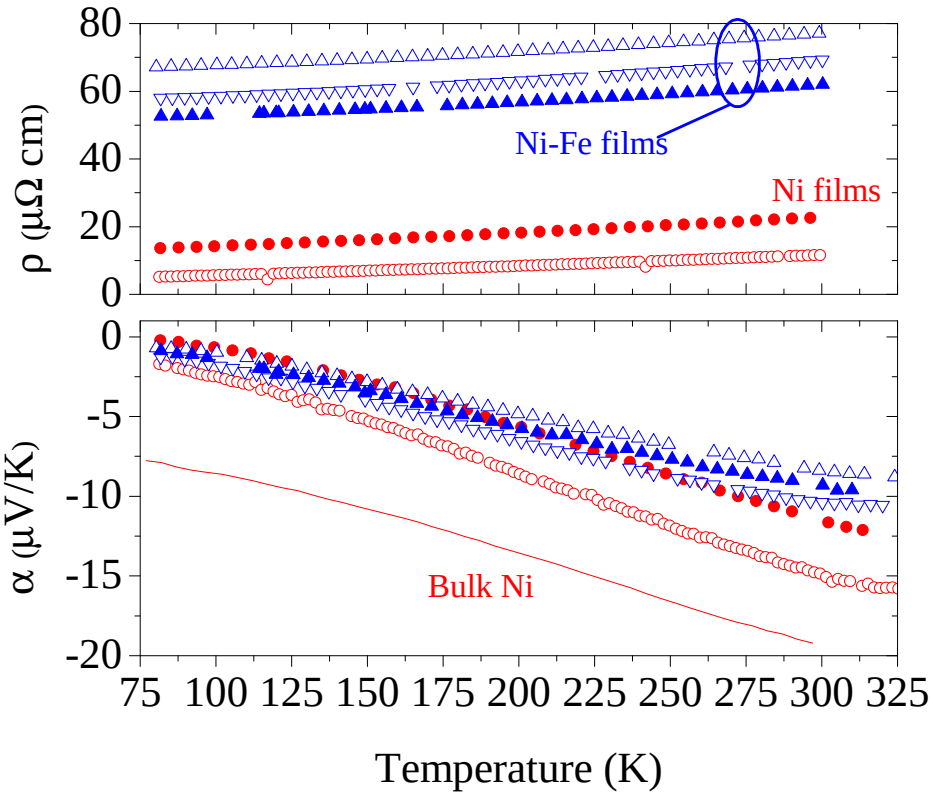

Figure 5.2: (color online) Measured ρ and α of Ni and of Ni-Fe alloy films compared to bulk literature values for Ni and Ni-Fe (solid lines).

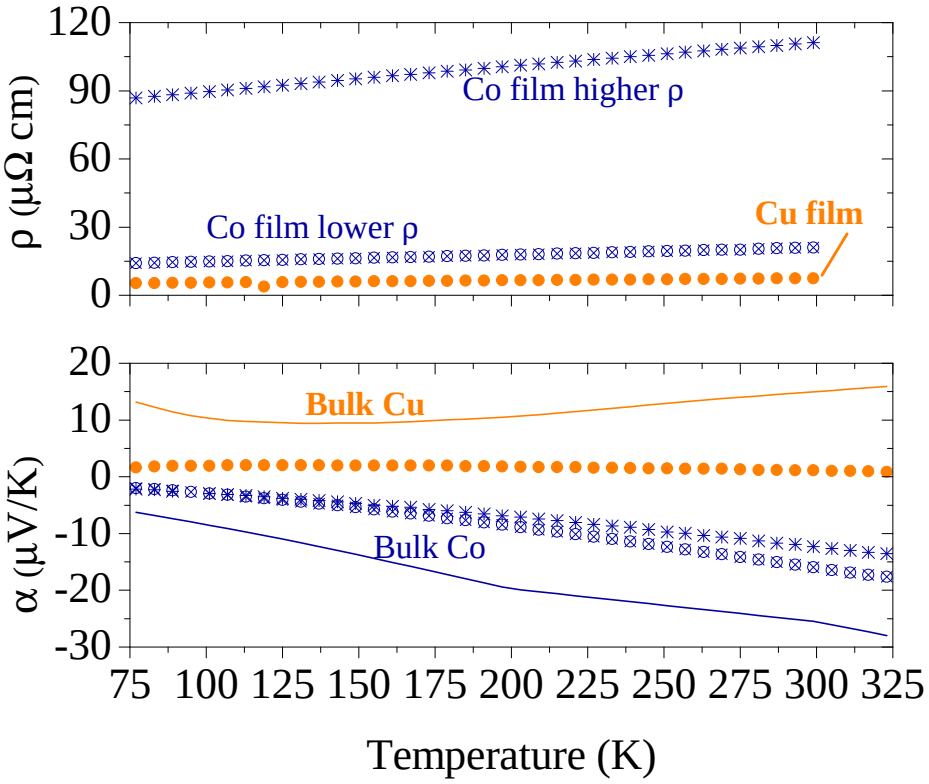

Figure 5.3: Measured ρ and α of Co and Cu films compared to bulk thermopower values for Co and Cu.

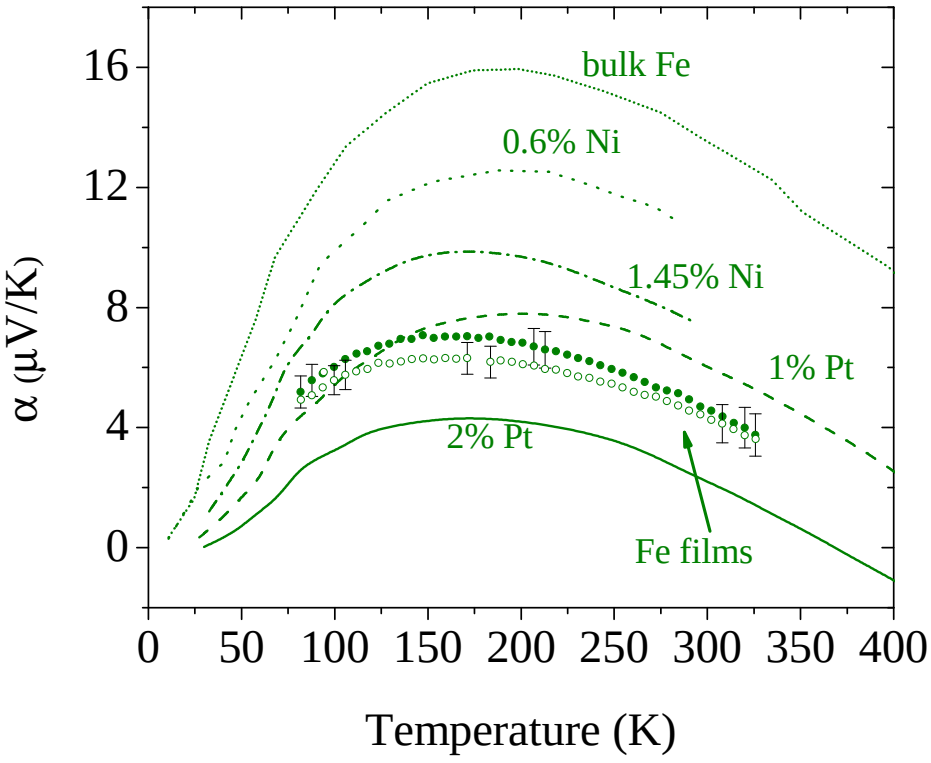

Figure 5.4: Fe α films (circles) compared to bulk data (lines 1-5) from Blatt et al. 1: bulk Fe, 2: 0.6% Ni, 3: 1.45% Ni, 4: 1% Pt, 5: 2% Pt

Chapter 6

Observation of the Planar Nernst Effect

6.1 Introduction

The reliable generation of pure spin currents, transport of angular momentum without movement of charge, is an important step toward a future spin-based nanoelectronics model that could allow computer speed and power consumption to move past limitations of current technologies (11, 52, 53, 54). One possible route toward a source for pure spin currents has been termed the spin Seebeck effect (SSE) (14, 55), where application of a thermal gradient to a ferromagnet causes a spin imbalance which can drive pure spin currents into normal metal contacts. Such coupling between spin and thermal excitations is a rapidly growing area of research that has been given the name "spin caloritronics," (56, 20) and has stimulated interest in a range of thermoelectric and magnetothermoelectric effects.

Some form of the SSE has now been reported for metallic, semiconducting

and insultating ferromagnetic films grown on thick substrates. (14, 45, 57, 15) However, the physical mechanisms responsible for the observed effects are still being debated among both experimentalists and theorists. A key piece of the puzzle could be found in the so-called "longitudinal" spin Seebeck effect (15, 16). In the SSE as originally discussed, shown schematically in Fig. 6.1a, a thermal gradient (∇T) applied along a sample in the $\hat{x}$-direction creates a spin current that flows perpendicularly into normal metal contacts at the sample ends in the $\hat{z}$-direction. For metals with large spin-orbit coupling such as Pt (58), the inverse spin Hall effect (ISHE) (26, 59) causes a charge voltage to appear across the metal contact in the $\hat{y}$-direction. In contrast, observations of the longitudinal SSE were made with applied heat perpendicular to the sample, substrate, and detector strip, so that the resulting ∇T is also in the $\hat{z}$-direction (15, 16). This modified geometry can generate signals as large or larger than those reported in the original SSE observations. Other reports suggest that the SSE signal is strongly dependent on the thermal conductivity of or phonon flow in the bulk substrate itself (18, 17).

Furthermore, recent work on spin-dependent transport in thin film nanostructures on bulk substrates has underscored the difficulty in understanding thermal gradients applied to thin films on thick substrates (60). The size of the longitudinal SSE coefficients, along with the uncertainty that arises concerning the direction of the actual thermal gradient generated on a thin film placed on a thick substrate with overall thermal conductance that is at least a factor of 1000X larger than the contribution of the magnetic sample (60), suggests that the early SSE experiments may have also been affected by both the longitudinal SSE and an anomalous Nernst effect (ANE) contribution.

Progress toward a complete physical picture requires experiments that can clearly

distinguish signals caused by known thermoelectric or magnetothermoelectric effects. For example, in addition to the ANE that can mimic the signatures of the SSE when out-of-plane thermal gradients develop, a transverse thermopower, or planar Nernst effect (PNE), is known in ferromagnetic semiconductors and metals (61, 62). This effect, caused by the same spin-dependent scattering that generates both anisotropic magnetoresistance (AMR) and the standard thermopower, can add a transverse voltage generated by the ferromagnetic material itself in response to ∇T to the voltage potentially generated by the SSE. However, these effects can be separated by their angular dependence. The ISHE used to detect the SSE should produce no voltage when the magnetization is parallel to the Pt strip, and an opposite sign when the applied field reverses the magnetization, leading to a $\cos\theta$ dependence, where θ is the angle between the applied magnetic field (assumed parallel to magnetization M in these samples) and the ∇T vectors. The PNE instead shows a $\sin\theta\cos\theta$ dependence.

In this chapter, we present the first results from a novel approach for examining the spin Seebeck and related effects in ferromagnetic metal films. By using micromachined suspended Si-N membranes, we are able to perform thermoelectric experiments that approach the "zero substrate" limit (32, 33, 63). The 500 nm thick thermal isolation platforms reduce thermal conduction through the substrate by at least 1000x compared to experiments performed using bulk substrates. This confinement to the plane of the platform and film ensures a ∇T in the x- or y-direction only. The experiment therefore explores the SSE in a truly planar geometry. The resulting V_{T} shows some features previously thought to be unique to SSE, but has a field dependence in complete agreement with the PNE, observed here in ferromagnetic metal thin films.

6.2 Methodology

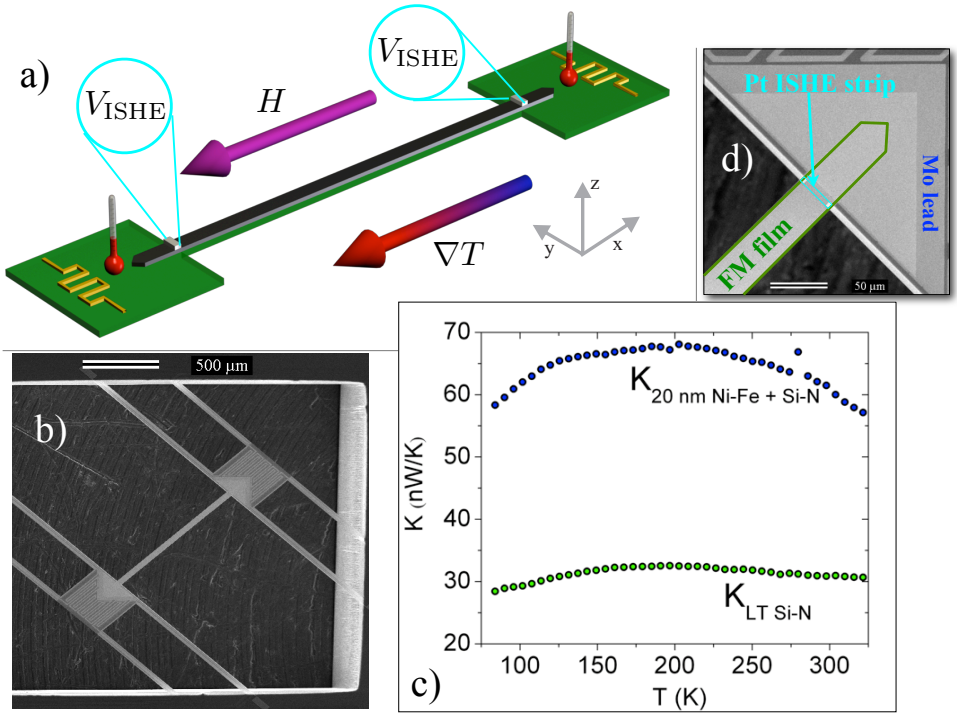

Figure 6.1: (a) Schematic of the thermal isolation platform with ∇T and H applied in the negative x-direction, (b) SEM micrograph of the platform, and (c) plot of thermal conductance vs T for a Si-N bridge and a 20 nm Ni-Fe film deposited on a Si-N bridge. (d) SEM micrograph of one island shows a triangle-shaped lead for measuring film resistance and thermopower, false color outlines show a 20 nm thick Ni-Fe film and a 10 nm thick Pt spin detector.

Figure 6.1 shows a schematic and SEM micrographs of the thermal isolation platform. This platform consists of two suspended Si-N islands connected by a 35 x 800 μm^2 bridge (Fig. 6.1b). A heater and thermometer is lithographically patterned on each island. An additional thermometer is patterned on the frame for monitoring T of the heat bath. The film is deposited on the bridge and overlaps triangle-shaped Mo leads on each island for making measurements of film resistance and thermopower (see Fig. 6.1d).

The thermal platforms are based on structures we use to measure thermal conductivity and the conventional Seebeck effect in thin films and nanostructures (32, 33, 63). The key addition required to probe thermal spin currents are Pt strips to provide detection of spin via the ISHE (59, 26). The sample layer, Pt spin detectors, and their Au leads (with a thin titanium sticking layer) are deposited in three separate steps through lithographically patterned photoresist lift-off masks. This lift-off layer is removed after each deposition and the exposed surfaces are RF sputter-cleaned for several minutes to ensure reliable contact between layers. We use deep trench silicon etching to remove the bulk substrate and thermally isolate the platform. After fabrication, the platform is mounted in a fully radiation shielded Au-plated box in a sample-in-vacuum liquid nitrogen cryostat. ∇T is created along the bridge by applying a known current to the heater on one island. T of each island and the reference T of the frame are determined from the resistance of each thermometer. Every thermometer used is individually calibrated from measurements of R vs. T over the desired range.

To test for the presence of SSE or PNE, we monitor the transverse voltage (V_T) across the Pt strips in response to applied ∇T. When measuring V_{T} we typically observe background voltages of up to several μV that drift slightly over a several minute time-scale, even without an applied ∇T. This expected background is due to thermovoltages produced by conventional Seebeck effects in experimental wiring [1], and its effect can be safely removed from our data. Figure 6.2 shows an example data point taken at 100 Oe (with $\theta = 0$) for one Pt detector. All measurements

[1]This background thermovoltage occurs mainly due to the temperature gradient between the sample held at 276 K and the room-temperature end of the wiring which can fluctuate several degrees. Any length difference in the ~ 0.5 m long manganin twisted pairs will produce imperfect cancellation of the thermovoltage developed across these wires and cause the thermoelectric background.

were conducted at a base T of 276 K. V_T is measured while the sample heater is cycled on and off. The low thermal mass of the platform allows the sample to reach thermal equilibrium in < 1 s. After subtracting a linear fit to the unheated data to correct for thermal drift, we average 20 trials to increase the signal-to-noise ratio. We repeat the measurement after reversing ∇T by heating the opposite island. This allows comparison of the responses for the same Pt strip when hot or cold.

The thermal isolation platforms are designed to be as symmetric as possible to eliminate thermovoltages from unmatched thermal gradients in either direction along the legs, ∇T_{y}. However, variation in the platform materials can cause asymmetries and background thermovoltages that contribute to the measured V_T signal. Measurement of V_{T} while equally heating both islands so that $\nabla T_{\mathrm{x}} = 0$ allows us to determine this background. Once identified (Fig. 6.2c), we subtract it from the voltages measured while heating each island separately ($V_{\mathrm{Hot+Background}} - V_{\mathrm{Background}} = V_{\mathrm{Hot}}$). The response of an example detector to a ∇T_{x}, is shown in Fig. 6.2d), when at the hot and cold end of a sample Ni-Fe film. Note that these signals are symmetric about zero and of opposite sign, demonstrating the spatial reversal thought to be a key signature of the SSE.

6.3 Results and Discussion

Figure 6.3 shows V_T as a function of increasing $\triangle T$ measured at 100 Oe (at $\theta = 0$) for both detectors on a single film when hot and cold, as well as points at $\triangle T = 50$ K for the respective detectors of four additional Ni-Fe films. Though there is a spread in values among the various Pt strips measured, V_T for all samples is linear with $\triangle T_x$ as expected. The voltages are symmetric about zero for each

detector and as shown in Fig. 6.2, the sign of the voltage measured at opposite ends of the film is reversed. These patterns are present in all 12 detectors on 6 Ni-Fe films and 3 detectors on 2 Ni films we measured. All these samples exhibited magnetic field dependence. Figure 6.3b shows an example V_T versus applied magnetic field (H) for a Ni-Fe film. We also tested a platform with a 20 nm thick Au film (see Fig. 6.5) which served as a non-magnetic control and showed neither spatial dependence nor magnetic field dependence.

Fig. 6.4a displays AMR vs H for a Ni film (Ni-a) and Fig. 6.4b shows V_T versus H for a detector when hot and cold in another Ni film (Ni-b). Like AMR, the field dependence of V_T for both Ni-Fe (shown in Fig. 6.3b) and Ni is even. This differs from previous measurements of films on bulk substrates where the field dependence reported for the SSE resembled an M-H curve (14, 45, 15). The coercivity in Ni-Fe and Ni are similar to the AMR peaks measured on these and additional films (Ni-Fe not shown). The background corrected V_T signal for each detector is again approximately symmetric about $V_T = 0$ in both saturation value and peak magnitude [2].

Fig. 6.4c-e presents angular dependence of V_{T} for a Ni film. Figure 6.4c and 6.4d show V_T for one detector on the Ni-b film when cold and hot at values of θ spaced by 45 degree increments (data shown for only one direction of H sweep for clarity). When the detector is cold, V_T is positive for $\theta = 45^\circ$ and 225° with a larger saturation value when compared to saturated values at $\theta = 0^\circ$ and 180°. Rotating the sample an additional 90° generated negative saturation values for $\theta = 135^\circ$ and 315°. Near $M = 0$, V_T values are similar for all angles. Reversal of the applied ∇T changes the detector from cold to hot, but as shown in insets to Fig. 6.4e, also

[2]The background with ∇T_y only was also field dependent. This is caused by the magnetothermopower (MTEP) of the film when heated in the y-direction. A paper presenting MTEP and AMR in FM films has been submitted to *PRB*.

inverts the sign of the PNE component. This effect is shown in Fig. 6.4d, where the pattern of saturated values is reversed from Fig. 6.4c. Fig. 6.4e clarifies this pattern and the overall angular dependence by plotting the V_T in a saturating field of 200 Oe vs. θ for the detector when both cold and hot. Both match the $\sin\theta\cos\theta$ dependence of the PNE extremely well, though with a *field-independent* positive (negative) constant component added when the detector is cold (hot). Again, note the hot data appear to be proportional to -$\sin\theta\cos\theta$ simply due to the negative sign introduced by the reversed ∇T. This sign change is only relevant for the PNE component of V_T, since the pattern of positive V_T for the cold detector and negative V_T for the hot detector is present when ∇T is not reversed.

Data in Fig. 6.4 clearly indicate that the field dependence of the signals in our experiment is entirely explained by the planar Nernst effect. The component of V_T responsible for the sign change on the hot and cold ends of the sample has no field dependence, and is therefore very difficult to interpret as due to a spin current flowing from the ferromagnet into the Pt ISHE spin detectors. Therefore, within the error of our experiment, there is no evidence of thermally generated spin currents, which would add a component to V_T with a $\cos\theta$ angular dependence. This puts an upper limit on the size of the SSE in our planar geometry.

Before discussing the size of the SSE coefficient (S_{s}), we consider other reasons why the SSE might not appear in our experiment. The first concern is the interface between the FM and Pt ISHE detector. Though we have taken steps to assure a high quality contact (RF cleaning of the FM surface before deposition of Pt at pressures of $\approx 10^{-7}$ Torr), it is possible that the interface unintentionally limits the flow of spins into the Pt. It is difficult to probe the quality of the interface directly in our structures, though electrical resistance measurements in various configurations rule

out a large contact resistance that would suggest poor transparency between the Pt and FM. The second concern is that the Mo contacts at the ends of the sample (several μm distant from the Pt) increase the electrical conductance of the structure and partially reduce any transverse voltage. We have estimated the size of this reduction based on the relation between measured longitudinal thermopower (described elsewhere (64)) and the PNE to be ~ 0.4.

Previous reports for Ni-Fe and Ni were $S_{\mathrm{s,Ni-Fe}} = -6 \times 10^{-11}$ V/K and $S_{\mathrm{s,Ni}} = 5 \times 10^{-11}$ V/K (65), where

$$S_{\mathrm{s}} = \left(\frac{2}{\theta_{\mathrm{Pt}}\eta_{\mathrm{FM/Pt}}}\right)\left(\frac{d_{\mathrm{Pt}}}{L_{\mathrm{Pt}}}\right)\left(\frac{V_{\mathrm{ISHE}}}{\Delta T}\right). \tag{6.3.1}$$

Here θ_{Pt} is the spin-Hall angle, $\eta_{\mathrm{FM/Pt}}$ is the spin injection efficiency, d_{Pt} and L_{Pt} are thickness and length of the Pt strip, and V_{ISHE} is the size of the voltage generated on the hot end of the saturated FM sample. Using the geometry of our micromachined platform, $\Delta T = 50$ K, and assuming the same values of $\theta_{\mathrm{Pt}} = 0.08$ and $\eta_{\mathrm{FM/Pt}} = 0.16$ and S_{s} as the previous reports, we would expect an SSE contribution of 56 nV in Ni and 67 nV in Ni-Fe (note that this should appear as an anti-symmetric component in Figs. 6.3b and 6.4b of $2V_{\mathrm{ISHE}}$, due to the expected $\cos\theta$ dependence). If the Mo features partially short this voltage by the expected factor of 0.4, we would still expect a voltage from the SSE of $2V_{\mathrm{ISHE}} \sim 50$ nV. In fact, any SSE component in our experiment is less than the experimental error of ≈ 5 nV. If present, the spin Seebeck effect is significantly reduced in our planar geometry.

6.4 Supplemental Information: Au Experiment

As mentioned briefly in the main text, we also fabricated thermal isolation platforms identical to those used to study 20 nickel and permalloy thin films, but with non-magnetic gold in place of the ferromagnetic samples. Examples of V_T data for this non-magnetic control are shown in Fig. 6.5. Parts a-d of this figure can be directly compared to data for permalloy shown in Fig.6.2 in the main text. The signals generated in the Au sample are entirely explained by small thermoelectric offsets and show none of the signatures of either the spin Seebeck effect or the planar Nernst effect. Specifically, there is no reversal of sign of a V_T component with thermal gradient, and no field dependence.

6.5 Conclusion

In summary, we have used a novel technique to probe the SSE and PNE in the "zero" substrate limit. Though the linear dependence of V_T on $\triangle T$ and the spatial dependence are similar to SSE measurements on films supported by bulk substrates, the magnetic field dependence is entirely explained by the PNE. The upper limit on the SSE coefficient in our experiment is at least an order of magnitude smaller than previous measurements on FM metals on bulk substrates.

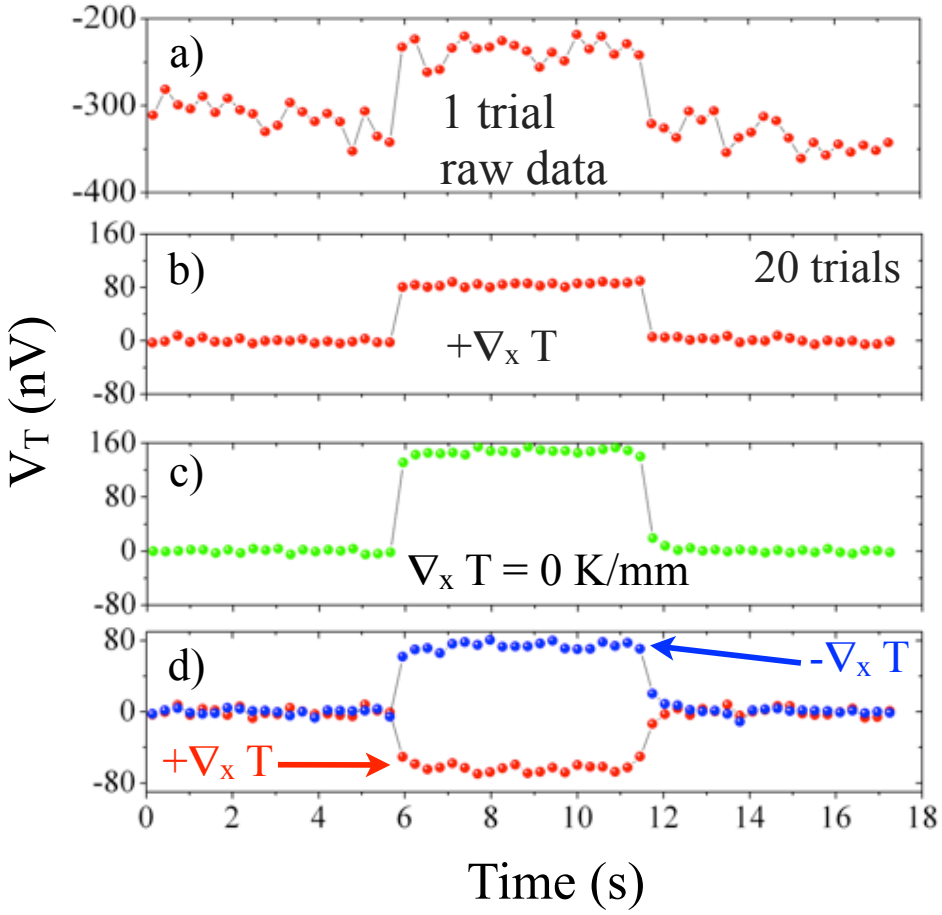

Figure 6.2: (a) Example raw data for V_T across a Pt detector. (b) Averaged data when hot ($\nabla_x T = 62.5$ K/mm, and (c) when both sides of the film heated equally leaving only the background thermovoltage generated by ∇T_y. (d) Hot and cold measurements ($\nabla_x = \pm 62.5$ K/mm) after subtracting the ∇T_y contribution. For all measurements, the heater is cycled on at 6 seconds and off at 11 seconds.

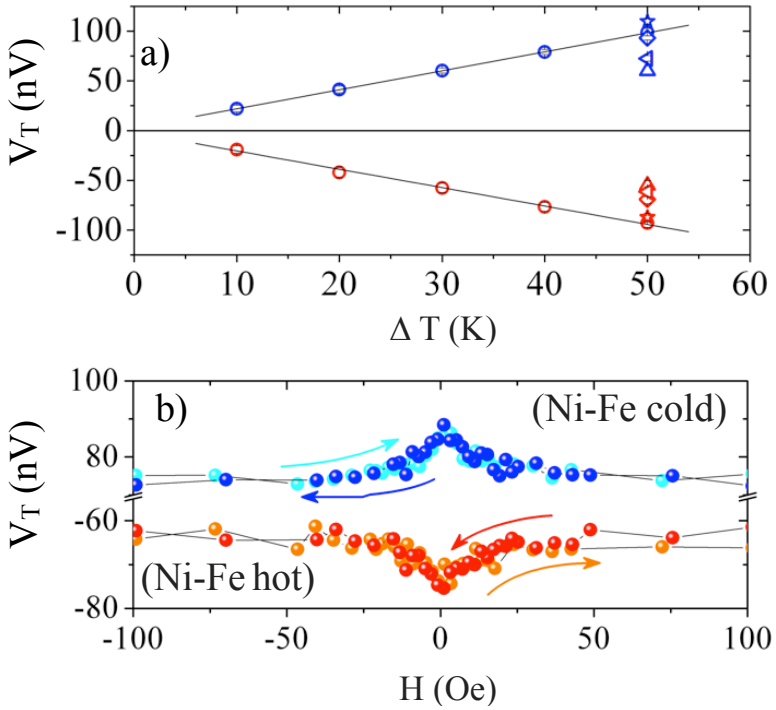

Figure 6.3: V_T versus $\triangle T$ for Ni-Fe ($H = 100$ Oe, $\theta = 0$). a) V_T for one detector when hot and cold with a linear fit. Additional points at $\triangle T = 50$ K are for the same detector on four additional Ni-Fe films. The same trends occur for the other Pt detector (not shown). b) V_T versus H (applied in the $\pm\hat{x}$ direction) for one detector on a Ni-Fe film when hot and cold for up and down H sweeps.

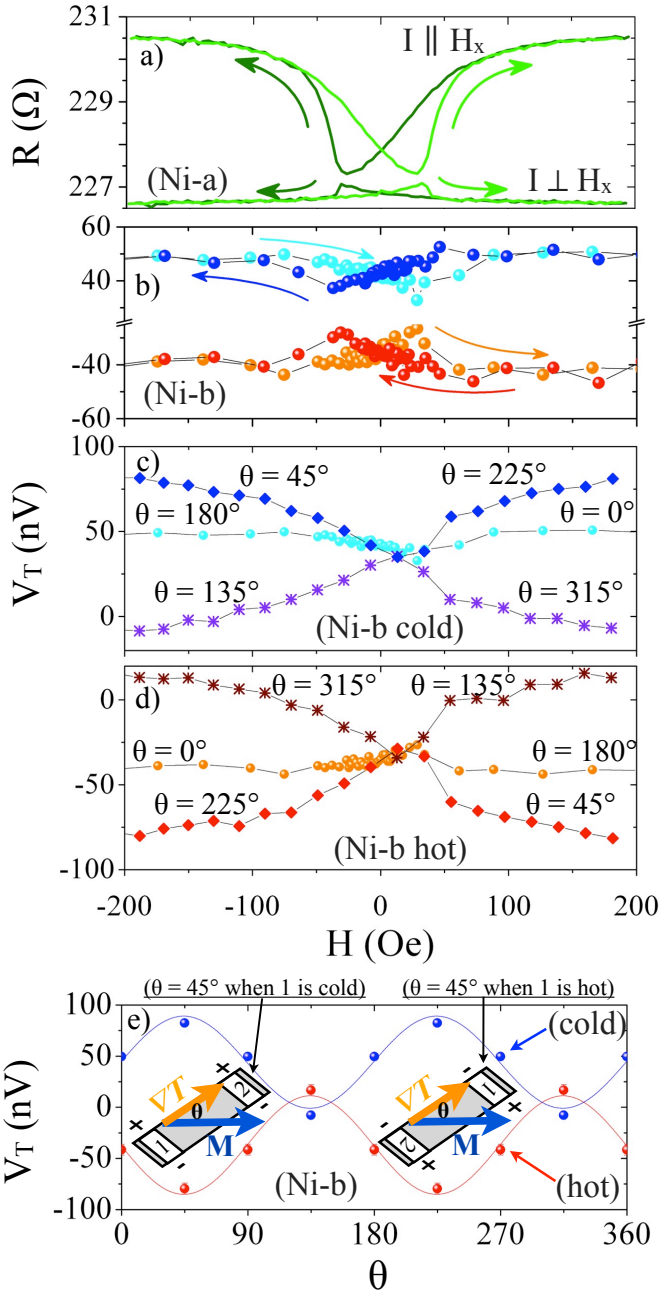

Figure 6.4: a) AMR data for a Ni-a. b) V_T versus H for one detector on Ni-b when hot and cold for up and down H sweeps. c) V_T versus H for Ni-b when cold for one sweep direction at various θ (the angle between M and ∇T and d) when hot. e) V_T vs θ for Ni-b when the detector is hot and cold with $\sin\theta\cos\theta$ fit. Data when hot appear reversed due to the sign change introduced by reversing ∇T *Insets:* Schematics show the sign change for V_T when ∇T is reversed.

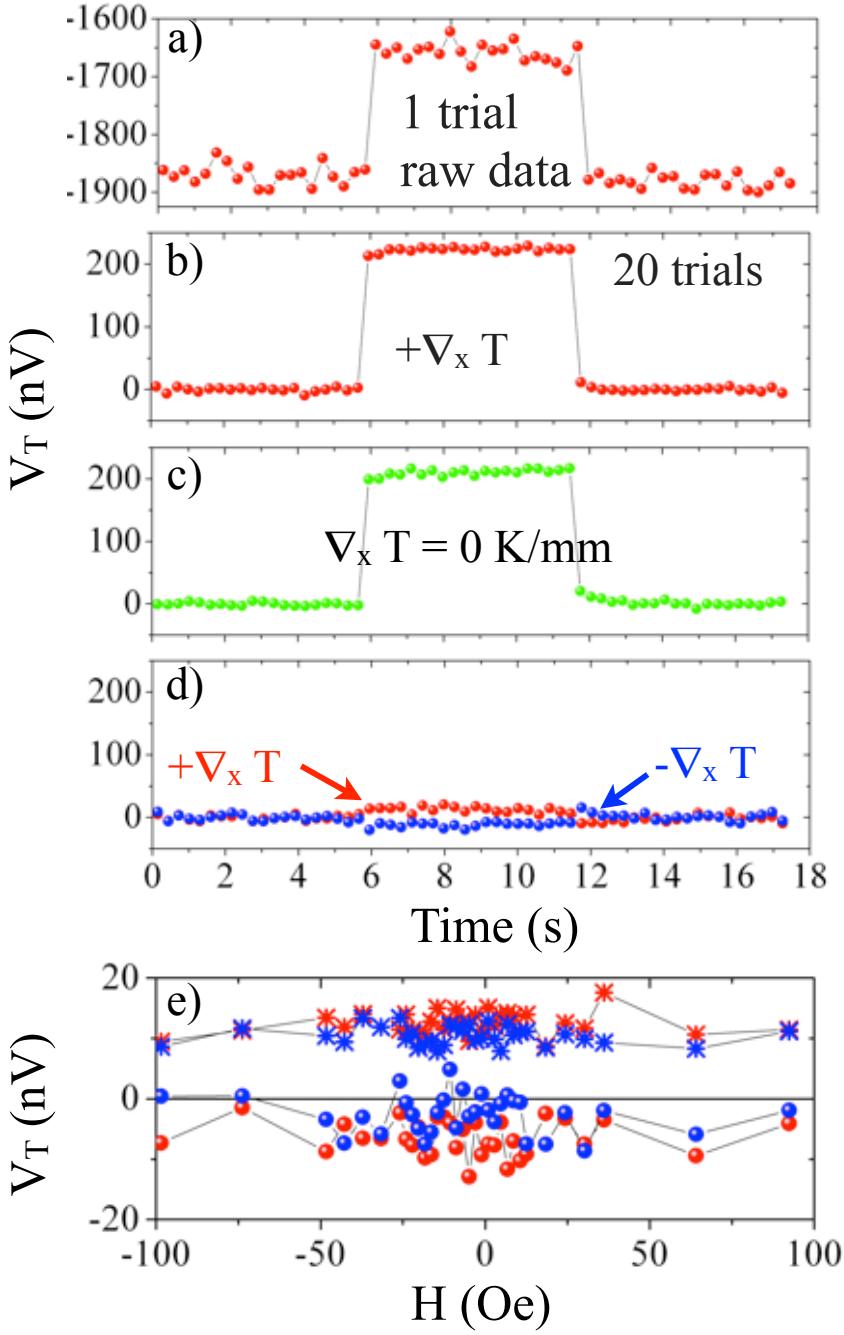

Figure 6.5: (a) Example raw data for V_T across a Pt detector on a Au sample. (b) Averaged data when hot ($\nabla_x T = 62.5$ K/mm, and (c) when both sides of the film heated equally leaving only the background thermovoltage generated by ∇T_y. (d) Hot and cold measurements ($\nabla_x = \pm 62.5$ K/mm) after subtracting out the ∇T_y contribution. For all measurements, the heater is cycled on at 6 seconds and off at 11 seconds. (e) V_T vs. applied field H for the Au sample shows no field dependence.

Chapter 7

Magneto-Thermopower and Anisotropic Magnetoresistance

7.1 Introduction

As the size of traditional logic and storage devices continues to be reduced, the effect of heat on micro-and nanoscale samples has become an important research focus for spintronics, spin caloritronics, and thermoelectrics. Careful characterization of thin film properties is necessary for the development of more energy efficient devices and to clarify the underlying physics governing magneto-thermoelectric properties of ferromagnetic materials. One such effect is the traditional Seebeck effect, or longitudinal thermopower, where a sample develops a voltage in response to a thermal gradient ($\vec{\nabla}T$) applied across the material.

The longitudinal thermopower of a metal, α, is represented by the Mott equation

$$\alpha(E) = \frac{\pi^2 k_B^2 T}{3e}\left[\frac{1}{\sigma(E)}\frac{\partial\sigma(E)}{\partial E}\right]_{E=E_F} \tag{7.1.1}$$

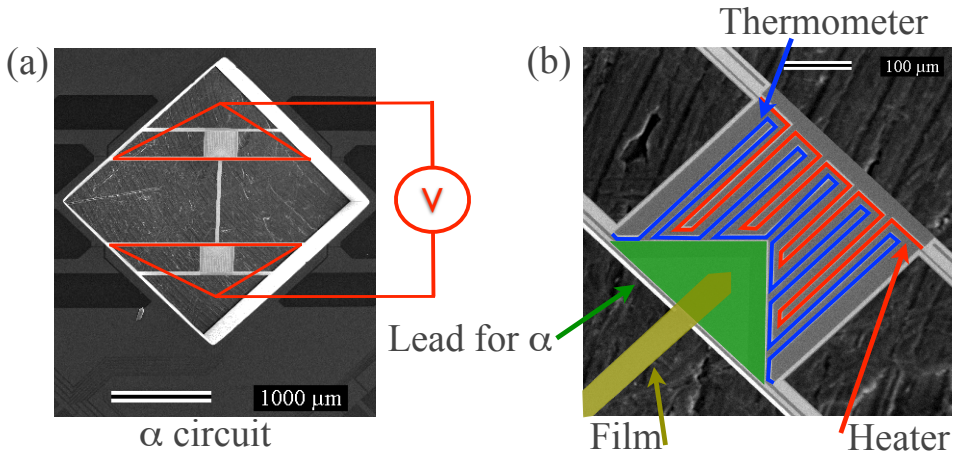

Figure 7.1: **a)** Scanning electron micrograph of a thermal isolation platform with the α circuit shown schematically. **b)** SEM micrograph zoom of one island with leads and film highlighted in false color.

where σ is the electrical conductivity, E_F is the Fermi energy and e is the charge of the carrier and is negative for electrons. After simplifying with natural log, separating the bracketed term into two components gives

$$\left[\frac{\partial ln\sigma(E)}{\partial E}\right]_{E=E_F} = \left[\frac{\partial lnA}{\partial E} + \frac{\partial ln\lambda}{\partial E}\right]_{E=E_F} \tag{7.1.2}$$

where A is the area of the Fermi surface and λ is the mean free path of a charge carrier, electron or hole(22). The sign and magnitude of α depend on the number of scattered electrons, the type of scattering, and the interaction of the Fermi surface with the Brillouin zone boundary. In fact, the sensitivity of α to charge carrier scattering is apparent in an alternate form of the Mott equation expressed as a function of resistivity ρ

$$\alpha(E) = -\frac{\pi^2 k_B^2 T}{3e}\frac{1}{\rho(E)}\left[\frac{\partial \rho(E)}{\partial E}\right]_{E=E_F}. \tag{7.1.3}$$

The interaction between conduction electrons and sample magnetization adds

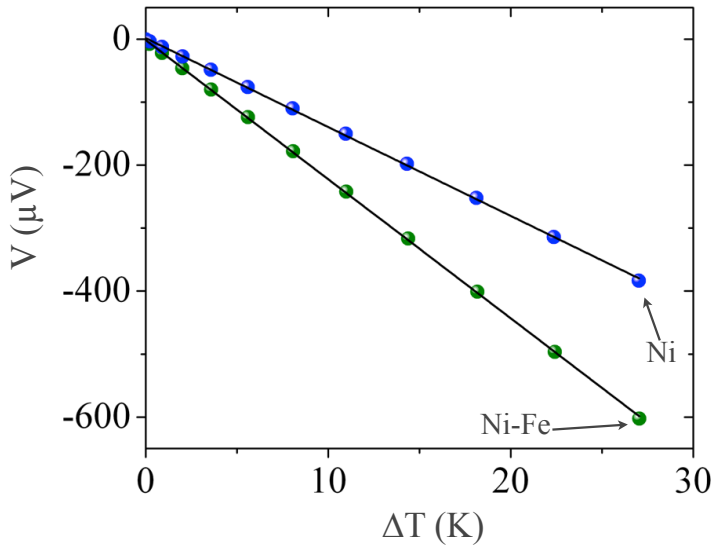

Figure 7.2: $\triangle$T dependence of the voltage generated in response to an applied thermal gradient for Ni-Fe and Ni films with linear fits displayed as solid lines. The slope from the linear fit to the data gives α.

an additional degree of freedom to the thermoelectric properties of ferromagnetic metals when compared with normal metals. One example of this interaction is the anisotropic magnetoresistance (AMR). In AMR, spin-dependent scattering related to sample magnetization generates a change in $R(H)$. The mean free path of the conduction electrons changes with the orientation of the magnetization relative to the direction of the current flow. This interaction between the conduction electrons and the sample magnetization produces an even field dependence in the sample resistance generated by spin-dependent scattering (66). Through $R(H)$, α has an implicit magnetic field dependence along with the energy dependence defined by the Mott equation.

In addition to longitudinal thermopower, ferromagnetic semiconductors and metals exhibit a transverse thermopower also known as the planar Nernst effect, PNE. (61, 62) The PNE is related to the Nernst effect where a magnetic field ap-

plied perpendicular to the plane of a sample and a $\vec{\nabla}T$ in the plane of a sample generates an electric field transverse to the applied $\vec{\nabla}T$. In contrast to the Nernst effect, the planar Nernst effect depends on the angle between the in-plane sample magnetization and the $\vec{\nabla}T$. In the PNE, the resulting electric field is transverse to the direction of the applied $\vec{\nabla}T$. The PNE coefficient is defined by (61)

$$\alpha_{\mathrm{PNE}}(\mathrm{H}) = \frac{1}{2}[\alpha(\mathrm{H}_{\parallel}) - \alpha(H_{\perp})]\sin 2\theta. \tag{7.1.4}$$

In this equation, $\alpha(\mathrm{H}_{\parallel})$ and $\alpha(H_{\perp})$ are longitudinal thermopower coefficients measured in external fields oriented parallel and perpendicular to the applied $\vec{\nabla}T$. θ is the angle between the film magnetization, $\vec{M}$, and $\vec{\nabla}T$. The resulting angular dependence of the PNE is proportional to $\sin 2\theta$.

The spin Seebeck effect is another effect thought to be generated by a $\vec{\nabla}T$ and detected by measuring a transverse voltage, $\mathrm{V_T}$ (14, 55, 45). In the SSE, a $\vec{\nabla}T$ applied across a sample is said to produce a pure spin current that is detected by measuring the $\mathrm{V_T}$ generated through the inverse spin Hall effect. In contrast to the PNE, the SSE is predicted to have a cosine dependence on the angle between $\vec{M}$ and $\vec{\nabla}T$, making it possible to distinguish between these effects using their angular dependence. We recently conducted an experiment designed to measure the SSE in a geometry that limited the $\vec{\nabla}T$ to the plane of the sample film. However, rather than the SSE, we observed the $\sin 2\theta$ dependence generated by the planar Nernst effect (PNE) (67).

Previous studies have explored α(H) in magnetic tunnel junctions (68), multilayered thin films(69, 70, 71, 72) and multilayered nanowires (44, 73). However, few studies have probed single layer thin films. In this chapter, we present $R(H)$,

α(T), and α(H) measurements made on single layer 20 nm thick Ni and Ni-Fe films that are supported by suspended Si-N thermal isolation platforms. We show that the magnetic field dependence for both R and α originates from spin-dependent scattering. Finally, we compare our previous PNE results to the PNE coefficient calculated from the α(H) results, confirming that the origin of the PNE is also spin-dependent scattering.

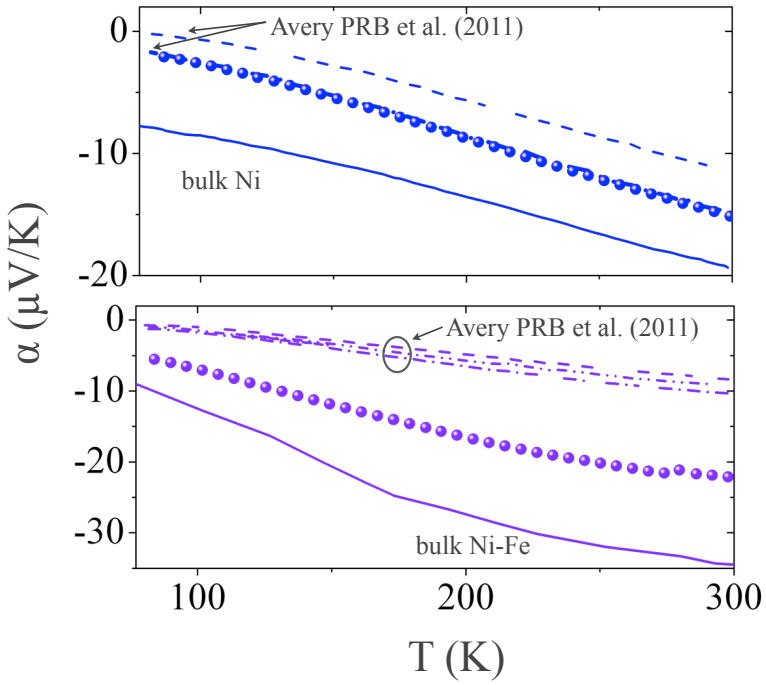

Figure 7.3: Temperature dependence of α for a 20 nm thick Ni (top panel) and a Ni-Fe (bottom panel) film (circles) compared to previously measured films (dotted lines) and bulk literature values (solid lines) for Ni and Ni-Fe.

7.2 Experimental Details

We previously measured α(T), resistivity, and in-plane thermal conductivity of thin films using earlier versions of our thermal isolation platforms(32, 63). However, we conducted our current experiments using an updated platform design that includes a platinum lead at each end of the film. As well as longitudinal thermopower, we can now measure transverse thermopower using these additional leads. We fabricated the platforms and films for this experiment and our PNE experiments (67) at the same time on a single Si-N coated silicon wafer. The thermal platforms used for the current data have the exact same design and geometry as those used for the PNE experiment.[1]

We fabricate suspended thermal isolation platforms using 500 nm thick low-stress Si-N. An SEM micrograph of an example platform and a schematic of our α measurement circuit are shown in Fig. 7.1. Each platform has two islands with integrated heaters and thermometers for applying, maintaining, and measuring temperature gradients. An 800 μm X 35 μm bridge connects the islands and serves both as support for a deposited film and as the only thermal link between the two islands. The platform is suspended and connected to a Si frame by 8 Si-N legs. Fabrication and deposition details are published elsewhere (67). To prevent convective heating, we make all measurements in a sample-in-vacuum cryostat at pressures of 10^{-5} to 10^{-6} torr. We mount the thermal isolation platforms to a gold-plated copper block and wire bond to make connections to room temperature electronics. A radiation

[1]Note that the Pt strip on the top of the sample film is not required for a transverse thermopower measurement. All platforms used in our experiments so far do have this strip, which was designed to test for thermally generated spin currents via the inverse spin Hall effect.

shield encloses the platform before it is inserted into the cryostat to prevent radiative heating.

Figure 7.2 shows an example data point for 20 nm thick Ni-Fe and Ni films at 276 K. To determine α, we measure the thermovoltages generated in response to a series of applied powers and plot V vs. $\triangle$T. α is the slope of the linear fit to the V vs. $\triangle$T plot at each reference temperature. We measured α(T) from 77-325 K. All α(H) and R(H) measurements were conducted at a base temperature of 276 K. For α(H) and R(H), we swept an external magnetic field (H) between $\pm$200 Oe. We applied the external field parallel or perpendicular to the applied I or $\vec{\nabla}T$. We converted measured R into resistivity, ρ, using the known geometry of the films ($\rho = RA/L$).

7.3 Results and Discussion

Figure 7.3 shows α versus temperature at $H = 0$ for a Ni film and a Ni-Fe film compared to previous measurements of similar thin films and to bulk samples (48, 49). The room temperature α value for our Ni-Fe matches the α value for $\mathrm{Ni_{81}Fe_{19}}$ from an earlier experiment reporting the SSE in ferromagnetic metals by Uchida et al.(14) The temperature dependence of α for both films is similar to 60-167 nm thick films measured on an earlier version of our thermal isolation platform using the same technique (63). With one exception, the α and ρ values for the current 20 nm thick films are closer to bulk values than previous films. The 20 nm Ni film has the same α(T) as a 50 nm thick Ni film previously grown in the same chamber. This confirms that any increase in α(T) magnitude towards bulk values stems from fewer defects and impurities in our current films rather than a

thickness dependence, as expected. Electrons dominate conduction in Ni and Ni-Fe alloys(74), resulting in the observed negative α for both Ni and Ni-Fe.

Figure 7.4 shows R(H) and α(H) of a Ni film for external magnetic fields applied parallel ($\mathrm{H}_{\parallel}$) and perpendicular ($\mathrm{H}_{\perp}$) to I or $\vec{\nabla}T$. To differentiate, we denote $\mathrm{R}(\mathrm{H}_{\parallel})$, $\alpha(\mathrm{H}_{\parallel})$, $\mathrm{R}(\mathrm{H}_{\perp})$, and $\alpha(\mathrm{H}_{\perp})$. From R(H) measurements, we determine the Ni film coercivity is $\approx$ 30 Oe. The $\mathrm{R}(\mathrm{H}_{\parallel})$ and $\mathrm{R}(\mathrm{H}_{\perp})$ data confirm that the film magnetization switches as the field is swept. As the film $\vec{M}$ sweeps from fully saturated to $\vec{M} \approx 0$, $\mathrm{R}(\mathrm{H}_{\parallel})$ decreases and $\mathrm{R}(\mathrm{H}_{\perp})$ increases, shown in Fig. 7.4a and Fig. 7.4c. Both $\mathrm{R}(\mathrm{H}_{\parallel})$ and $\mathrm{R}(\mathrm{H}_{\perp})$ exhibit an even field dependence, indicating spin-dependent scattering in the presence of magnetic domains oriented both parallel and perpendicular to the applied current when $\vec{M}$ is zero.

Figure 7.4b and 7.4d show $\alpha(\mathrm{H}_{\parallel})$ and $\alpha(\mathrm{H}_{\perp})$ for the Ni film. The coercivity for both $\alpha(\mathrm{H}_{\parallel})$ and $\alpha(\mathrm{H}_{\perp})$ is $\approx$ 30 Oe as expected from the R(H) data. The $\alpha(\mathrm{H}_{\parallel})$ magnitude increases as $\mathrm{H}_{\parallel}$ is reduced from saturation to coercivity, correlating with the decrease seen in $\mathrm{R}(\mathrm{H}_{\parallel})$. Likewise, the magnitude of $\alpha(\mathrm{H}_{\perp})$ decreases as $\mathrm{R}(\mathrm{H}_{\perp})$ increases. α(H) and R(H) display an inverse proportionality predicted by Eq. 7.1.3 only if the remaining terms on the right hand side are constant. The α(H) data trace the R(H) data in both orientations, suggesting that spin-dependent scattering is the common physical origin.

R(H) and α(H) for a 20 nm thick Ni-Fe film are displayed in Fig. 7.5. For Ni-Fe, both the R(H) and α(H) for parallel and perpendicular external fields exhibit a coercivity $\approx$ 5 Oe. Like Ni, Ni-Fe $\vec{M}$ switches with field and both parallel and perpendicular domains are present at $|\vec{M}| = 0$. However, Ni-Fe has a smaller coercivity than Ni, as expected. As with Ni, Ni-Fe α(H) also increases(decreases) as R(H) decreases(increases), suggesting that α(H) and R(H) for Ni-Fe are related

through spin-dependent scattering.

For quantitative evidence of spin-dependent scattering in α, we convert ρ in Eqn. 7.1.3 to R and examine α(1/R). Figure 7.6 shows α vs. 1/R plots for Ni and Ni-Fe and a linear fit for each. Once the proportionality between α and 1/R is determined, we generate the expected α(H) values and plot them as solid lines in Fig. 7.4b and 7.4d for Ni, and Fig. 7.5b and 7.5d for Ni-Fe. The predicted α(H) lines for Ni and Ni-Fe follow the observed shape of the actual data. This illustrates the direct proportionality between α(H) and 1/R(H). The remaining terms in Eqn 7.1.3 ($\pi^2 k_B^2 T/3e(\partial\rho(E)/\partial E)_{E=E_F}$) are independent of H at a given temperature. Therefore like R(H), the magnetic field dependence of α for a given temperature is due to spin-dependent scattering.

Finally, we compare our results for α and Eq. 7.1.4 to the PNE measurement from our previous experiments (67). In these experiments, we applied a magnetic field at an angle to $\vec{\nabla}T$, for example 45°. Next we swept the field from positive 200 Oe to negative 200 Oe and measured the resulting $\mathrm{V_T}$. This reversed the direction of the field vector resulting in a 225° angle with the $\vec{\nabla}T$. We switched between 135° and 315° using the same method. To calculate $\mathrm{V_T}$, first we determine the transverse thermopower coefficient (α_{PNE}) using Eq. 7.1.4. Since θ is only well-defined at saturation, we use the saturated values $\alpha(\mathrm{H}_{\parallel} = 200Oe) = -13.83\mu V/K$ and $\alpha(H_{\perp} = 200Oe) = -14.03\mu V/K$ for Ni to determine α_{PNE} for all θ. We repeat the process to determine α_{PNE} for Ni-Fe as well. Figure 7.7(a) shows the angular dependence of α_{PNE} for Ni and Ni-Fe for comparison. Although Ni α is smaller than Ni-Fe α at 276K, we calculate a larger α_{PNE} for Ni than Ni-Fe at 276K.

Next we use α_{PNE} to determine $\mathrm{V_T}$. Like the longitudinal thermopower, the

transverse thermopower generates an electric field from an applied $\vec{\nabla}T$. In the longitudinal thermopower, the electric field ($\vec{E}$) is generated over the same geometry as the $\vec{\nabla}T$. These dimensions cancel, leaving a voltage and a $\triangle$T. In the transverse thermopower, $\vec{\nabla}T$ is applied perpendicular to the resulting $\vec{E}$ field,

$$E_y = \frac{V_T}{w} = \alpha_{PNE}\frac{\triangle T}{L}. \tag{7.3.1}$$

In this equation, w is the width of the film, L is the length, and $\triangle$T the temperature difference along the length of the film. This results in an equation that can be solved for the expected transverse voltage (V_T) generated by the PNE. In our experiment, the Pt lead and other metal features partially shorted the ferromagnetic film. This short reduces the expected $\mathrm{V_T}$ by a factor we introduce as a free parameter. This parameter depends on the resistivity and geometry of the Pt, Mo, and ferromagnetic layers as well as the quality of their interface. In order to match the data, the value of the free parameter in our experiment is 0.4. Finally, in the original PNE experiments we measured a $\mathrm{V_T}$ offset at both θ = 0$^{\mathrm{o}}$ and θ = 90$^{\mathrm{o}}$ where PNE is predicted to be zero. PNE data at all other θ appeared to be shifted by this offset as well. To account for the offset, we added the 35 nV offset measured at θ = 90$^{\mathrm{o}}$ in the original PNE experiments. Figure 7.7b shows the calculated PNE $\mathrm{V_T}$ for θ = 0$^{\mathrm{o}}$ to 360$^{\mathrm{o}}$ plotted as a solid line and compared to data from a 20 nm Ni film grown at the same time as our current samples.

Figure 7.8 shows the magnetic field dependence of previously measured $\mathrm{V_T}$ and predicted $\mathrm{V_T}$(H). To predict $\mathrm{V_T}$(H) we determined α_{PNE} for all applied H between $\pm$200 Oe and θ = 45$^{\mathrm{o}}$, 135$^{\mathrm{o}}$, 225$^{\mathrm{o}}$, and 315$^{\mathrm{o}}$. We determined $\mathrm{V_T}$ from the known geometry, $\triangle T$, and α_{PNE}, multiplied by 0.4 and added the 35 nV offset. As mentioned

earlier, the PNE equation is well-defined only when the film is fully saturated. Between $\pm H_{sat}$, $\vec{M}$ is undefined (indicated by dotted lines in Fig. 7.8). However, the Eqn. 7.1.4 prediction reproduces the shape and magnitude of the previously measured PNE along the entire range of applied external field. This close prediction in the intermediate regime where $\vec{M}$ is undefined suggests there is a roughly equal volume of parallel and perpendicular domains over the entire film at field values less than saturation even though individual domain orientation will differ from one field sweep to the next. The predicted PNE V_T has both an angular dependence and a magnetic field dependence that agrees very well with the experimental data. From this agreement, we conclude that the transverse thermopower originates from spin-dependent scattering as well.

Since the origin of the planar Nernst Effect is the same spin-dependent scattering responsible for not only longitudinal thermopower, but AMR, a PNE component should be found in any experiment measuring transverse voltages on ferromagnets that display AMR. For example using α_{PNE} shown in Fig. 7.7a, a Ni-Fe sample with the same AMR and α, with sample width of 4 mm and length of 6 mm with an applied longitudinal temperature difference of 20 K should display a transverse voltage with $\sin 2\theta$ angular dependence and maximum value of 0.9 μV.

7.4 Supplemental Information: sin2θ dependence of α_{PNE}

In this section, we present a short derivation of the $\sin 2\theta$ dependence of the PNE coefficient equation. The equation for the electric field generated by the Nernst effect is $\vec{E} = \vec{\nabla} T \times \vec{M}$. However, because the magnetization of the film $\vec{M}$ and the

thermal gradient $\vec{\nabla}T$ are in the same plane, the cross product between the two is equal to zero and the origin of the planar Nernst effect $\sin 2\theta$ dependence is not obvious. In the following paragraphs, we outline the origin of the angular dependence of the planar Nernst effect.

We begin by outlining a solution to the equation

$$\vec{x} = \vec{a} + [\vec{x} \times \vec{b}] \tag{7.4.1}$$

Using identities from vector calculus, we can solve for $\vec{x}$ by first taking the dot and cross products of $\vec{x}$ and $\vec{b}$

$$\vec{x} \cdot \vec{b} = \vec{a} \cdot \vec{b} \tag{7.4.2}$$

$$\vec{x} \times \vec{b} = [\vec{a} \times \vec{b}] + [[\vec{x} \times \vec{b}] \times \vec{b}] \tag{7.4.3}$$

In general, $[[\vec{a}\times]\vec{b} \times \vec{c}] = \vec{b}(\vec{a} \cdot \vec{c}) - \vec{a}(\vec{c} \cdot \vec{b})$. Using this identity to simplify Eqn. 7.4.3 we get

$$\vec{x} \times \vec{b} = [\vec{a} \times \vec{b}] + \vec{b}(\vec{x} \cdot \vec{b}) - \vec{x}(\vec{b} \cdot \vec{b}). \tag{7.4.4}$$

Substituting this expression and $\vec{x} \cdot \vec{b} = \vec{a} \cdot \vec{b}$ into Eqn. 7.4.1 gives

$$\vec{x} = \vec{a} + [\vec{a} \times \vec{b}] + \vec{b}(\vec{a} \cdot \vec{b}) - \vec{x}(\vec{b} \cdot \vec{b}). \tag{7.4.5}$$

After simplification, we finally have an equation for $\vec{x}$ in terms of $\vec{a}$ and $\vec{b}$.

$$\vec{x} = \frac{\vec{a} + [\vec{a} \times \vec{b}] + \vec{b}(\vec{a} \cdot \vec{b})}{(1 + b^2)} \tag{7.4.6}$$

The expression for the electric field generated through the Hall effect has three components that can be expressed in the form of Eqn. 7.4.6. In the hall effect,

the Lorentz force preferentially scatters the electrons to one side of a sample. $\vec{F} = q(\vec{E}+[\vec{v}\times\vec{B}])$. This scattering results in a steady state electric field $\vec{E_H}$. Multiplying the force $q\vec{E_H}$ by the number of electrons (n) and the electron mobility (μ) gives the electron current density

$$J(\vec{B}) = \sigma\vec{E} - \mu[J(\vec{B}) \times \vec{B}]. \tag{7.4.7}$$

This is the basic equation that relates the three quantities necessary for the Hall effect, $\vec{J}$, $\vec{B}$, and $\vec{E}$. In the most general case, the magnetic induction is not constrained to the z-axis. This case is shown in Fig. 7.9. We can use the results from Eqn. 7.4.6 to generate a solution to this equation

$$J(\vec{B}) = \left(\frac{1}{1+\mu^2B^2}\right)\left(\sigma\vec{E} + \mu\sigma[\vec{E}\times\vec{B}] + \mu^2\sigma\vec{B}(\vec{E}\cdot\vec{B})\right). \tag{7.4.8}$$

$\sigma\vec{E}$ represents the drift current density when $\vec{B} = 0$. This is the component along the applied current. The second term, $\mu\sigma[\vec{E}\times\vec{B}]$, is perpendicular to both $\vec{B}$ and $\vec{E}$. The third term, $\mu^2\sigma\vec{B}(\vec{E}\cdot\vec{B})$, is collinear with $\vec{B}$ in the generalized geometry.

For clarity, we can rewrite Eqn. 7.4.8 in a more compact form

$$\vec{E} = \rho_b\vec{J} - R_H[\vec{J}\times\vec{B}] + P_H(\vec{J}\cdot\vec{B})\vec{B} \tag{7.4.9}$$

where ρ_b is the magnetoresistivity, R_H is the Hall coefficient, and P_H is the planar Hall coefficient. Simplifying the collinear component gives

$$\vec{E_B} = P_HJB^2\cos\theta\hat{B} \tag{7.4.10}$$

where θ is the angle between $\vec{J}$ and $\vec{B}$. The component of $\vec{E}$ in the y-direction is then

$$\vec{E_y} = (\vec{E_B} \cdot \hat{y})\hat{y} \tag{7.4.11}$$

$$= E_B \cos(90 - \theta)\hat{y}$$

$$= P_H J B^2 \cos\theta \cos(90 - \theta)\hat{y}.$$

Using the trigonometric identity, $\cos(\frac{\pi}{2} - \theta) = \sin\theta$, $\vec{E_y}$ becomes

$$\vec{E_y} = P_H J B^2 \cos\theta \sin\theta \hat{y}. \tag{7.4.12}$$

Finally, using the trigonometric identity $\cos\theta\sin\theta = \frac{1}{2}\sin 2\theta$, we can express the equation for the planar Hall effect electric field as a function of $\sin 2\theta$,

$$\vec{E_y} = \frac{1}{2} P_H J B^2 \sin 2\theta \hat{y}. \tag{7.4.13}$$

The Nernst effect is the thermal analog to the Hall effect. Simply replacing the applied current with the thermal gradient, the magnetic induction with the magnetization, and the planar Hall coefficient with a Nernst coefficient gives an expression for the PNE as a function of $\sin 2\theta$,

$$\vec{E_y} = \frac{1}{2} P_N \frac{dT}{dx} M^2 \sin 2\theta \hat{y}. \tag{7.4.14}$$

See Popovic (75) for a more detailed derivation of the Hall effect expression.

7.5 Conclusion

We have presented measurements of α(T), α(H) and R(H) of 20 nm thick Ni and Ni-Fe films. The temperature dependence of α for both materials was similar to previously published results for thin films measured using the same technique on an earlier version of the supporting platform. However, the 20 nm films displayed a lower resistance than previous films, resulting in α(T) values closer to bulk values. Ni and Ni-Fe films exhibited even magnetic field dependence for α(H) and R(H). We observed a coercivity of $\approx$ 30 Oe for Ni and $\approx$ 5 Oe for Ni-Fe. Both Ni-Fe and Ni exhibit a linear proportionality between α and 1/R predicted by the Mott equation. Thus, for a given temperature, α is a function of ρ and the $(\partial\rho/\partial E)_{E=E_F}$ term is constant. Finally, we used $\alpha(\mathrm{H}_{\|})$ and $\alpha(H_{\perp})$ to predict previous PNE results of films grown during the same deposition. From the even field dependence of both α(H) and R(H), the linear relationship between α and 1/R, and the prediction of PNE results using $\alpha(\mathrm{H}_{\|})$ and $\alpha(H_{\perp})$, we conclude all three share a common physical origin of spin-dependent scattering.

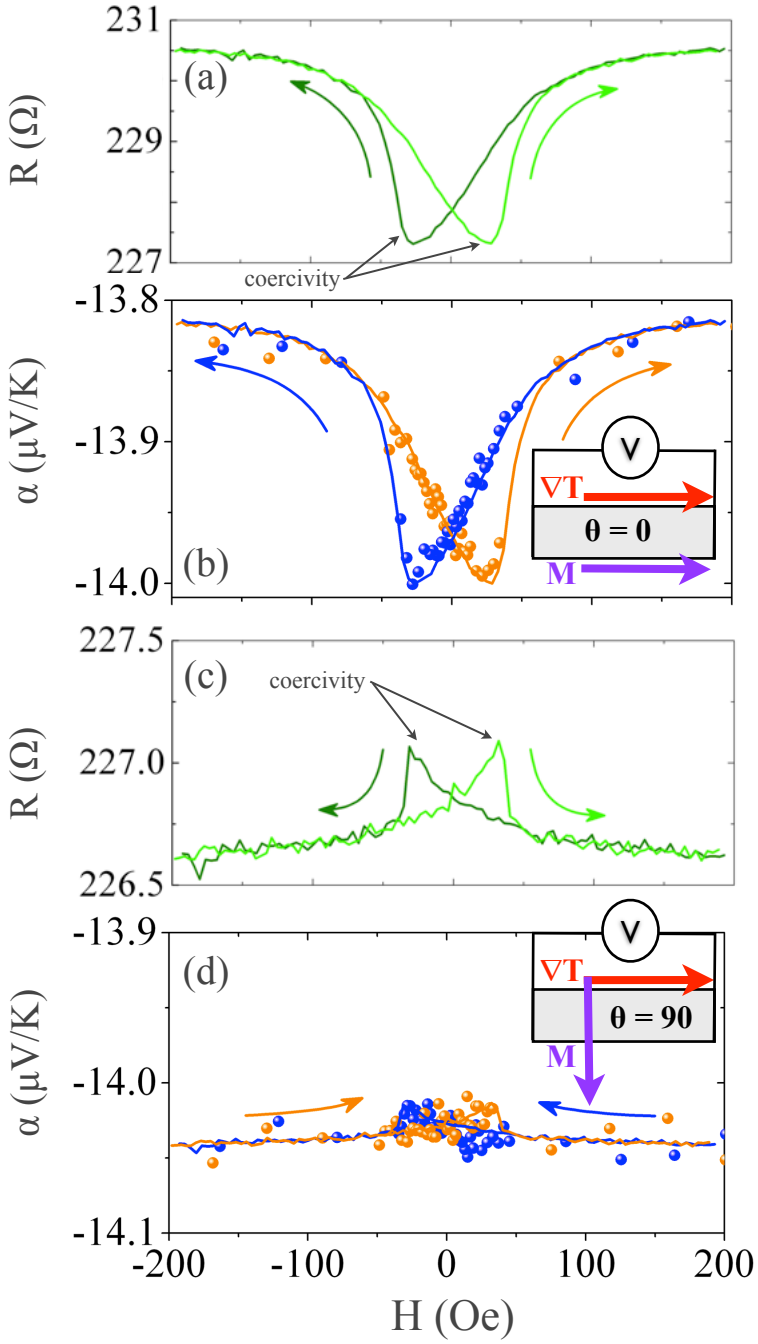

Figure 7.4: Magnetic field dependence of R and α for a 20 nm thick Ni film. (a) $R(H_{\parallel})$, (b) $\alpha(H_{\parallel})$, (c) $R(H_{\perp})$, and (d) $\alpha(H_{\perp})$. Solid lines in (b) and (d) represent $\alpha(H)$ values predicted using linear fits to the α vs 1/R plot for Ni. All measurements are made at a base temperature of 276K.

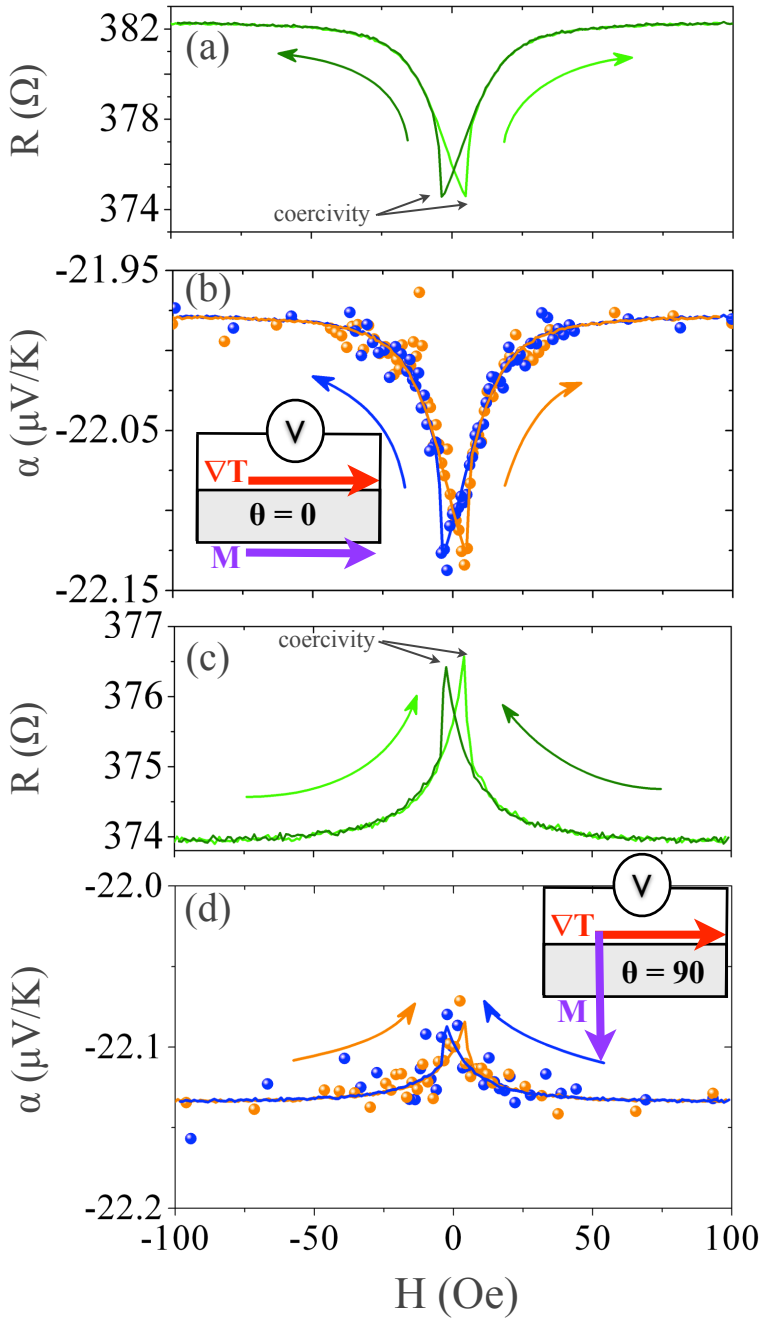

Figure 7.5: Magnetic field dependence of R and α for a 20 nm thick Ni-Fe film. (a) $R(H_{\parallel})$, (b) $\alpha(H_{\parallel})$, (c) $R(H_{\perp})$, and (d) $\alpha(H_{\perp})$. Solid lines in (b) and (d) represent $\alpha(H)$ values predicted using linear fits to the α vs 1/R plot for Ni-Fe. All measurements are made at a base temperature of 276K.

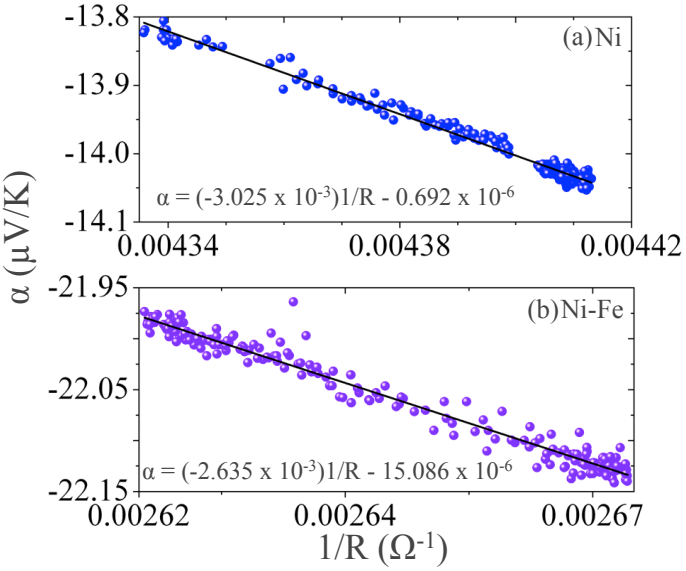

Figure 7.6: Inverse R dependence of α for (a) Ni and (b) Ni-fe films measured in $H_{\parallel}$ and $H_{\perp}$. Solid lines represent linear fits to the data.

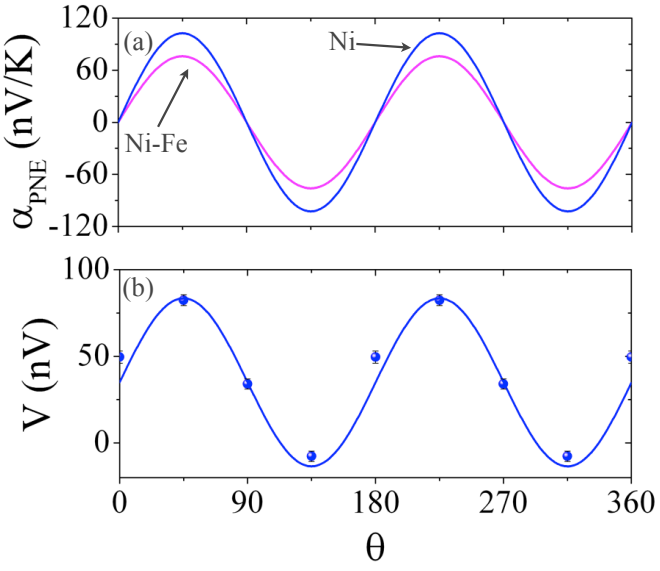

Figure 7.7: (a) Angular dependence of the calculated PNE coefficients (α_{PNE}) for Ni-Fe and Ni generated using Eq. 7.1.4. (b) Angular dependence of the expected voltage from Ni (solid line) compared with the voltage generated by the PNE from Avery et al. citeAveryPRL12 for a 20 nm Ni film deposited iat the same time as the Ni sample from this experiment.

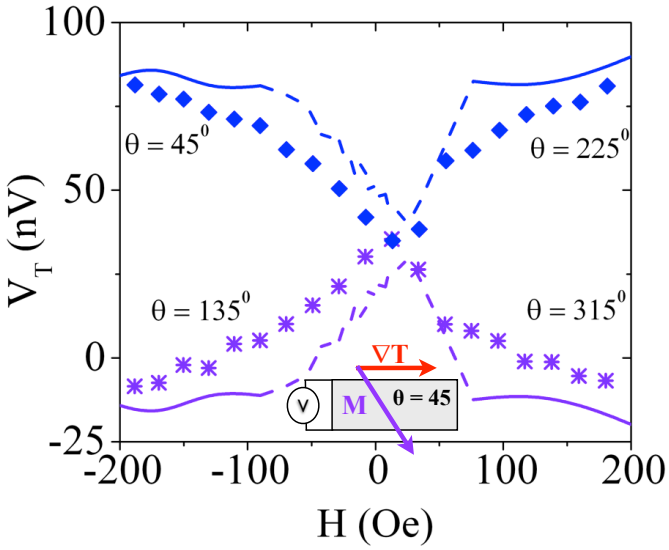

Figure 7.8: Magnetic field dependence of the V_T generated by the transverse thermopower (or planar Nernst effect) for a 20 nm thick Ni film citeAveryPRBRC11 at θ = 45°, 135°, 225°, 315°. The solid lines represent the voltage predicted using $\alpha(H_{\parallel})$ and $\alpha(H_{\perp})$ where the film is saturated. Dotted lines represent the prediction where $\vec{M}$ is not well-defined.

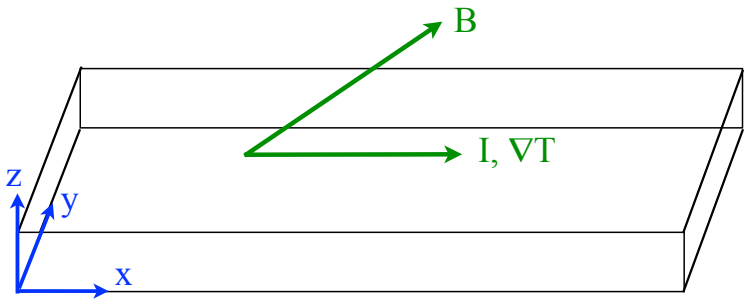

Figure 7.9: Schematic showing the magnetic induction $\vec{B}$ and the current or thermal gradient direction of the Hall effect or the Nernst effect respectively.

Chapter 8

Peltier effect

8.1 Introduction to the Peltier Effect

The Peltier effect and the Seebeck effect are the two most fundamental thermoelectric phenomena. These thermoelectric effects are a primary focus in the emerging field of spin caloritronics where an intense search is underway for their spin analogs (14, 57, 45, 76, 77). Both effects couple heat and electrical currents together and are theorized to be reciprocals of each other. In the Seebeck effect, a material develops a current or voltage in response to a thermal gradient. Conversely, the temperature difference developed across a material in response to an applied current is known as the Peltier effect. The importance of both effects stems from their role in a variety of applications from thermoelectric energy generation (78) to technological applications such as spot cooling of integrated circuits (79, 80).

In 1931, Lars Onsager developed a proof of the reciprocity between the Peltier and Seebeck coefficients for which he later won the 1968 Nobel Prize in Chemistry (81). Onsager reciprocity is the result of the thermodynamics of non-equilibrium

processes, assuming microscopic reversibility applied to fluctuations, and relates generalized thermodynamic forces with generalized currents. The general mathematical expression linking forces and currents is, $\dot{q} = \Sigma_{j=1}^{N} L_{ij} X_j$ where $\dot{q}$ is a generalized current, X_J is a generalized force, and L_{ij} is the coefficient relating the two. The Onsager reciprocity applies to the off-diagonal elements in the L_{ij} matrix such that

$$L_{ij} = L_{ji}. \tag{8.1.1}$$

Applying these conditions to the charge and heat flow through a material yields a system of equations

$$\begin{pmatrix} \vec{J} \\ \dot{\vec{Q}} \end{pmatrix} = \sigma \begin{pmatrix} 1 & \alpha \\ \Pi & k/\sigma \end{pmatrix} \begin{pmatrix} \nabla V \\ -\nabla T \end{pmatrix} \tag{8.1.2}$$

where $\dot{\vec{Q}}$ is the heat current density, $\vec{J}$ is the electrical current density, σ is the electrical conductivity, and k is the thermal conductivity (25, 22). The off-diagonal coefficient elements are the Seebeck coefficient (α) and the Peltier coefficient (Π) and are related through their predicted Onsager reciprocity (22)

$$\Pi = \alpha T. \tag{8.1.3}$$

The dominant transporter of heat in metals is electrons. In the Seebeck effect, heating one side of a film excites phonons and electrons that transport energy through the film. Hot electrons transport heat by flowing down the thermal gradient to occupy available energy states on the cold end of a film. Cold electrons move in the opposite direction in response to the electric field established by the hot elec-

trons. The charge is redistributed until a steady state balance is reached between the heat flow through the film and the electric field generated by the intinerant energetic electrons. This sets up a measurable voltage in response to a temperature difference maintained across a sample. In magnetic thin films, additional excitations in the form of spin waves, or magnons, can increase the voltage drop by transporting additional energy from the phonons to the electrons. The increase in thermopower magnitude through magnons is known as magnon drag and is the magnetic analog of phonon drag usually observed at low temperatures in metallic films such as copper (82). We have previously observed magnon drag in Fe films (63). Experiments probing the Peltier effect and the Onsager reciprocal relations in samples that exhibit magnon drag offer additional insight into which couplings between excitations are microscopically time reversible.

Compared to the substantial number of Seebeck effect experiments, however, few experiments have explored the Peltier effect. There are several reasons for this considerable disparity. For one, measurements of α are straightforward and do not require the sensitivity thermal measurements necessary to measure Π. Furthermore, the same current that generates a temperature difference through the Peltier effect also gives rise to Joule heating. The heat produced through the Joule effect is proportional to I^2 and can obscure the Peltier heating or cooling, which is proportional to I. Finally, sensitive thermal transport measurements present challenges in scaled down geometries such as thin films (63, 33, 64, 67).

Rather than directly observing the Peltier effect, Π is usually estimated by assuming Onsager reciprocity. Therefore, there are only a few direct measurements of the Peltier coefficient. One experiment by Grannemann et al. explored the magnon drag component in Ni-Cu and Ni-Fe alloys below 4.2 K, observing a reduction in

Π after quenching magnons using a large applied external magnetic field (83). The few additional studies have probed the Peltier effect in various materials including semiconductors (84, 85, 86), in a metallic thermopile (87), and in GMR multilayers with the current-perpendicular-to-plane (88). However, there are no previous experiments exploring the Peltier effect in Ni, Ni-Fe, and Fe films from 77 to 325 K.

In this chapter, we present results from experiments designed to measure the Peltier effect. Comparing the results from the Peltier measurements and predictions of the Peltier coefficient using previously measured Seebeck coefficient allows us to test the Onsager reciprocal relation between the Peltier coefficient and Seebeck coefficients directly as well as probe the coupling between thermal excitations in ferromagnetic thin films such as electrons, phonons, and magnons. We first describe the suspended Si-N thermal isolation platforms which enable sensitive thermal and electrical transport measurements. Next we present our methodology for measuring Π. One of the major advantages of our technique is the flexibility to apply either a charge current or heat current through a thin film and monitor the resulting temperature or potential difference generated as a consequence of the Seebeck and Peltier effects on the same film. Finally, we present results for 20 nm thick Ni, permalloy (Ni-Fe), and Fe thin films measured from 77 to 325 K and discuss the validity of the Onsager reciprocity between Π and α.

8.2 Methodology

We measured the Peltier effect on 20 nm thick Ni and Ni-Fe films supported by suspended low-stress Si-N membranes. These thermal isolation platforms orig-

inated from the same wafer as the platforms previously used to measure the planar Nernst effect, magnetic field dependent thermopower, and anisotropic magnetoresistance (67, 64). We deposited the Ni and Ni-Fe experimental films during platform fabrication using RF sputtering. Each thermal isolation platform has 2 islands patterned with a thermometer and heater, and a bridge. The bridge supports a film and provides the only thermal path between the two islands. Adding a film provides a parallel path for heat through the film in addition to the bridge. Eight legs connect the platform to the frame and suspend the platform to eliminate contact to the large thermal mass of the Si frame. Fig. 8.1 (b) is an SEM micrograph showing an exam-

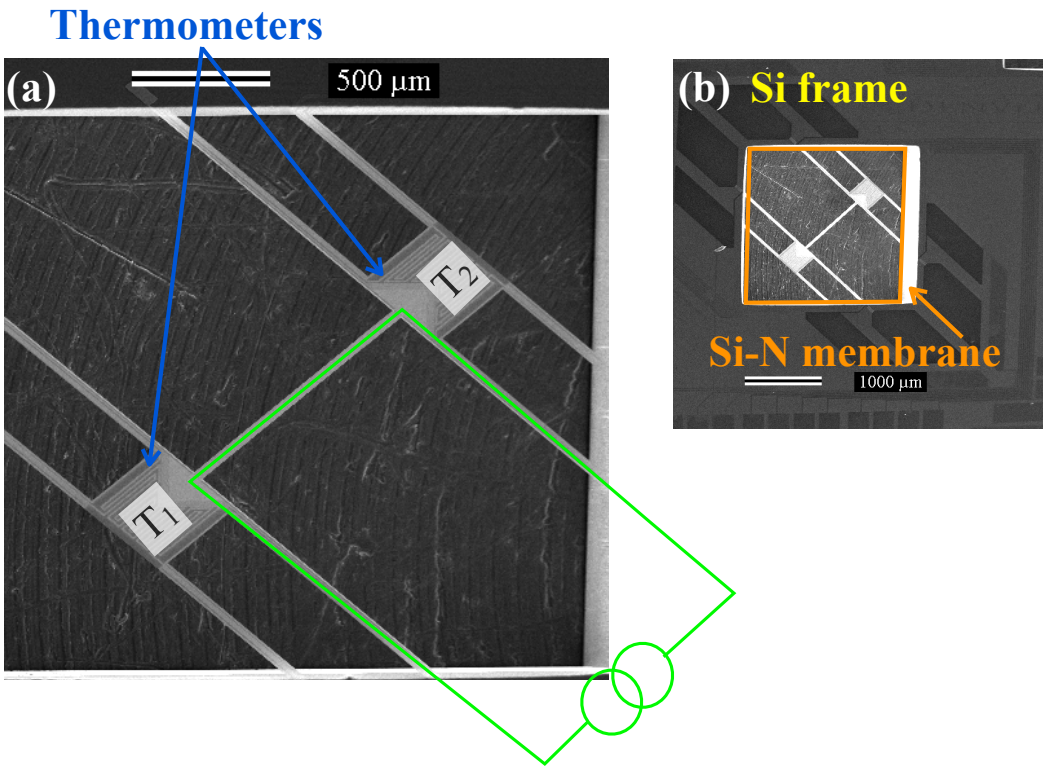

Figure 8.1: An example thermal isolation platform used to measure the Peltier effect. (a) shows the thermometers on either side of the film and current path through the film. (b) shows a zoomed out SEM micrograph of the Si-N platform and the surrounding Si frame.

ple thermal isolation platform and the surrounding Si frame. Fig. 8.1 (a) is a close up of the platform that highlights the thermometry and illustrates the current path through the film. There is an additional thermometer on the Si frame for monitoring the bath temperature throughout the experiment. We presented platform fabrication detailed steps in a previous publication (64).

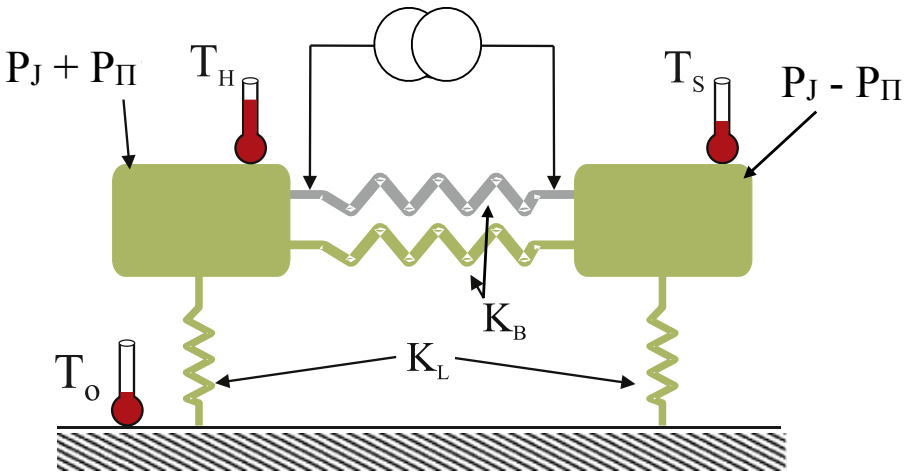

Figure 8.2: A schematic showing the simple thermal model for the heat flow due to the Peltier and Joule effects through the micromachined thermal platforms. Thermal conduction occurs through the legs connecting the Si-N platform to the Si frame, K_L, and through the Si-N bridge and film connecting the two Si-N islands, K_B. A current through the film generates heat from the Joule effect and the Peltier effect, P_J and P_{Π}.

To develop expressions for the Joule power (P_{J}) and the Peltier power (P_{Π}) dissipated in the film, we start with a system of steady-state heat flow equations for

the thermal model illustrated in Fig. 8.2

$$P_J + P_{\Pi} = K_L(T_h - T_o) + K_B(T_h - T_s)$$

$$P_J - P_{\Pi} = K_L(T_s - T_o) + K_B(T_s - T_h).$$

In these equations, T_h, T_s, and T_o are the temperatures on the hot and cold ends of the film and the Si frame, and K_L and K_B represent the thermal conductance for the legs and the bridge and film together. Solving for $P_{\rm J}$ and P_{Π} gives

$$P_J = \frac{1}{2}K_L[(T_h - T_o) + (T_s - T_o)] \tag{8.2.1}$$

$$P_{\Pi} = (K_B + \frac{1}{2}K_L)(T_h - T_s) \tag{8.2.2}$$

According to Eqn. 8.2.1, the power dissipated by the Joule effect is a function of the thermal conductance through the legs and the temperature difference generated along the legs. The power dissipated through the Peltier effect depends on the entire thermal conductance through the platform and the temperature difference generated across the film.

We begin a Peltier experiment by calibrating each of the three experimental thermometers. At each reference temperature, we regulate the temperature of the bath and measure all three resistances with no external applied current. We perform a separate thermometer calibration for each thermometer on each thermal isolation platform during every experiment. In this way, we ensure the most accurate determination of T_o, T_h, and T_s using their respective $T(R)$ functions. To measure the Peltier effect, we apply a series of currents from negative to positive and record the resulting temperatures on each side of the film. Next, we convert to P_{Π} by substi-

tuting measured values for K_B, K_L, T_h, T_s, and T_o into Eqn. 8.2.2. To determine the Peltier coefficient, we perform a linear fit to the Peltier power, P_{Π}, as a function of applied current. The slope of the linear fit to the data represents the Peltier coefficient Π. We also monitor the frame thermometer for temperature stability at each base temperature. Finally, we measure the voltage generated as a consequence of the current through the film and determine the film resistance using a linear fit to a voltage versus current plot.

8.3 Results and Discussion for the Peltier Effect

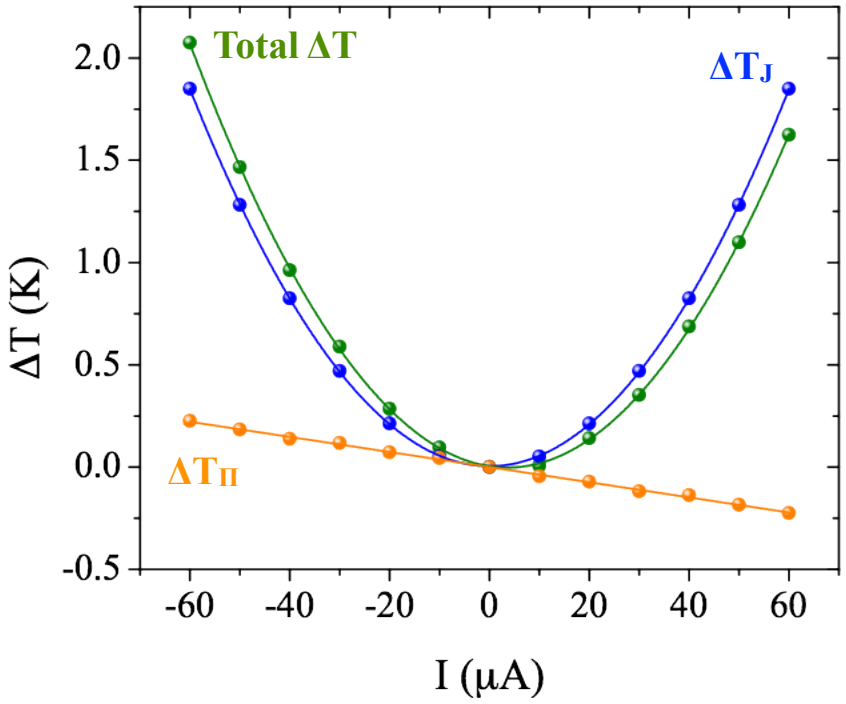

Figure 8.3: Temperature difference as a function of current for one end of a 20 nm thick Ni film. Total $\triangle$T is in green, $\triangle T_J$ is in blue, and $\triangle T_{\Pi}$ is orange.

The total temperature difference at the hot end of the film, $\triangle T_{hot} = \triangle T_J +$

$\triangle T_{\Pi}$, is a sum of $\triangle$T from the Joule effect and the Peltier effect. Reversing the current causes the Peltier effect to switch from liberating heat to absorbing heat. However, the Joule effect still adds heat, and the temperature difference becomes $\triangle T_{cold} = \triangle T_J - \triangle T_{\Pi}$. We take advantage of the symmetry of the Joule effect to determine its contribution to the total $\triangle$T. Thus, adding $\triangle T_{cold}$ and $\triangle T_{hot}$ at either end of a film gives $2\triangle T_J$. Subtracting the $\triangle T_J$ contribution from $\triangle T_{hot}$ gives $+\triangle T_{\Pi}$ and from $\triangle T_{cold}$ gives $-\triangle T_{\Pi}$.

Fig. 8.3 shows the temperature difference generated on one side of the film by running a current through a Ni film. The $\triangle T_{\Pi}$, in orange, decreases as the current is changed from -60 μA to +60 μA in 20 μA increments. The change in $\triangle T_{\Pi}$ is linear, symmetric about I=0, and the Peltier effect can be clearly seen when comparing two polarities of the same current. For example, at I = +60 the temperature difference generated by the Peltier effect is 0.25 K. Reversing the current to -60 μA causes the Peltier effect to be reversed and the temperature difference becomes -0.25 K. The Joule effect, which is always a heating effect, is proportional to I^2, and therefore $\triangle T_J$ is expected to be as well. $\triangle T_J$ data (shown in blue) is always positive indicating heating for either polarity of applied current. The quadratic dependence of the Joule heat on I is evident from the $\triangle T_J$ data. Finally, the total $\triangle$T function (in green) is similar to the Joule effect, but asymmetric around x=0. The observed asymmetry, for this end of the film, originates from the contribution of a $-\triangle T_{\Pi}$ as a result of $-I$ and a $+\triangle T_{\Pi}$ from a $+I$. The opposite end of the film (not represented in Fig. 8.3) exhibits an opposite Peltier response for a given current as expected.

To determine the power dissipated by the Joule effect and the Peltier effect resulting in the observed $\triangle T_J$ and $\triangle T_{\Pi}$, we substitute the experimentally determined

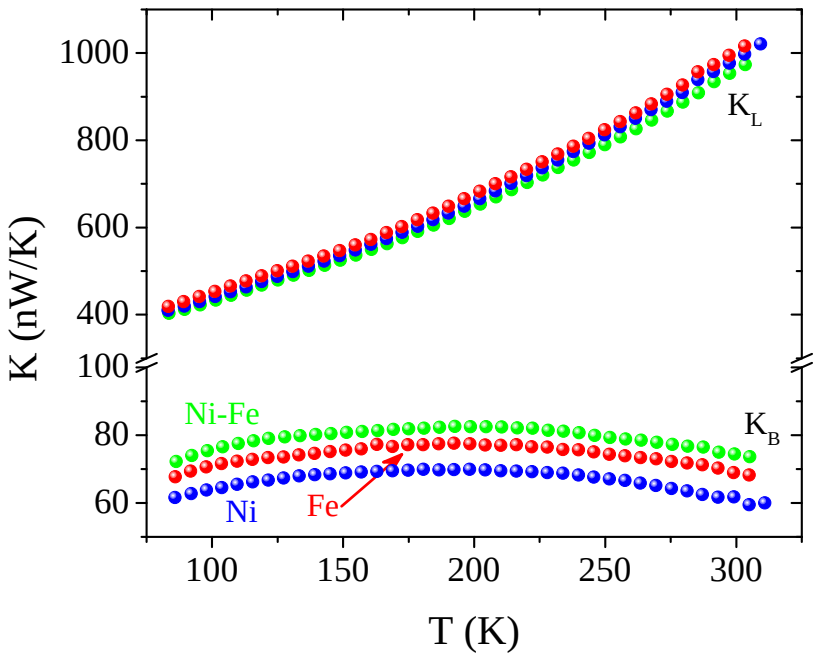

Figure 8.4: Thermal conductance as a function of temperature for a 20 nm Ni film, a 20 nm Ni-Fe film, and a 20 nm Fe film supported by Si-N membrane platforms from the same wafer. K_L represents the thermal conductance for the suspension legs connected to the Si frame and K_B represents the thermal conductance through the film and the supporting Si-N bridge connecting the islands.

T_h, T_s, and T_o from this experiment and K_L and K_B values determined in earlier measurements of films from the same wafer into Eqns. 8.2.1 and 8.2.2. Fig. 8.4 shows thermal conductance as a function of temperature for 20 nm thick Ni, Fe, and Ni-Fe films supported by Si-N membrane structures. K_L represents the conductance through the suspension legs connecting the thermal isolation platform to the Si frame and the metallic wires running along them. K_B is the total thermal conductance contributed by the Si-N bridge plus a 20 nm thick film deposited on the bridge. The temperature dependence and magnitude of the thermal conductance

displayed in Fig. 8.4 are comparable to previous measurements of K conducted on similar films as expected.

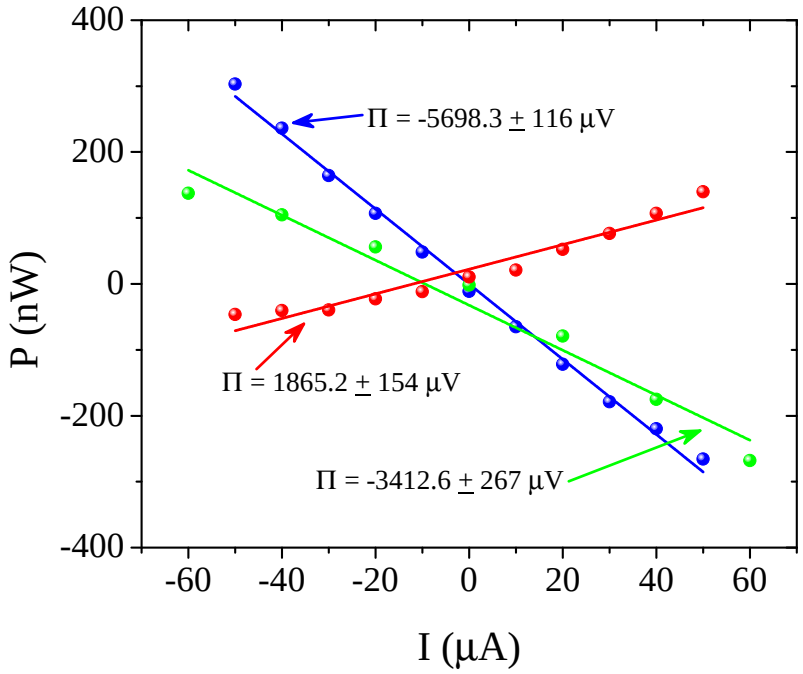

Figure 8.5: Power generated by the Peltier effect as a function of current for a 20 nm Ni film (green), a 20 nm Ni-Fe film (blue), and a 20 nm Fe film (red) at 276 K. The slope of the linear fit to the data gives the Peltier coefficient, Π.

Fig. 8.5 shows P_{Π} versus current for the 20 nm Ni, Fe, and Ni-Fe films in green, red, and blue respectively measured at a base temperature of 276 K. The slope of the linear fit to P_{Π} as a function of the applied current gives the Peltier coefficient, Π. The similarities between Ni and Ni-Fe as well as the differences between the responses of these films and the Fe film to an applied series of currents are immediately apparent. The film with the largest P_{Π} magnitude is the Ni-Fe film. The second largest was the Ni film while the Fe film displayed the smallest magnitude. Linear fits to the data revealed a negative slope for Ni and Ni-Fe and a

positive slope for Fe as expected from the sign of the $\Pi = \alpha T$ prediction.

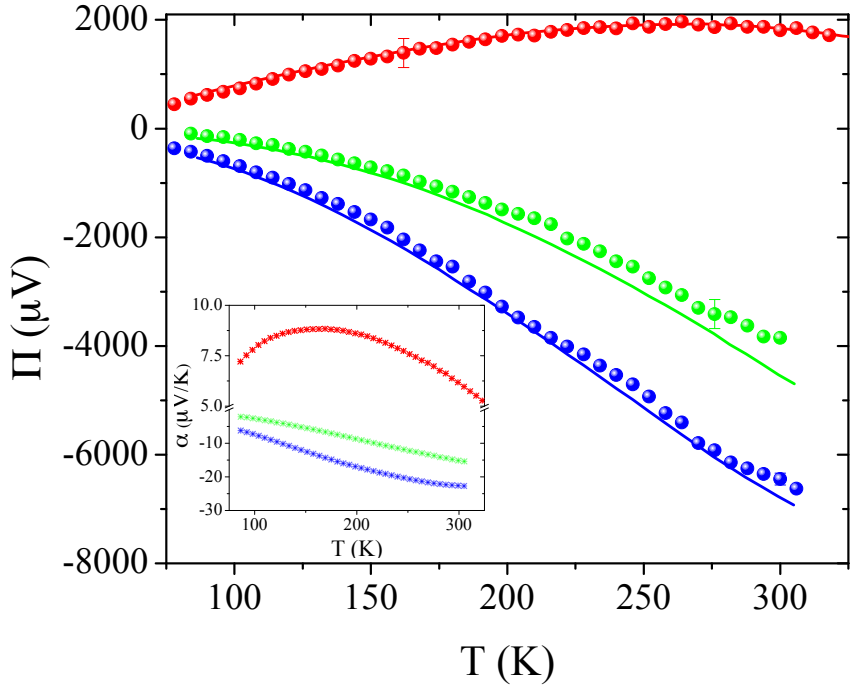

Figure 8.6: Π as a function of temperature for a 20 nm Ni film (green), a 20 nm Ni-Fe film (blue), and a 20 nm Fe film (red). Inset plot displays previously measured α for similar films. Predicted Π values from $\Pi = \alpha T$ are represented by solid lines.

Fig. 8.6 shows Π as a function of temperature for Ni, Ni-Fe, and Fe. The predicted Π values calculated from previous measurements of α on similar films are represented by solid lines. The inset in Fig. 8.6 shows α versus temperature used in these predictions. Π for all three films is in excellent agreement with predicted values. The additional thermopower indicated by the peak in Fe α originates from magnon drag. This peak is represented in both the predicted and experimental Π temperature dependence as well. This confirms that Onsager reciprocity applies not only to the electrons and phonons, but the exchange between these excitations and magnons as well. These results are consistent with the previous observation

of reduced Π when magnons are quenched using a large applied external magnetic field in Ni-Cu and Ni-Fe alloys at temperatures below 4.2 K.

8.4 Conclusion

In summary we have conducted experiments to measure the Peltier coefficient in Ni, Ni-Fe, and Fe thin films. Ni and Ni-Fe films displayed a negative $\Pi(T)$ while the Fe film $\Pi(T)$ was positive as expected from previously measured $\alpha(T)$ values. In contrast to the Ni and Ni-Fe films, the Fe film exhibited a peak associated with the Peltier effect magnon drag. The Peltier coefficients measured for all three films was in excellent agreement with the Peltier coefficient predicted using the Onsager reciprocal relation $\Pi = \alpha T$. The close agreement between measured and predicted Π values confirms the microscopic time reversibility between the Peltier and Seebeck effects. Finally, the observation of magnon drag in the Fe film confirms the microscopic time reversal symmetry of magnon drag. This verifies that the coupling constant between the phonon, magnon, and electron systems in the film is equal and reversible.

Chapter 9

Conclusion

I have presented a group of experiments designed to probe thermal and electrical transport in ferromagnetic thin films using a suspended membrane technique. The first experiments established the efficacy of our technique applied to ferromagnetic and non-magnetic metallic thin films. I also presented thermopower and resistivity results from several ferromagnetic thin films. These results confirmed the Mott relationship between electrical resistivity and thermopower and represent some of the most sensitive thermopower measurements conducted to date for thin films. These measurements are sensitive enough to detect magnon drag in Fe and detect changes in thermopower as a function of magnetic field as small as 50 nV/K. I presented results from the first measurements of the Peltier effect in ferromagnetic thin films from 77 to 325 K. These results confirm the relationship between the Seebeck and Peltier effects, $\Pi = \alpha T$, predicted by the theory of Onsager reciprocity.

The most significant results from this thesis are results that prove the planar Nernst effect rather than the spin Seebeck effect is responsible for the observed transverse voltage in response to an applied thermal gradient using a planar exper-

imental geometry. We observed no evidence of a thermally generated spin current in our 2-D experimental geometry. The even field dependence of the planar Nernst effect originates from spin-dependent scattering, and this scattering is also responsible for the magnetic field dependence of thermopower and magnetoresistance in the same films. In future experiments designed to measure transverse voltage associated with a "spin" Seebeck effect, any films that exhibit anisotropic magnetoresistance will generate a transverse voltage from the planar Nernst effect. If a spin current is present, these Nernst effect voltages will can mimic or completely overwhelm the spin current signal. These results underline the importance of thermal gradient control and definition in experiments designed to probe thermal and electrical transport in ferromagnetic thin films.

Bibliography

[1] Th. J. Seebeck. *Magnetische Polarisation der Metalle und Erze Durch Temperatur-Differenz "1822-1823"*. A. J. v. Oettingen, 1895.

[2] Choongho Yu, Li Shi, Zhen Yao, Deyu Li, and Arunava Majumdar. Thermal conductance and thermopower of an individual single-wall carbon nanotube. *Nano Letters*, 5(9):1842–1846, 2005.

[3] Albert Fert. The present and the future of spintronics. *Thin Solid Films*, 517(1):2 – 5, 2008.

[4] G. Binasch, P. Grünberg, F. Saurenbach, and W. Zinn. Enhanced magnetoresistance in layered magnetic structures with antiferromagnetic interlayer exchange. *Phys. Rev. B*, 39:4828–4830, 1989.

[5] J. Barnaś, A. Fuss, R. E. Camley, P. Grünberg, and W. Zinn. Novel magnetoresistance effect in layered magnetic structures: Theory and experiment. *Phys. Rev. B*, 42:8110–8120, 1990.

[6] M. N. Baibich, J. M. Broto, A. Fert, F. Nguyen Van Dau, F. Petroff, P. Etienne, G. Creuzet, A. Friederich, and J. Chazelas. Giant magnetoresistance of (001)fe/(001)cr magnetic superlattices. *Phys. Rev. Lett.*, 61:2472–2475, 1988.

[7] J. S. Moodera, Lisa R. Kinder, Terrilyn M. Wong, and R. Meservey. Large magnetoresistance at room temperature in ferromagnetic thin film tunnel junctions. *Phys. Rev. Lett.*, 74:3273–3276, 1995.

[8] Terunobu Miyazaki and Nobuki Tezuka. Spin polarized tunneling in ferromagnet/insulator/ferromagnet junctions. *Journal of Magnetism and Magnetic Materials*, 151(3):403 – 410, 1995.

[9] S.S.P. Parkin, M. Hayashi, and L. Thomas. Magnetic domain-wall racetrack memory. *Science*, 320(5873):190, 2008.

[10] Masamitsu Hayashi, Luc Thomas, Rai Moriya, Charles Rettner, and Stuart S. P. Parkin. Current-controlled magnetic domain-wall nanowire shift register. *Science*, 320(5873):209–211, 2008.

[11] SD Bader and SSP Parkin. Spintronics. *Annu. Rev. Condens. Matter Phys.*, 1(1):71–88, 2010.

[12] Haiming Yu, S. Granville, D. P. Yu, and J.-Ph. Ansermet. Evidence for thermal spin-transfer torque. *Phys. Rev. Lett.*, 104:146601, 2010.

[13] D. Hinzke and U. Nowak. Domain wall motion by the magnonic spin seebeck effect. *Phys. Rev. Lett.*, 107:027205, 2011.

[14] K. Uchida, S. Takahashi, K. Harii, J. Ieda, W. Koshibae, K. Ando, S. Maekawa, and E. Saitoh. Observation of the spin Seebeck effect. *Nature*, 455(7214):778–781, 2008.

[15] K. Uchida, H. Adachi, T. Ota, H. Nakayama, S. Maekawa, and E. Saitoh. Ob-

servation of longitudinal spin-seebeck effect in magnetic insulators. *Applied Physics Letters*, 97(17):172505–172505, 2010.

[16] K. Uchida, T. Nonaka, T. Ota, and E. Saitoh. Longitudinal spin-seebeck effect in sintered polycrystalline (mn,zn)fe[sub 2]o[sub 4]. *Applied Physics Letters*, 97(26):262504, 2010.

[17] H. Adachi, K. Uchida, E. Saitoh, J. Ohe, T. Takahashi, and S. Maekawa. Gigantic enhancement of spin seebeck effect by phonon drag. *Applied Physics Letters*, 97(25):252506, 2010.

[18] C. M. Jaworski, J. Yang, S. Mack, D. D. Awschalom, R. C. Myers, and J. P. Heremans. Spin-seebeck effect: A phonon driven spin distribution. *Phys. Rev. Lett.*, 106:186601, 2011.

[19] C.M. Jaworski, R.C. Myers, E. Johnston-Halperin, and J.P. Heremans. Giant spin seebeck effect in a non-magnetic material. *Nature*, 487:210–213, 2012.

[20] G. E.W. Bauer, A. H. MacDonald, and S. Maekawa. Spin caloritronics. *Solid State Communications*, 150(1112):459 – 460, 2010.

[21] G.S. Kumar, G. Prasad, and R.O. Pohl. Experimental determinations of the lorenz number. *Journal of Materials Science*, 28:4261–4272, 1993.

[22] J. M. Ziman. *Electrons and Phonons*. Oxford University, London, 1960.

[23] N. Hawkins and staff. *Hawkins Electrical Guide Number One: Questions, Answers, & Illustrations, A Progressive Course of Study for Engineers, Electricians, Students, and Those Desiring to acquire a Working Knowledge of Electricity and its Applications*. Theo. Audel & Co., 1917.

[24] D.M. Rowe, editor. *Thermoelectrics Handbook: Micro to Nano*. CRC Press, 2005.

[25] S. Maekawa, S.O. Velnzuela, E. Saitoh, and T. Kimura, editors. *Spin Current*. Oxford University Press, 2012.

[26] J.E. Hirsch. Spin hall effect. *Physical Review Letters*, 83(9):1834–1837, 1999.

[27] T.M. Tritt, editor. *Thermal Conductivity: Theory, Properties, and Applications*. Kluwer Academic / Plenum Publishers, 2004.

[28] David G. Cahill. Thermal conductivity measurement from 30 to 750 k: the 3 omega method. *Review of Scientific Instruments*, 61(2):802–808, 1990.

[29] D.G. Cahill, W.K. Ford, K.E. Goodson, G.D. Mahan, A. Majumdar, H.J. Maris, R. Merlin, and S.R. Phillpot. Nanoscale thermal transport. *Journal of Applied Physics*, 93(2):793–818, 2003.

[30] A.I. Hochbaum, R. Chen, R.D. Delgado, W. Liang, E.C. Garnett, M. Najarian, A. Majumdar, and P. Yang. Enhanced thermoelectric performance of rough silicon nanowires. *Nature*, 451:163–167, 2008.

[31] A.I. Boukai, Y. Bunimovich, J. Tahir-Kheli, J. Yu, W.A. Goddard III, and J.R. Heath. Silicon nanowires as efficient thermoelectric materials. *Nature*, 451:168–171, 2008.

[32] Rubina Sultan, A.D. Avery., G. Stiehl, and B.L. Zink. Thermal conductivity of micromachined low-stress silicon-nitride beams from 77 to 325 k. *Journal of Applied Physics*, 105(4), Feb 15 2009.

[33] B.L. Zink, A.D. Avery, Rubina Sultan, D. Bassett, and M.R. Pufall. Exploring thermoelectric effects and wiedemann-franz violation in magnetic nanostructures via micromachined thermal platforms. *Solid State Communications*, 150(11-12):514–518, 2010.

[34] Childs G.E., Ericks L.J., and Powell R.L. Thermal conductivity of solids at room temperature and below - review and compilation of literature. *NBS Monograph*, M131:1–608, 1973.

[35] Laubitz M.J. and Matsumura T. Transport properties of ferromagnetic metals .1. cobalt. *Canadian Journal Of Physics*, 51(12):1247–1256, 1973.

[36] Powell R.L. and Blaniped W.A. Thermal conductivity of metals and alloys at low temperatures. *NBS Circular*, 556, 1954.

[37] Moore J.P., Kollie T.G., Graves R.S., and McElroy D.L. Thermal Trasport Properties of Ordered and Disordered Ni3Fe. *Journal Of Applied Physics*, 42(8):3114–&, 1971.

[38] T Farrell and D Greig. The thermal conductivity of nickel and its alloys. *Journal of Physics C: Solid State Physics*, 2(8):1465, 1969.

[39] M. N. Ou, T. J. Yang, S. R. Harutyunyan, Y. Y. Chen, C. D. Chen, and S. J. Lai. Electrical and thermal transport in single nickel nanowire. *Applied Physics Letters*, 92(6):063101, 2008.

[40] G. K. White and R. J. Tainsh. Electron scattering in nickel at low temperatures. *Phys. Rev. Lett.*, 19:165–166, 1967.

[41] W. Holmes, J. M. Gildemeister, P. L. Richards, and V. Kotsubo. Measurements of thermal transport in low stress silicon nitride films. *Applied Physics Letters*, 72(18):2250–2252, 1998.

[42] M. Johnson and R.H. Silsbee. Thermodynamic analysis of interfacial transport and of the thermomagnetoelectric system. *Physical Review B*, 35(10):4959–4972, 1987.

[43] M. Hatami, G.E.W. Bauer, Q. Zhang, and P.J. Kelly. Thermoelectric effects in magnetic nanostructures. *Phys. Rev. B*, 79(17):174426, May 2009.

[44] L. Gravier, A. Fábián, A. Rudolf, A. Cachin, J. E. Wegrowe, and J. Ph. Ansermet. Spin-dependent thermopower in co/cu multilayer nanowires. *Journal of Magnetism and Magnetic Materials*, 271(2-3):153 – 158, 2004.

[45] C.M. Jaworski, J. Yang, S. Mack, D.D. Awschalom, J.P. Heremans, and R.C. Myers. Observation of the spin-seebeck effect in a ferromagnetic semiconductor. *Nature Materials*, 9(11):898–903, 2010.

[46] J. Xiao, G.E.W. Bauer, K. Uchida, E. Saitoh, and S. Maekawa. Theory of magnon-driven spin seebeck effect. *Physical Review B*, 81(21):214418, 2010.

[47] J.M. Ziman. *Electrons and Phonons*. Oxford University Press, 1960.

[48] F.J. Blatt, D.J. Flood, V. Rowe, P.A. Schroeder, and J.E. Cox. Magnon-drag thermopower in iron. *Physical Review Letters*, 18(11):395–396, Mar 1967.

[49] C.Y. Ho, T.C. Chi, R.H. Bogaard, T.N. Havill, and H.M. James. Thermoelectric power of selected binary alloy systems. In J.G. Hust, editor, *Thermal*

Conductivity 17, volume 17, pages 195–205. Thermophysical Properties Division National Bureau of Standards, Plenum Press, 1983.

[50] M.J. Laubitz and T. Matsumura. Transport properties of the ferromagnetic metals. i. cobalt. *Canadian Journal of Physics*, 51(12):1247–1256, 1973.

[51] D.K.C. MacDonald and W.B. Pearson. Thermoelectricity in metals at normal temperatures - a query. *Proceedings of the Physical Society*, 78(2):306, 1961.

[52] D.D. Awschalom and M.E. Flatté. Challenges for semiconductor spintronics. *Nature Physics*, 3(3):153–159, 2007.

[53] SA Wolf, DD Awschalom, RA Buhrman, JM Daughton, S. Von Molnar, ML Roukes, AY Chtchelkanova, and DM Treger. Spintronics: A spin-based electronics vision for the future. *Science*, 294(5546):1488–1495, 2001.

[54] I. Žutić, J. Fabian, and S.D. Sarma. Spintronics: Fundamentals and applications. *Reviews of Modern Physics*, 76(2):323, 2004.

[55] J. Sinova. Spin seebeck effect: Thinks globally but acts locally. *Nature Materials*, 9(11):880–881, 2010.

[56] G. E.W. Bauer, E. Saitoh, and B.J. van Wees. Spin caloritronics. *Nature Materials*, 11:391–399, 2012.

[57] K. Uchida, J. Xiao, H. Adachi, J. Ohe, S. Takahashi, J. Ieda, T. Ota, Y. Kajiwara, H. Umezawa, H. Kawai, G.E.W. Bauer, S. Maekawa, and E. Saitoh. Spin seebeck insulator. *Nature Materials*, 9:894–897, November 2010.

[58] O. Mosendz, J. E. Pearson, F. Y. Fradin, G. E. W. Bauer, S. D. Bader, and A. Hoffmann. Quantifying spin hall angles from spin pumping: Experiments and theory. *Phys. Rev. Lett.*, 104:046601, 2010.

[59] E. Saitoh, M. Ueda, H. Miyajima, and G. Tatara. Conversion of spin current into charge current at room temperature: Inverse spin-hall effect. *Applied Physics Letters*, 88:182509, 2006.

[60] S.Y. Huang, WG. Wang, S.F. Lee, J. Kwo, and C.L. Chien. Intrinsic spin-dependent thermal transport. *Physical Review Letters*, 107(21), 2011.

[61] Y. Pu, E. Johnston-Halperin, D. D. Awschalom, and J. Shi. Anisotropic thermopower and planar nernst effect in $\mathrm{ga}_{1-x}\mathrm{mn}_x\mathrm{As}$ ferromagnetic semiconductors. *Physical Review Letters*, 97:036601, 2006.

[62] V.D. Ky. Planar hall and nernst effect in ferromagnetic metals. *Physica Status Solidi (b)*, 22:729–736, 1967.

[63] A.D. Avery, Rubina Sultan, D. Bassett, D. Wei, and B.L. Zink. Thermopower and resistivity in ferromagnetic thin films near room temperature. *Physical Review B*, 83(10), 2011.

[64] A. D. Avery, M. R. Pufall, and B. L. Zink. Determining the planar nernst effect from magnetic-field-dependent thermopower and resistance in nickel and permalloy thin films. *Phys. Rev. B*, 86:184408, 2012.

[65] K. Uchida, T. Ota, K. Harii, K. Ando, H. Nakayama, and E. Saitoh. Electric detection of the spin-seebeck effect in ferromagnetic metals (invited). *Journal of Applied Physics*, 107(9):09A951–09A951–5, 2010.

[66] R. C. O'Handley. *Modern Magnetic Materials: Principles and Applications*. John Wiley & Sons, Inc, New York, 2000.

[67] A. D. Avery, M. R. Pufall, and B. L. Zink. Observation of the planar nernst effect in permalloy and nickel thin films with in-plane thermal gradients. *Phys. Rev. Lett.*, 109:196602, 2012.

[68] N. Liebing, S. Serrano-Guisan, K. Rott, G. Reiss, J. Langer, B. Ocker, and H. W. Schumacher. Tunneling magnetothermopower in magnetic tunnel junction nanopillars. *Physical Review Letters*, 107:177201, 2011.

[69] M.J. Conover, M.B. Brodsky, J.E. Mattson, C.H. Sowers, and S.D. Bader. Magnetothermopower of fe / cr superlattices. *Journal of Magnetism and Magnetic Materials*, 102(12):L5 – L8, 1991.

[70] L. Piraux, A. Fert, P. A. Schroeder, R. Loloee, and P. Etienne. Large magnetothermoelectric power in co/cu, fe/cu and fe/cr multilayers. *Journal of Magnetism and Magnetic Materials*, 110(3):L247 – L253, 1992.

[71] Jing Shi, S. S. P. Parkin, L. Xing, and M. B. Salamon. Giant magnetoresistance and magnetothermopower in co/cu multilayers. *Journal of Magnetism and Magnetic Materials*, 125(3):L251 – L256, 1993.

[72] Jing Shi, Kevin Pettit, E. Kita, S. S. P. Parkin, R. Nakatani, and M. B. Salamon. Field-dependent thermoelectric power and thermal conductivity in multilayered and granular giant magnetoresistive systems. *Phys. Rev. B*, 54:15273–15283, 1996.

[73] S. Serrano-Guisan, L. Gravier, M. Abid, and J.-Ph. Ansermet. Thermoelectri-

cal study of ferromagnetic nanowire structures. *Journal of Applied Physics*, 99(8):08T108, 2006.

[74] Stephen Soffer, James A. Dressen, and Emerson M. Pugh. Hall effects, resistivity, and thermopower in fe and $\mathrm{fe}_{1-x}\mathrm{ni}_x$ for $x = 0$ to 0.2. *Phys. Rev.*, 140:A668–A675, 1965.

[75] R. S. Popovic. *Hall Effect Devices Second Edition*. IOP Publishing Ltd, 2004.

[76] F. L. Bakker, A. Slachter, J.-P. Adam, and B. J. van Wees. Interplay of peltier and seebeck effects in nanoscale nonlocal spin valves. *Phys. Rev. Lett.*, 105:136601, 2010.

[77] J. Flipse, F. L. Bakker, A. Slachter, F. K. Dejene, and B. J. van Wees. Direct observation of the spin-dependent peltier effect. *Nat Nano*, 7:166–168, 2012.

[78] Lon E. Bell. Cooling, heating, generating power, and recovering waste heat with thermoelectric systems. *Science*, 321(5895):1457–1461, 2008.

[79] Ihtesham Chowdhury, Ravi Prasher, Kelly Lofgreen, Gregory Chrysler, Sridhar Narasimhan, Ravi Mahajan, David Koester, Randall Alley, and Rama Venkatasubramanian. On-chip cooling by superlattice-based thin-film thermoelectrics. *Nature Nanotechnology*, 4(4):235–8, 2009.

[80] Arun Majumdar. Thermoelectric devices: Helping chips to keep their cool. *Nature Nanotechnology*, 4(4):214–5, 2009.

[81] Lars Onsager. Reciprocal relations in irreversible processes. i. *Phys. Rev.*, 37:405–426, 1931.

[82] I. Weinberg. Phonon-drag thermopower in dilute copper alloys. *Phys. Rev.*, 146:486–489, 1966.

[83] G. N. Grannemann and L. Berger. Magnon-drag peltier effect in a ni-cu alloy. *Phys. Rev. B*, 13:2072–2079, 1976.

[84] A. T. Fiory and B. Serin. Observation of a "peltier" effect in a type-ii superconductor. *Phys. Rev. Lett.*, 16:308–310, 1966.

[85] Hilmar Straube, Jan-Martin Wagner, and Otwin Breitenstein. Measurement of the peltier coefficient of semiconductors by lock-in thermography. *Applied Physics Letters*, 95(5):052107, 2009.

[86] Helin Zou, D.M. Rowe, and S.G.K. Williams. Peltier effect in a co-evaporated sb2te3(p)-bi2te3(n) thin film thermocouple. *Thin Solid Films*, 408:270 – 274, 2002.

[87] J. Jimenez, E. Rojas, and M. Zamora. Device for simultaneous measurement of the peltier and seebeck coefficients: Verification of the kelvin relation. *Journal of Applied Physics*, 56(11):3250–3255, 1984.

[88] A. Fukushima, H. Kubota, A. Yamamoto, Y. Suzuki, and S. Yuasa. Peltier effect in metallic junctions with cpp structure. *Magnetics, IEEE Transactions on*, 41(10):2571 – 2573, oct. 2005.

[89] E. Meyer. Atomic force microscopy. *Progress in Surface Science*, 41(1):3 – 49, 1992.

[90] G. Binnig, C. F. Quate, and Ch. Gerber. Atomic force microscope. *Phys. Rev. Lett.*, 56:930–933, 1986.

Appendix A: Bulk Sample Transfer Technique

A future direction for our thermal conductivity measurements is to probe thermal transport through bulk samples. We modified the platform design to enable bulk measurements by increasing both the size and the thickness of the membrane structure. The original version of the bulk structures was 1000 μm thick rather than the 500 nm thickness of the thin film thermal isolation platforms. This increase in size and thickness provides a larger surface for bulk support as well as additional strength in the supporting membrane. To attach the sample, some type of adhesive must be used, so that the sample doesn't fall off of the platform when the chip is mounted to the cold finger of the cryostat. Although I experimented with GE varnish, silver paint is a much better choice for adhesive. I could easily thin the paint with Ag paint thinner if it was too thick. Also, since it is a conductive paint, heat will easily transfer through it to the bulk sample. In order to prevent the heaters and thermometers on each island from shorting together, I deposited a thin layer of alumina on the islands to insulate the important wiring on the platform.

The next step is to transfer the adhesive to the islands. To do this I used a modified "bubble wand". Even though these bulk platforms are larger than the

typical platforms, the islands are still tiny, so a small instrument is needed to transfer adhesive. A spare piece of the wire for the Janus cryostat worked nicely because it was the thinnest wire in the lab at the time. I used 1 of the 4 twisted wires and cut a small piece about 2 inches in length. Next, I formed a small loop at the end of the wire by grabbing the very end with sharp tweezers and looping the wire around the tip. This formed a loop about the size of one island. I would double check the size of the loop next to the island through the bonder microscope without touching the island. Avoid loops larger than the island because they can transfer enough adhesive to connect the island to the bottom of the etch pit and form a thermal link. Finally, I bent the wire so that the loop was close to a 90^o angle to the rest of the wire, forming a handle.

Next, I transferred a small amount of Ag paint onto a glass slide. This made it easy to dip the loop into the paint without grabbing too much or dipping too deeply into the paint vial. The viscosity of the paint is important. If the paint is too thick, it will make a big glob on top of the loop and transfer to the island will be difficult. If it is too runny, it will be difficult to get any to stay in the loop. Once the paint has the right consistency, I would dip the loop in the paint and then **gently** touch the loop to the surface of one island. The silver paint will form a nice meniscus and coat the entire island. Repeat this step for the opposite island. The Ag paint will dry fairly quickly, so this should be done as quickly (and gently) as possible.

The final step is to transfer the sample onto the adhesive coated islands. Have the sample ready to pick up with tweezers immediately after applying the Ag paint. Sharp tweezers work best for this because the smaller surface area reduces the amount of contact between the tweezers and the sample is less likely to stick to the tweezers. The transfer the sample to the islands by holding it right above both

islands and opening the tweezers. The sample should drop right onto the islands gently enough that the suspended structures on each side stay intact. Fig. A-1 shows a bulk quartz sample and bulk Si samples mounted on bulk platforms.

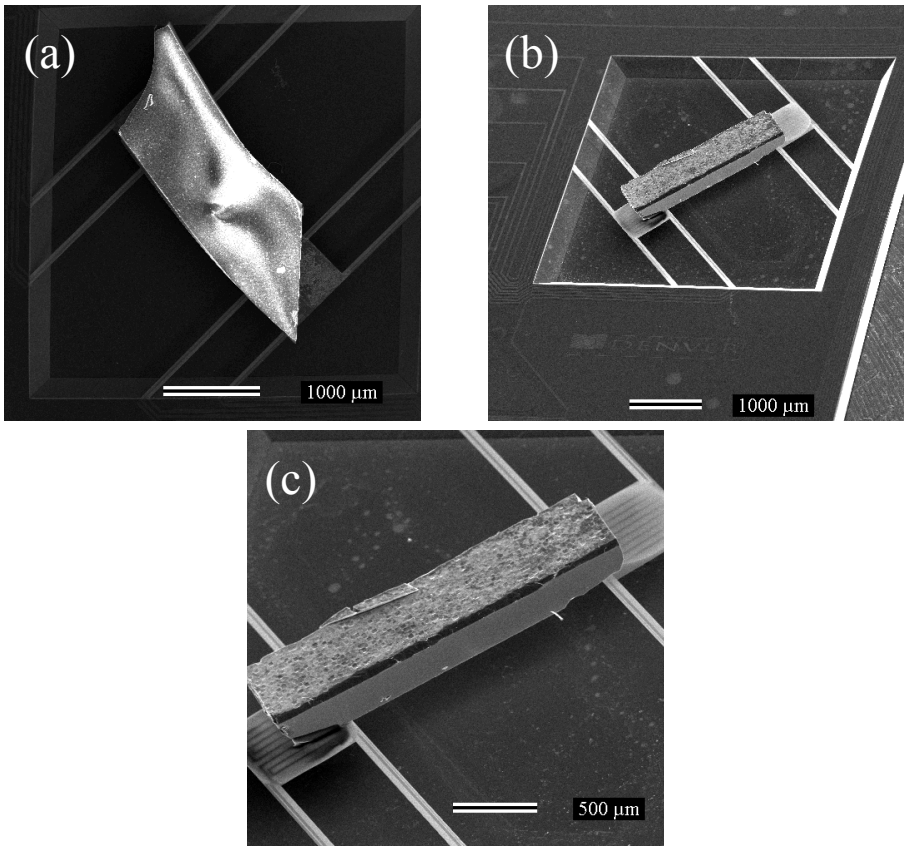

Figure A-1: (a) SEM micrograph of a bulk quartz sample on a bulk platform. (b) SEM micrograph of a bulk Si sample on a bulk platform. (c)SEM micrograph zoom of a bulk Si sample on a bulk platform.

Appendix B: MATLAB Code for Transferring Xic File

The layout for the thermal isolation platforms is a fairly complicated structure made up of many, many rectangles. To generate a heat flow model using MATLAB's PDE toolbox, it is possible to draw this all in by hand (or mouse). However, it's much easier to convert the Xic file used during fabrication to a file format readable by the PDE toolbox. In the following section, I have included my code for converting from Xic file to PDE.

```
function  A = convertCifToPde(xicfile,pdefile)
%convertCifToPde('xicfile.txt','pdefile.m')
%convertCifToPde takes geometry file from XIC and rewrites for PDEtool
%inputs are xicfile with a .txt extension and pdefile with a .m extension

format long e;
%%%%%%%%%%%%%%%%%%%%%%%%%%%%%%%%%%%%%%%%%%%%%%%%%%%%%%%%%%%%%%%%%%%%%%%
%
% Create data_array from lines of Xic file
% Open Pdefile and assign a "name"
%%%%%%%%%%%%%%%%%%%%%%%%%%%%%%%%%%%%%%%%%%%%%%%%%%%%%%%%%%%%%%%%%%%%%%%
%
data_array = readFileIntoArray(xicfile);
PdeFile = fopen(pdefile, 'wt');


%%%%%%%%%%%%%%%%%%%%%%%%%%%%%%%%%%%%%%%%%%%%%%%%%%%%%%%%%%%%%%%%%%%%%%%
%
% Set header and plot variables
%%%%%%%%%%%%%%%%%%%%%%%%%%%%%%%%%%%%%%%%%%%%%%%%%%%%%%%%%%%%%%%%%%%%%%%
%
 header = char('function pdemodel',...
     '[pde_fig,ax]=pdeinit;',...
     'pdetool(',...
     'appl_cb',...
     ',9);');

 aspectRatio = char('set(ax,',...
     'DataAspectRatio',...
     ',[1 1 1]);',...
     'set(ax,',...
     'PlotBoxAspectRatio',...
     ',[1 1 1]);');

 limits = [-3e-003,3e-003];
 axes = char('X','Y');


%%%%%%%%%%%%%%%%%%%%%%%%%%%%%%%%%%%%%%%%%%%%%%%%%%%%%%%%%%%%%%%%%%%%%%%
%
% Print header and axes settings
%%%%%%%%%%%%%%%%%%%%%%%%%%%%%%%%%%%%%%%%%%%%%%%%%%%%%%%%%%%%%%%%%%%%%%%
%
 fprintf(PdeFile,'%s\n%s\n%s\"%s\"%s\n',...
     header(1,:),header(2,:),deblank(header(3,:)),...
     deblank(header(4,:)),header(5,:));
```

Figure B-1: convertCifToPDE page 1

```
fprintf(PdeFile,'%s\''%s\''%s\n%s\''%s\''%s\n',...
    deblank(aspectRatio(1,:)),...
    deblank(aspectRatio(2,:)),...
    deblank(aspectRatio(3,:)),...
    deblank(aspectRatio(4,:)),...
    aspectRatio(5,:),aspectRatio(6,:));

fprintf(PdeFile,'set(ax,\''XLim\'',[%d %d]);\n',limits(:,1),limits(:,2));
fprintf(PdeFile,'set(ax,\''YLim\'',[%d %d]);\n',limits(:,1),limits(:,2));


for i = 1:2
     fprintf(PdeFile,'set(ax,\''%sTick\'',[%d,...\n',axes(i,:),limits(:,1));
     for j = -2:3
         fprintf(PdeFile,'%de-003,...\n',j);
     end
     fprintf(PdeFile,']);\n');
end

fprintf(PdeFile,'\n\n%% Geometry description:\n');



%%%%%%%%%%%%%%%%%%%%%%%%%%%%%%%%%%%%%%%%%%%%%%%%%%%%%%%%%%%%%%%%%%%%%%%%
%
% Loops through each line and converts CIF geom to PDE geom
%%%%%%%%%%%%%%%%%%%%%%%%%%%%%%%%%%%%%%%%%%%%%%%%%%%%%%%%%%%%%%%%%%%%%%%%
%
index = numel(data_array);
boxcount = 0;
polycount = 0;

for i = 1:index
   %for rectangles
   if regexp(data_array{1,i},'^B\s.+')
       boxcount = boxcount + 1;

       %split line into token (before first space) and remain (everything
       %after
       [token remain] = strtok(data_array{1,i});

       %convert string to number
       b = str2num(remain);

       %convert XIC box geometry to PDE rectangle geometry
```

Figure B-2: convertCifToPDE page 2

```
        pdeRectangleGeom = convertBoxGeom(b);

        % write new geom to file
        % \" is the escape for single quotes
        fprintf(PdeFile,'pderect([%d %d %d %d],\"R%d\")\n',pdeRectangleGeom,boxcount);

    %for polygons
    elseif regexp(data_array{1,i},'^P\s.+')
        polycount = polycount + 1;

        %Separate beginning letter from coordinates
        [token remain] = strtok(data_array{1,i});

        %trim leading whitespace from remain
        remain = strtrim(remain);

        %split remain on whitespaces
        xandy = regexp(remain,'\s*','split');

        %convert to double and change to microns
        xandy = str2double(xandy);
        xandy = convertPolyGeom(xandy);

        %determine number of columns for use in for loop
        columnNum = numel(xandy);

        xcount = 0;
        ycount = 0;
        fprintf(PdeFile,'pdepoly([');

        %for loops to separate xandy into x array then y array
        %x array
        for j = 1:columnNum-2
            xcount = xcount + 1;
            if isodd(j)
%                 sprintf('j = %d and x = %d,...',j,xandy(1,j))
                fprintf(PdeFile,'%d,...\n',xandy(1,j));
            end
        end

        fprintf(PdeFile,'],...\n[')

        %y array
        for k = 1:columnNum-2
            ycount = ycount + 1;
            if iseven(k)
```

Figure B-3: convertCifToPDE page 3

```
%              sprintf('k = %d and y = %d,...',k,xandy(1,k))
             fprintf(PdeFile,'%d,...\n',xandy(1,k));
          end
       end
       fprintf(PdeFile,'],...\n\"P%d\");\n',polycount);

%    else break;
   end
end



%%%%%%%%%%%%%%%%%%%%%%%%%%%%%%%%%%%%%%%%%%%%%%%%%%%%%%%%%%%%%%%%%%%%%%%%%%%%
%
% Close files
%%%%%%%%%%%%%%%%%%%%%%%%%%%%%%%%%%%%%%%%%%%%%%%%%%%%%%%%%%%%%%%%%%%%%%%%%%%%
%
fclose(PdeFile);
```

Figure B-4: convertCifToPDE page 4

```
function F = convertBoxGeom(A)
%CONVERTBOXGEOM converts box geom from XIC CIF file to PDEtool geometry
% convertBoxGeom converts box geom from XIC CIF file to PDEtool geometry

% Convert to microns
Amicron = A/1000*1E-6;

% Define elements from CIF geometry
xhalf = Amicron(:,1)/2;
yhalf = Amicron(:,2)/2;
xmid = Amicron(:,3);
ymid = Amicron(:,4);

% Convert to xmin/max and ymin/max
xmin = xmid - xhalf;
xmax = xmid + xhalf;
ymin = ymid - yhalf;
ymax = ymid + yhalf;

% Build new array with converted min/max values for PDEtool use
F = [xmin xmax ymin ymax];
```

Figure B-5: convertBoxGeom

```
function Amicron = convertPolyGeom(array)
% CONVERTPOLYGEOM converts poly geom from XIC CIF file to PDEtool geometry
% convertBoxGeom converts poly geom from XIC CIF file to PDEtool geometry

% Convert to microns
Amicron = array/1000*1E-6;
```

Figure B-6: convertPolyGeom

```
function array = readFileIntoArray(XicFile)
%READFILEINTOARRAY reads the XIC CIF file into one array
% This array can then be split using ; as the delimiter
% Usage readFileIntoArray('filename.txt')
file = fopen(XicFile);
char_array = '';
while true
    line = fgetl(file);
  if ischar(line)
     char_array = strcat(char_array, line);
  else break
  end
end
array = regexp(char_array,';','split');
fclose(file);
```

Figure B-7: readFileIntoArray

```
function x = iseven(number)
% iseven(number)
% returns 1 if the number is Odd, 0 if it is even.

a = number/2;
remain = a-floor(a);

if remain == 0;
   x = 1;
else
   x = 0;

end
```

Figure B-8: iseven

```
function x = isodd(number)
% isodd(number)
% returns 1 if the number is Odd, 0 if it is even.

a = number/2;
remain = a-floor(a);

if remain > 0;
   x = 1;
else
   x = 0;

end
```

Figure B-9: isodd

Appendix C: Error Analysis

Thermal Conductance Error

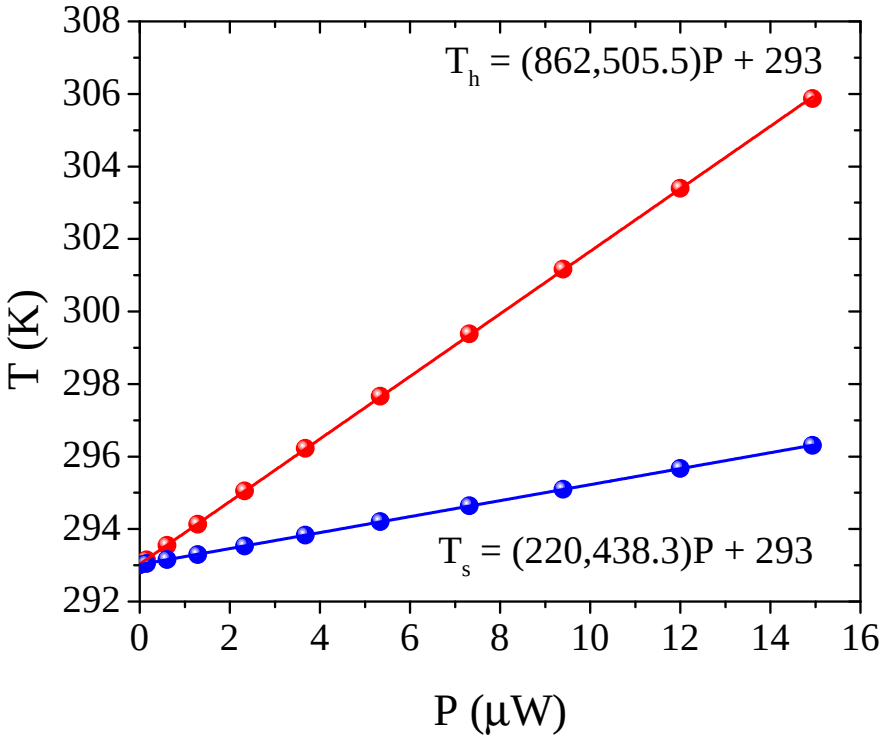

Figure C-1: Temperature as a function of heating power for the hot side of a 75 nm thick Cu film T_h and the cold side of the film T_s. The slopes from the linear fits to both hot and cold sides are functions that can be solved for K_B and K_L.

To analyze the error for a thermal conductivity experiment, the first step is to express K_B and K_L in terms of measured values. We measure the increase in T_h and T_s with increasing P. The slopes from the linear fits to both hot and cold sides are functions that can be solved for K_B and K_L.

$$T_h = m_{Th}P + T_o \tag{C-1}$$

$$T_s = m_{Ts}P + T_o \tag{C-2}$$

The steady state heat flow equations for our experimental thermal model can be solved for K_B and K_L.

$$K_L = \frac{P}{(T_h - T_o) + (T_s - T_o)} \tag{C-3}$$

$$K_B = \frac{1}{2}\left[\frac{P}{T_h - T_s} - K_L\right]. \tag{C-4}$$

Next we substitute the expressions for $(T_h - T_o) = m_{Th}P$, $(T_s - T_o) = m_{Ts}P$ and $(T_h - T_s) = m_{Th}P - m_{Ts}P$ into Eqns. C-3 and C-4 and simplify to obtain K_B and K_L as an expressed of directly measured values.

$$K_L = \frac{1}{m_{Th} + m_{Ts}} \tag{C-5}$$

$$K_B = \frac{m_{Ts}}{(m_{Th} + m_{Ts})(m_{Th} - m_{Ts})} \tag{C-6}$$

The uncertainty in the slope of a line generated through least squares fitting is

$$\delta m = \delta T \sqrt{\frac{N}{N\Sigma P^2 - (\Sigma P)^2}} \tag{C-7}$$

where N is the number of data points.

To determine T, we fit a polynomial to the function representing $T(R)$ for each thermometer. Multiplying the derivative of this function for each thermometer by the resolution of the SRS AC resistance bridge (δR) gives the error in temperature specific to each thermometer $\delta T = \delta R \frac{dT}{dR}$. Next, we calculate $\delta(m_{Th} \pm m_{Ts}) = \sqrt{(\delta m_{Th})^2 + (\delta m_{Ts})^2}$ using error propagation.

After determining δT, δm_{Th}, δm_{Ts}, and $\delta(m_{Th} \pm m_{Ts})$ simple propagation of errors yields equations for the fractional uncertainty of K_B and K_L.

$$\frac{\delta K_L}{K_L} = \sqrt{\left(\frac{\delta(m_{Th} \pm m_{Ts})}{(m_{Th} + m_{Ts})}\right)^2} \tag{C-8}$$

$$\frac{\delta K_B}{K_B} = \sqrt{\left(\frac{\delta m_{Ts}}{m_{Ts}}\right)^2 + \left(\frac{\delta(m_{Th} \pm m_{Ts})}{(m_{Th} + m_{Ts})}\right)^2 + \left(\frac{\delta(m_{Th} \pm m_{Ts})}{(m_{Th} - m_{Ts})}\right)^2} \tag{C-9}$$

Seebeck Coefficient Error

The thermopower α is the slope of the linear fit to the $\triangle V$ across a film as a function of $\triangle T$. Therefore

$$\delta\alpha = \delta V \sqrt{\frac{N}{N\Sigma\triangle T^2 - (\Sigma\triangle T)^2}} \tag{C-10}$$

where V is the voltage resolution measurement from a Keithley 2400 Sourcemeter or a Keithley 2182A Nanovoltmeter.

Peltier Coefficient Error

The Peltier coefficient Π is the slope of the linear fit to the applied I. The equation for P_Π is

$$P_\Pi = (\frac{1}{2}K_L + K_B)(T_h - T_s). \tag{C-11}$$

Using the values for δK_B and δK_L determined from the thermal conductance error analysis and $\delta T = \delta R \frac{dT}{dR}$ for the hot and cold thermometers in the Peltier experiment, we determine

$$\delta(K_L + K_B) = \sqrt{(\delta K_L)^2 + (\delta K_B)^2} \tag{C-12}$$

and

$$\delta(T_h - T_s) = \sqrt{(\delta T_h)^2 + (\delta T_s)^2}. \tag{C-13}$$

The P_Π fractional error is

$$\frac{\delta P_\Pi}{P_\Pi} = \sqrt{\left(\frac{\delta(K_L + K_B)}{\frac{1}{2}K_L + K_B}\right)^2 + \left(\frac{\delta(T_h - T_s)}{T_h - T_s}\right)^2}. \tag{C-14}$$

Finally, to determine $\delta\Pi$, we calculate the error for the slope to the linear fit.

$$\delta\Pi = \delta P_\Pi \sqrt{\frac{N}{N\Sigma I^2 - (\Sigma I)^2}} \tag{C-15}$$

Appendix D: AFM/MFM notes

In 1986, Gerd Binnig, Calvin Quate, and Christoph Gerber designed a microscope that measured the forces between a sample and a scanning tunneling microscope (STM) probe rather than tunneling currents (89). They originally designed the AFM to increase the sensitivity of STM measurements in order to probe interatomic forces between atoms. The small mass of the cantilever beam allows smaller forces (on the order of 10^{-18} N) to move the cantilever (90).

Atomic force microscopy employs a probe tip that is attached to a cantilever spring. The force between the probe tip and the sample surface causes the lever to be deflected when the probe is moved into close proximity with a sample. Moving the probe across the surface causes deflections of the probe as the forces between the sample and the tip change. These deflections in the z-direction are coupled with the x and y location of the stage and converted to 2-D and 3-D images of the sample. When the forces between the sample and the probe are smaller than interatomic forces, imaging is non-destructive. There are two operating modes for AMF imaging: contact and non-contact. In non-contact mode at heights of 10 to 100 nm, van der Waals, electrostatic, and magnetic forces enable probes of roughness and topography, charge distribution, and magnetic domain imaging. In contact mode, the sample and the probe tip are in contact with each other. Intermolecular forces

enable high resolution imaging of the sample surface (89).

I performed thickness calibrations, measured surface roughness, and imaged magnetic domains in a ferromagnetic samples using the AFM. In all AFM images I used a soft engage to engage the probe tip. Asylum has an informative manualette on their website that describes how to load a probe tip, engage the tip with the sample, and run a scan. This is the most conservative way to engage the tip for a scan and helps to preserve the lifetime of the tip.

Once the images are obtained, the next important step is the image analysis. Raw images from the AFM often appear tilted or bowed. These artifacts are introduced by the scanning mechanism of the AFM. There are two functions in the AFM software to remove these artifacts, Flatten and Planefit. Flatten removes artifacts due to Z-axis scanner drift. The order of flattening necessary depends on the nature of the artifact observed in the image scan. For example a zero order flatten corrects for Z offset between each line while a first order flatten corrects for Z offset and the tilt. If the surface in the 3-D mode does not appear too inclined, then a flatten order 0 is usually sufficient. Planefit is similar to the flatten but works in the x-y plane of the stage. It is also used to remove artifacts such as tilting and bowing.

AFM: Thickness Calibration

For the thickness calibration shown in Fig. D-1, I used tapping mode (also called non-contact or AC mode) to image this sample. It is important to use the channel appropriate for the feature height when performing thickness calibrations. Use the height channel for films less than 100 nm, and the Z sensor channel for features over a 100 nm. (a) shows the flattened height trace and (b) shows the flattened 3-D plot for this image. The vertical red line in (a) is the line drawn for a

thickness measurement. I used the Section tab on the Analyze panel to draw a line for analysis. The plot in Fig. D-1 (c) displays the actual thickness of the Au layer. Although the Veeco thermal evaporator crystal monitor indicated a 20 nm thick Au layer, the actual thickness of this Au layer was close to 17 nm.

Since the AFM scans horizontally, the best way to determine height is by using a line in the horizontal direction. This gives a measurement of the feature height with respect to the surface of a sample without the averaging necessary from line to line in a vertical direction. Fig. D-2 shows a thickness calibration using a horizontal line to determine the feature height. These measurements indicate the Au bars were roughly 24 nm. Therefore, my thickness calibrations placed the thickness of these bars between 17 and 24 nm, which is close to the target thickness of 20 nm.

AFM: Surface Roughness

I measured the surface roughness for a SiO_2 substrate and a Si substrate. I scanned both substrates using an MFM tip because I was working on magnetic imaging at the time. To determine the roughness, use the Roughness tab on the Analyze Panel. The masking tool on this panel is very helpful when you have a substrate with metal features on it. Using the mask you can determine the roughness of either the substrate or the metal. We determine the roughness using the RMS values, or the standard deviation values for the elevation. The roughness values determined for the samples shown in Fig. D-3 are 150 nm for the SiO_2 and 247 pm for the Si substrate.

MFM: Magnetic Domain Imaging

To image magnetic domains in a sample you'll need a tip with a magnetic moment. There are several types of magnetic tips and the choice of tip depends on the magnetic property of the sample you are trying to scan. I ran my first scans using Budget Sensor Multi 75N-G magnetic tips. These are fairly standard MFM tips. After scanning a few permalloy samples with little success, nanoandmore.com recommended PPP-LM-MFMR tips for permalloy and SSS-MFMR or PPP-MFMR for Ni and Fe. The LM stands for low moment and the SS stands for super sharp. When using the between the AFM in MFM mode, you'll need to turn on the special imaging mode known as the NAP pass. In MFM imaging, the trace works like a normal AFM scan and gives topographical information. The retrace lifts up the probe up to a predetermined height, which is high enough so that short range forces no longer effect the tip, and tip deflection results from the interaction of longer range forces such as stray magnetic fields from the sample. This is known as the nap pass. I used tapping mode for MFM scans. When using tapping mode, you can use a smaller drive amplitude on the nap pass. This will push the tip closer to the sample surface during this pass. Note that the default drive amplitude is set at 1 V. I found this was so high that the force of the cantilever oscillation was too high to be affected by the stray magnetic fields from the sample.

The magnetic information is contained in the nap phase and nap amplitude modes. Comparing these to the regular phase and amplitude modes help to determine which features are a result of topography and which are magnetic in origin. Features found on both regular and nap passes are topographical. Features revealed only on the nap pass are magnetic. Light areas represent attractive forces between

the tip and the sample, and darker areas represent repulsive forces. Fig. D-4 shows scans of a portion of magnetic computer memory. The phase scan shown in (a) looks fairly uniform. The nap phase scan in (b) reveals the presence of magnetic domains. Once I imaged magnetic domains successfully, I tried to image the magnetic domains of a film deposited on a suspended Si-N platform. Early in our SSE analysis, we questioned whether trapped domains under the Pt strip transverse voltage detector were responsible for the unexpected even field dependence we observed with reversal of magnetic field. I scanned several permalloy and nickel films to image these domains, if present. I found no evidence of trapped domains in either type of film. Fig. D-5 shows an example scan from these probes of trapped magnetic domains. A note of caution, permalloy presents a challenge with the current AFM setup. The coercivity of our permalloy was roughly 2 Oe. The combination of the magnets used to hold the sample mount and the AFM sample stage produce a field anywhere from 1.5 to 2.5 Oe, so any magnetic domains that may be formed in permalloy can be destroyed simply by installing a sample on the sample stage.

Other tips and hints

1. When the gain is set too high, the amplitude displays periodic oscillations.

2. If the scan rate is too high, the height trace and retrace will display the poor surface tracking by not lining up nicely together.

3. Sometimes it is better to scan faster. What might seem like a scan that needs to be slower may be the result of thermal drift. If this is the case, scanning faster will remove the drift artifacts.

4. Choose to save trace and retrace data for any channel you want to save. You

may want the extra information later on when you're analyzing the scan data. Soft engaging the tip often results in a set point that's too high for AC mode because the 95% free air value is very conservative. If the height trace and retrace aren't lining up nicely, the image looks streaked, and you can't see a clear image, slowing lowering the set point may help this.

5. Set scan points to 512 rather than 256. This gives better resolution and better images for large posters and papers.

6. If magnetic domains are present during MFM, one way to ensure this is not an artifact is to turn the sample 90^o. If the domains rotate as well, then they are not artifacts.

7. In MFM, if you don't see a Z voltage, try raising the drive amplitude.

8. In MFM, if you don't see a height image, try raising the drive amplitude a bit after lowering the set point.

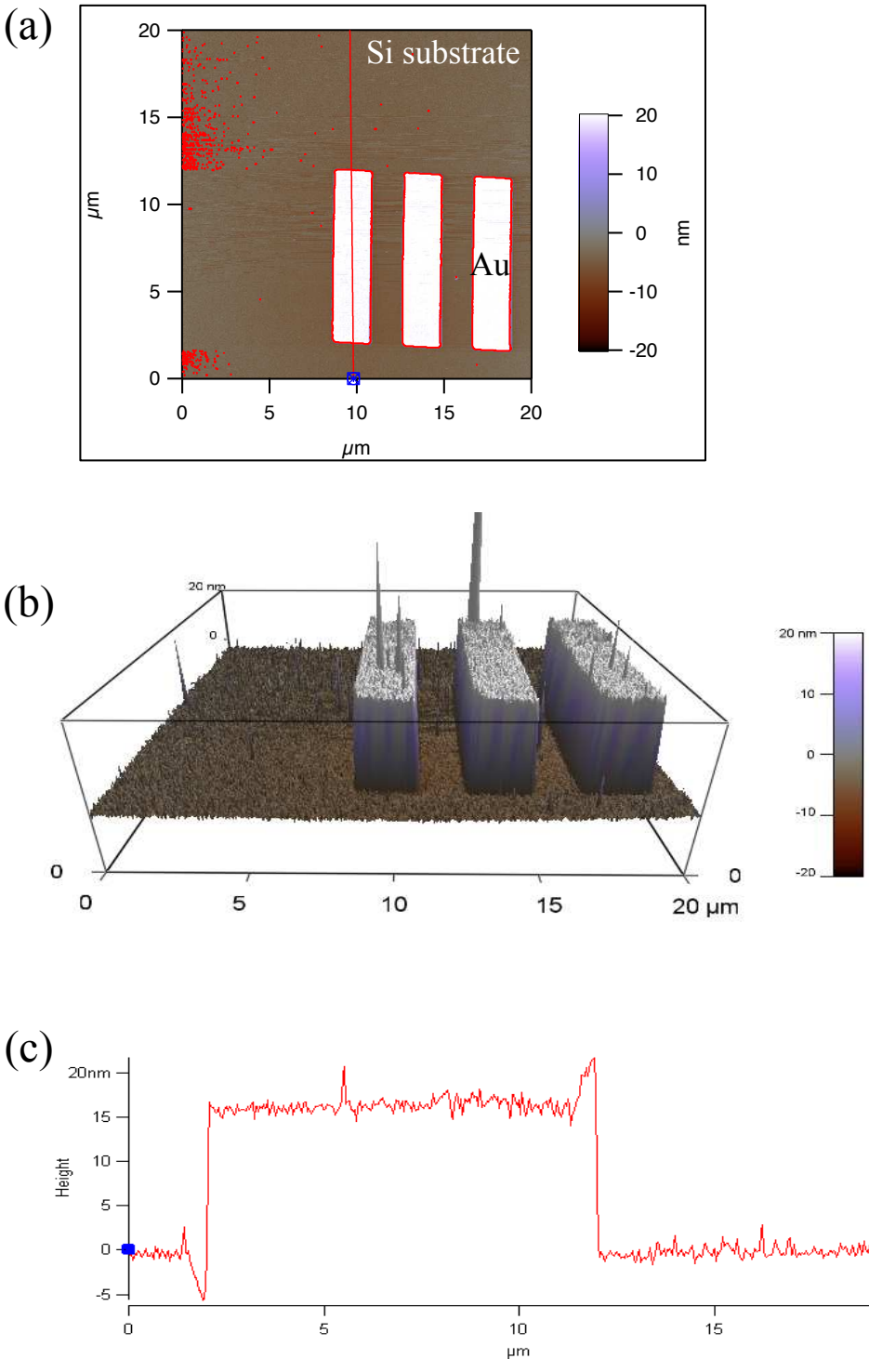

Figure D-1: (a) AFM image of 3 Au bars deposited on a Si substrate. (b) 3-D AFM image of Au on Si. (c) Height trace along the red line shown in (a). The height of these bars is roughly 17 nm.

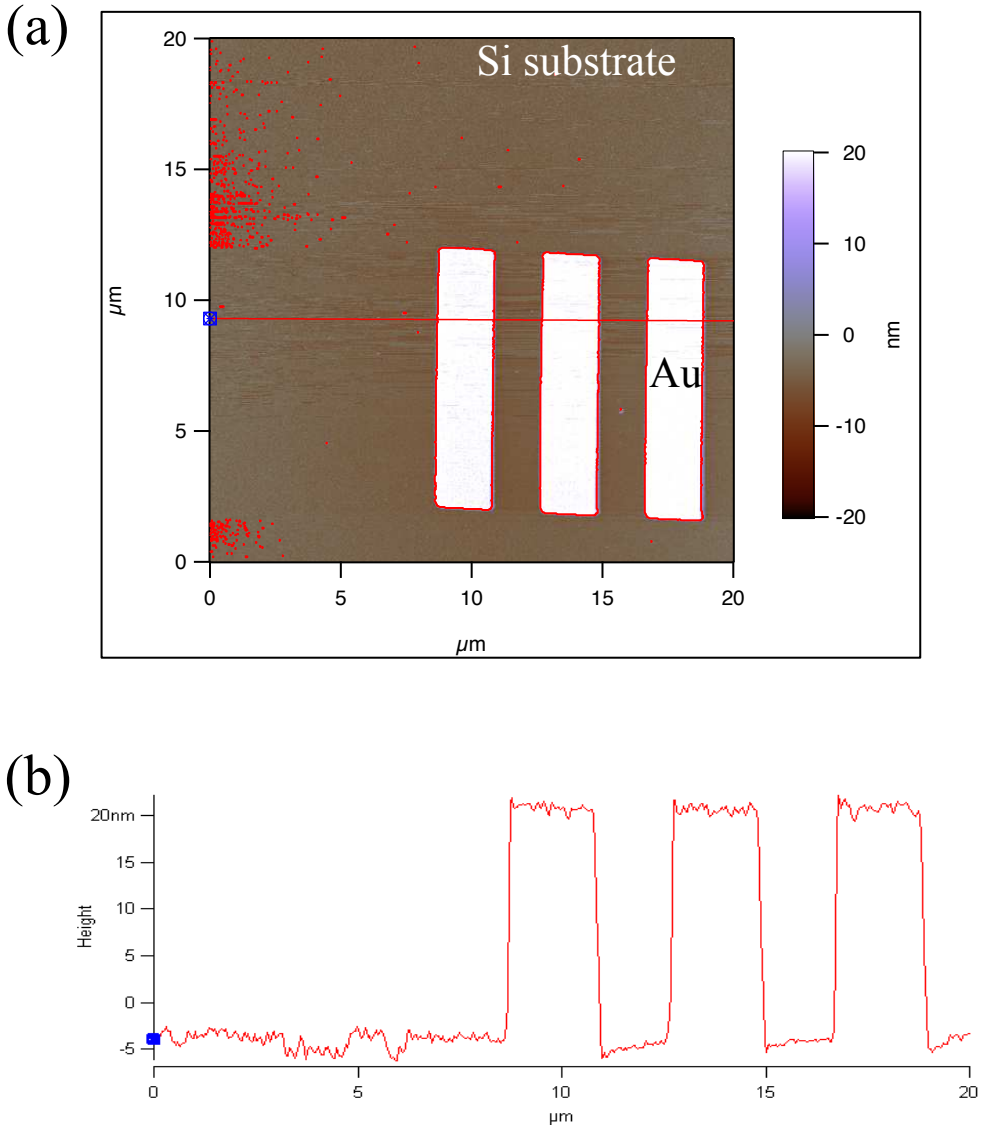

Figure D-2: (a) AFM image of 3 Au bars deposited on a Si substrate. (b) Height trace along the red line shown in (a). The height of these bars is roughly 24 nm.

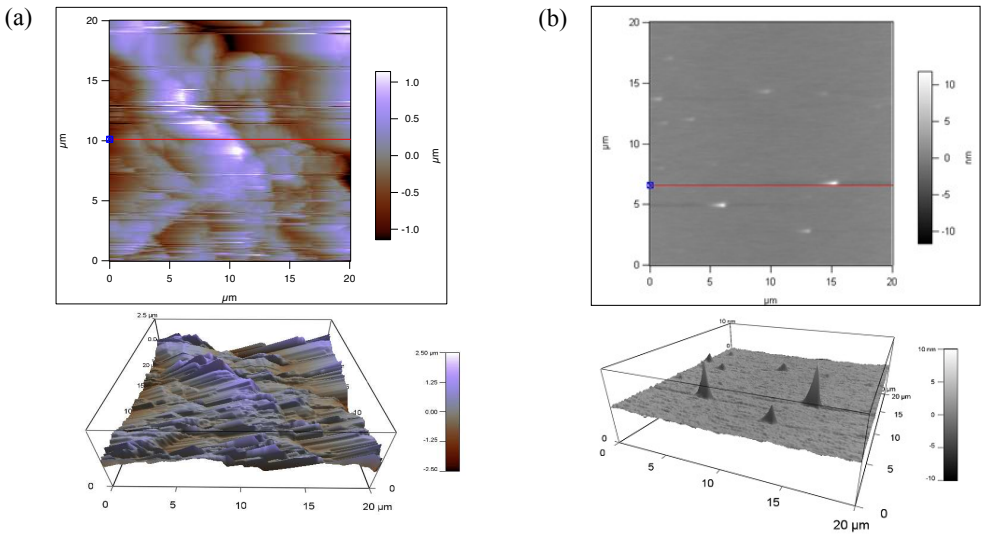

Figure D-3: (a) AFM images of a SiO_2 substrate. (b) AFM images of a Si substrate.

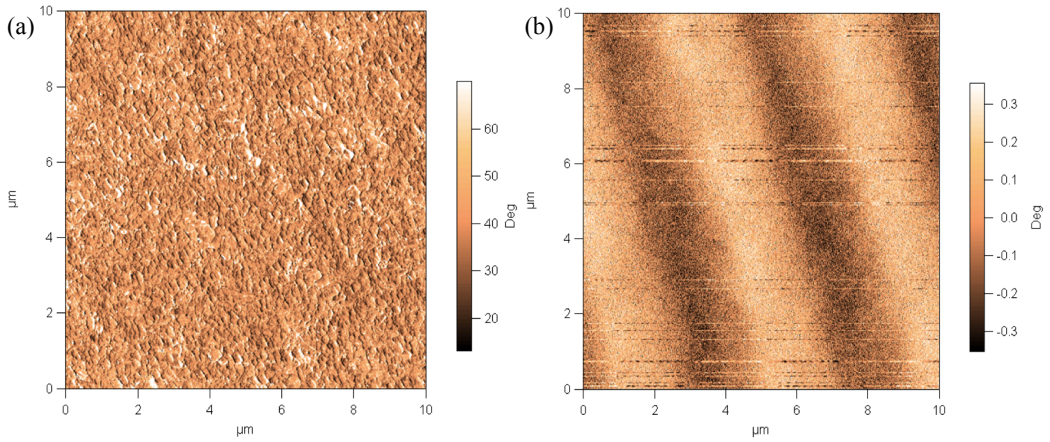

Figure D-4: (a) MFM phase image of magnetic computer memory. (b) MFM nap phase image magnetic computer memory.

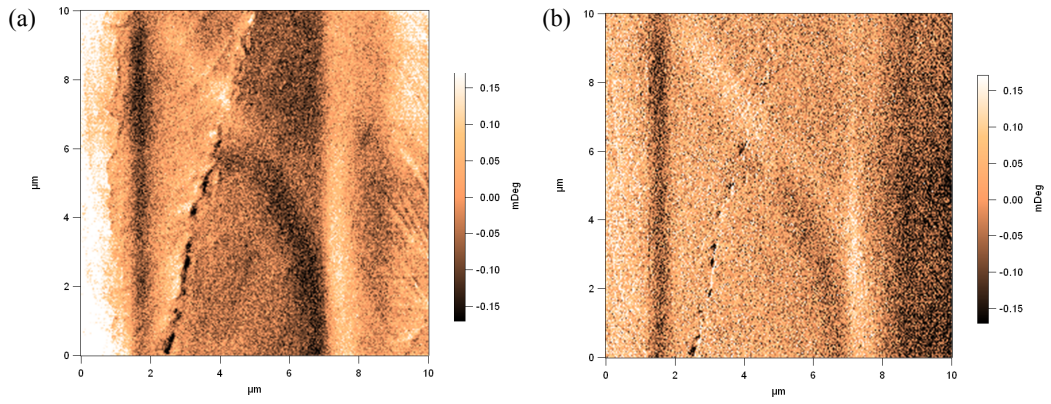

Figure D-5: (a) MFM phase image of a Pt strip for measuring V_T on a 20 nm thick permalloy film. (b) AFM nap phase image of a Pt strip for measuring V_T on a 20 nm thick permalloy film.

Appendix E: Tables of Films and Measurement Details

Film Number	Material	Thickness (nm)	Pre-Measured Bridge	Which Si-N Subtracted	Measurements	Growth Method	Base Pressure (torr)	Final Pressure (torr)
	Nickel	**50**	No		k, α, ρ, MTEP (950G)	NIST sputtered		
	Nickel	**100**	No		k, α	NIST sputtered		
13-09-37	**Nickel**	**83**	No	Py39	k, α, ρ	13er	1.00E-08	7.70E-07
	Nickel	**100**	No		ρ	NIST sputtered		
	Gold	**100**	No		k, α	Veeco		
13-09-30	**Ni-Fe**	**75**	No	from Py35	k, α, ρ, MTEP (950G)	13er	2.80E-09	7.40E-08
13-09-31	**Ni-Fe**	**60**	No	from Py35	k, α, ρ, hyst	13er	2.40E-09	6.50E-08
13-09-39	**Ni-Fe**	**75**	Yes	bz-062409-1 D4UR	k, α, ρ, MTEP (100G)	13er	7.80E-09	1.50E-08
13-10-51	**Ni-Fe**	**4**	No		k	13er		
13-10-01	**Cobalt**	**167**	Yes	bz-062409-1 C5LL	k, α, ρ	13er	1.00E-08	1.20E-07
13-10-07	**Cobalt**	**75**	Yes	bz-062409-1 C5UR	k, α, ρ, VdP	13er	6.00E-10	1.30E-08
13-10-06	**Copper**	**75**	Yes	bz-062409-1 A5UR	k, α, ρ, VdP	13er	3.80E-10	1.20E-08
	Chromium	**20**	No		k, α, ρ	Veeco		
13-10-09	**Chromium**	**93**	Yes	bz-062409-1 C2LL	k, α, ρ	13er	6.50E-10	1.20E-09
13-10-10	**Iron**	**75**	Yes	bz-062409-1 C3LL	k, α, ρ	13er	2.20E-08	2.50E-08
13-10-14	**Iron**	**65**	Yes	bz-062409-1 C6UR	k, α, ρ	13er	3.40E-09	1.70E-08

Figure D-6: Table of measurements for films grown on 2nd generation platforms with triangle shaped leads.

Film Number	Material	Thickness (nm)	Growth Rate (Å/s)	RT Resistivity (μΩ cm)	R film (Ω)	RRR	Date Measured	SRS Resolution (mΩ)	Fits	Notes
	Nickel	**50**					01/27/2009	56	7th order, 9 powers	
	Nickel	**100**					01/08/2009	56	8th order, all powers	
13-09-37	**Nickel**	**83**	0.9	19.5	60	1.65	11/17/2009	31	1st order, 7 points, 10 powers	1st new film with 3 mV excitation voltage
	Nickel	**100**					11/07/2008	56		Skinny Wires
	Gold	**100**					02/25/2009	56		Destroyed with the Keithley
13-09-30	**Ni-Fe**	**75**	4.0	68.3	210		09/15/2009	56	9th order, all powers	Short on Hot island btwn T2 and TEP lead. Heated cold island
13-09-31	**Ni-Fe**	**60**	13.0	61.2	235	1.19	09/30/0009	56	8th order, all powers	Hysteresis not exact
13-09-39	**Ni-Fe**	**75**	5.2	75.8	233	1.15	10/07/0009	56	9th order, all powers	
13-10-51	**Ni-Fe**	**4**					12/14/2010	31		Discont. film + bridge is background
13-10-01	**Cobalt**	**167**	1.0	50.4	155		01/13/2010	31	9th order, all powers	Dirty cobalt. ρ high.
13-10-07	**Cobalt**	**75**	1.0	19.5	60		02/19/2010	31	7th order, all powers	
13-10-06	**Copper**	**75**	1.0	8.1	25		02/15/2010	31	8th order, all powers	
	Chromium	**20**		347.4						Kboth too low to get + kCr.
13-10-09	**Chromium**	**93**	1.2	97.7	300		02/19/2010	31	8th order, 10 powers	
13-10-10	**Iron**	**75**	1.2	29.3	90	1.94	03/10/2010	31	7th order, all powers	
13-10-14	**Iron**	**65**	1.0		165	1.48	04/01/2010	31	1st order, 8 points, all	

Figure D-7: Table of measurements for films grown on 2nd generation platforms with triangle shaped leads.

PNE measurements of SSEflavors films

Film Number	Film	t (nm)	Measurements	Θ	Temp (K)	Publication	Date Measured	Notes
B4LL	**Au**	**20**	PNE Up Hyst	0	276		10/08/2011	
C4LL	**Au**	**20**	PNE, PNE Both Cold	0	276	PNE PRL	03/06/2012	
C4LL	**Au**	**20**	Peltier	0	296		10/30/2012	
C3LL	**Fe**	**20**	PNE	0	276		10/25/2011	Data files misnamed C1LL
C3LL	**Fe**	**20**	PNE Power Dependence	0	276		10/25/2011	
C3LL	**Fe**	**20**	Peltier Vs Temperature	0	78-324	Peltier PRB	02/04/2013	
E2UR	**Fe**	**20**	AMR	0	276		05/18/2012	
E2UR	**Fe**	**20**	PNE	0	162		05/29/2012	
E2UR	**Fe**	**20**	PNE	0	276		05/22/2012	
E2UR	**Fe**	**20**	k, TEP	0	78-324		05/07/2012	
E2UR	**Fe**	**20**	k, TEP sweep	0	162		05/15/2012	
E2UR	**Fe**	**20**	k, TEP sweep	0	276		05/16/2012	
E2UR	**Fe**	**20**	TEP (with Pt leads)	0	78-324		04/29/2012	
B5LL	**Ni**	**20**	PNE		276		10/27/11, 11/7/11	
B5LL	**Ni**	**20**	PNE (Coil)	90	276		11/05/2011	
B5LL	**Ni**	**20**	PNE Power Dependence		276		10/28/2011	
B5UR	**Ni**	**20**	k, TEP Reversed Islands	0	270-326		01/04/2013	
B5UR	**Ni**	**20**	Peltier Vs Temperature	0	80-304	Peltier PRB	12/6/12, 1/24/2013	Data from 1/24/13 best
B5UR	**Ni**	**20**	Peltier Reverse Legs	0	299		12/6/12, 1/24/13	Data from 1/24/13 best
B5UR	**Ni**	**20**	Peltier Sweep	0	299		01/11/2013	
D5LL	**Ni**	**20**	PNE	0	276	PNE PRL	03/19/2012	
D5LL	**Ni**	**20**	PNE	45, 90, 135	276		6/4/12, 6/5/12, 6/12/12	
E5UR	**Ni**	**20**	PNE	0	276		03/17/2012	
E5UR	**Ni**	**20**	AMR	0, 90	276, 300	PNE PRL, MTEP PRB	4/11/12, 4/12/12	
E5UR	**Ni**	**20**	AMR Diff Leads	0	300		05/04/2012	Various I,V lead combinations
E5UR	**Ni**	**20**	k, TEP	0	78-324		04/01/2012	

Figure D-8: Table of measurements for 20 nm thick films grown on SSEflavors wafer.

PNE measurements of SSEflavors films

Film Number	Film	t (nm)	Measurements	Θ	Temp (K)	Publication	Date Measured	Notes
E5UR	Ni	20	k, TEP sweep Rhot	0	276	MTEP PRB	04/09/2012	
E5UR	Ni	20	k, TEP sweep Lhot	0	276		04/10/2012	
E5UR	Ni	20	k, TEP sweep Rhot	0	226		04/11/2012	
E5UR	Ni	20	k, TEP sweep Rhot	90	276		07/12/2012	To double check artificial bump at end of data
E5UR	Ni	20	MTEP	0	276		07/12/2012	
E5UR	Ni	20	MTEP	90	276		07/24/2012	
E5UR	Ni	20	MTEP	90	276		8/8/12-8/10/12	8/5/12, Added zero-bin-averaging and removed Ground loop
E5UR	Ni	20	Peltier Sweep	0	296		07/06/2012	
E5UR	Ni	20	Peltier	0	299		11/16/2012	Good Data
B1LL	Ni-Fe	20	AMR	0	300		10/05/2011	
B1LL	Ni-Fe	20	PNE	0	276		9/19/11-9/30/11	Various adjustments of methodology
B1LL	Ni-Fe	20	PNE Power Dependence	0	276		01/01/2011	
B2LL	Ni-Fe	20	PNE	90	276		11/21/2011	
B2LL	Ni-Fe	20	PNE	0	276		11/25/2011	
B2LL	Ni-Fe	20	AMR	0	276		11/30/2011	
B2LL	Ni-Fe	20	AMR	90	276		12/16/2011	
B2LL	Ni-Fe	20	k, TEP	0	78-324		12/01/2011	
B2LL	Ni-Fe	20	MTEP	0	276		12/07/2011	
C1LL	Ni-Fe	20	PNE	0	276		02/07/2012	Data files misnamed C3LL
C1UR	Ni-Fe	20	PNE	0	276		02/08/2012	Data files misnamed C3UR
D1LL	Ni-Fe	20	PNE	0	276		10/09/2011	
D1UR	Ni-Fe	20	PNE, Power Dependence AMR	0	276		10/11/11-11/15/11	Bad Data. Series of changes with this including brass screws, added gaussmeter, and new naming convention
F3LL	Ni-Fe	20	PNE	0	276	PNE PRL	02/10/2012	
F3LL	Ni-Fe	20	PNE through film plane	90 (z)	276		02/13/2012	

Figure D-9: Table of measurements for 20 nm thick films grown on SSEflavors wafer.

PNE measurements of SSEflavors films

Film Number	Film	t (nm)	Measurements	Θ	Temp (K)	Publication	Date Measured	Notes
F3LL	Ni-Fe	20	PNE	45	276		02/15/2012	
A1LL	Ni-Fe b	20	PNE	0	276		02/17/2012	
A2UR	Ni-Fe b	20	PNE	90	276		02/23/2012	
E3LL	Ni-Fe b	20	PNE	0	276		03/11/2012	
E3LL	Ni-Fe b	20	k, TEP	0	78-326		03/22/2012	
E3LL	Ni-Fe b	20	MTEP	0	276		03/26/2012	4 powers Rhot
E3LL	Ni-Fe b	20	MTEP	0	276	MTEP PRB	03/27/2012	10 powers
E3LL	Ni-Fe b	20	MTEP	0	276		03/27/2012	10 powers, Lhot
E3LL	Ni-Fe b	20	MTEP	90	276	MTEP PRB	04/19/2012	
E3LL	Ni-Fe b	20	k	90	276		04/20/2012	
E3LL	Ni-Fe b	20	AMR	0	276	MTEP PRB	08/15/2012	
E3LL	Ni-Fe b	20	MTEP	0	276		08/16/2012	
E3LL	Ni-Fe b	20	AMR	90	276	MTEP PRB	08/29/2012	
E3LL	Ni-Fe b	20	Peltier	0	299		11/7/12-11/8/12	Not the best
E3LL	Ni-Fe b	20	Peltier	0	299		01/24/2013	Good Data
E3LL	Ni-Fe b	20	Peltier Vs Temperature	0	78-324	Peltier PRB	01/30/2013	

Figure D-10: Table of measurements for 20 nm thick films grown on SSEflavors wafer.

Appendix F: Experimental and Analysis Vi's: How to

SSE/PNE Experiments

IslandHeatingZero-Averaging.vi

This is the main Vi for the SSE/PNE experiments. Input the current necessary for creating $+\nabla T$, $-\nabla T$, and $\nabla T = 0$. The vi runs a quasi-AC method for measuring the resulting voltage developed in the y-direction (along the Pt lead). Raw data for the experiment are recorded from a series of NVM measurements: 20 with no power, 20 with power on, and 20 with no power. When plotted, the graph represents a step function. To correct for thermal drift, the vi plots data points 1-20 and 41-60, fits a straight line to the data, and subtracts this straight line from the raw data. After the subtraction, the raw data (now called subtracted data) are basically level and no power data points are close to 0 nV. However noise is still an issue since the voltages developed across these small Pt leads (35 μm across) are very small. To increase the signal-to-noise ratio, the vi will repeat this measurement 20 times and average all the data series with each additional step. For example, after the 1st measurement

of 60 and subtraction, the measurement is repeated. Then after subtracting off the thermal drift for the 2nd set of data, both of these data sets are averaged together in the following way. Both of the 1st data points are averaged, then the 2nd data points are averaged, etc. In this way, we are averaging each bin together. In this experiment, each bin is a data point, so there will be 60 bins. Outputs for this vi are the raw data, the subtracted data, and the bin-averaged data.

MasterSSEViWithField-V2.vi

This vi runs the SSE/PNE measurement for a series of external magnetic fields. Inputs to this vi are the starting magnetic field input current, the ending magnetic field input current, and the input current step size. The vi submits all input currents to the Keithley 6200 Precision Current Source. The 6200 is connected to the Kepco BOP 20/20 power supply connected to the magnet. Using the Keithley to input currents to the Kepco offers well-controlled current input that can be changed in small increments. For example, 10 μA starting current, -10 μA ending current, and 0.5 μA current step size inputs results in an 80 step array of currents that generate a magnetic field sweep from -39.1 Oe to 33.8 Oe in 1.7 Oe increments. At each magnetic field, this vi runs the IslandHeatingZero-Averaging.vi as a sub-vi.

MasterSSEHysteresisWithFieldV2.vi

This is the top level vi for the SSE/PNE measurement. Use this vi to generate an entire magnetic field sweep up and down. The inputs for this vi are three arrays: starting magnetic field currents, ending magnetic field currents, and current step size. The enables a sweep consisting of any for the entire sweep both up and down.

It will accommodate a series of arrays of inputs for magnetic field sweep steps. For example, large step sizes save time at saturating fields, where small step sizes offer sensitivity around coercive fields. This vi outputs each value in the 3 arrays to MasterSSEViWithField-V2.vi and runs this vi as many times as there are rows to supply the current-control to the magnet. To determine how long this master vi will take to run (a full experiment), it calls SSECheckMagnetControlInputs.vi.

SSECheckMagnetControlInputs.vi

This vi determines how many steps in each magnet run array and adds them.

SSEdeterminePowerP-2400

Use this to determine current necessary to generate the appropriate $\triangle$ T across the island (or along the legs) for SSE/PNE experiments. For a given current, this vi measures the Rs for the hot island and the cold island. To convert to temperature, I use a calibration imported into origin, and interpolate the T(R) for each input current. This vi generates no output to file.

ShortSSETempsCalibration.vi

Input the base temperatures of interest for the given experiment. Output is T, R1, R2, R3.

AverageTheAverages.vi (Analysis)

This is a (slightly) manual way to average the bin-averaged data. It takes data points 25-35 and averages them. It doesn't take into account 20-24 and 35-39 to

allow the system to respond to heater cycling on and off. The MasterSSEHysteresisWithFieldV2.vi does this already This is a good vi to double check the in-experiment analysis.

Other SSE/PNE Experiment Vi's

MasterSSEHysteresisWithFieldV2-OneGradTOrientation.vi and MasterSSEWithFieldV2-OneGradTOrientation.vi are vi's for running SSE/PNE measurements for entire sweep up and down, but ror one orientation only (for example Both hot). It will accommodate different step sizes between magnetic field inputs. Finally, NVM-DriftCheck.vi is a very useful tool. This vi runs continuous measurements of both NVMs at once and plots them. It is excellent for checking noise or drift. Cancel out of write file option at the end of you dont want to save the data to a data file.

K and α Magnetic Field Sweep Experiments

Peltier Experiments

PeltierMultiCurrent.vi

This vi runs the basic Peltier experiment without magnetic field input. Inputs are beginning and ending film current with step size. The vi then measures the resulting Rs. This can be called as a sub-vi for either a temperature sweep or a field sweep.

PeltierHysteresis.vi

This vi runs the Peltier vs H experiment with + to - I input (similar to a resistance measurement). It calls PeltierMultiCurrent.vi and writes the data via the PeltierWriteToFile.vi.

FirstThermalKSRS_DUv5CalibrationOnly.vi

This vi is for running a calibration in order to convert Rs from Peltier experiments to Ts. This is a useful vi when running PeltierMultiCurrent.vi.

PeltierAnalysis.vi

This file takes the output from the PeltierHysteresis.vi and the FirstThermalKSRS_DUv5CalibrationOnly.vi (for R and T data). It converts Rs to Ts using interpolation and adds the Ts to the output file. It also adds the film resistance determined through the slope to the V/I fit.

PeltierAnalysisPart2.vi

This vi takes the output from PeltierAnalysis-OneCurrentFieldSweep.vi, should prompt the user for Kb and KLegs, and determines the Peltier power, Joule Power, and I^2R. (*This vi needs updating*.)

PeltierTemperatureDependence.vi

Runs just like the K experiment but for the Peltier coefficient. It calls the PeltierMultiCurrent.vi. Calibration is included in the data output from this file.

PeltierVsTemperatureAnalysis.vi

Analysis vi for the Peltier vs Temperature experiment. Inputs to the front panel include the number in each set of input currents, and the polynomial to try for temperature fits. This vi will determine T1, T2, and T3 and add these columns to the output file. There is an interim step between this analysis vi and the final analysis vi that determines the Peltier coefficient, (see the following section). After saving the output from this vi, import it into Origin using the "PeltierVsTemperature" template. The next step is to populate the Kb, KLegs, and I^2R columns in the worksheet. After this, set the column values for Peltier Power column. This will determine the power generated through the Peltier effect using the equation determined through the Peltier thermal model. After filling in all these columns, the final step is to export this worksheet as a .txt file. This file is the input for the PeltierVsTemperatureSummaryAnalysis.vi.

PeltierVsTemperatureSummaryAnalysis.vi

This vi performs the linear fit for each data set (at each temperature) and determines the Peltier coefficient from the slope. The output file includes magnetic field, T, Film R, and Pi.

Peltier_OneCurrent.vi

This runs a single Peltier experiment with only one current rather than a series of currents.

PeltierHysteresisOneCurrent.vi

This runs a Peltier vs H experiment where the Peltier effect is generated with only one input current. This vi calls the Peltier_OneCurrent.vi.

PeltierAnalysis-OneCurrentFieldSweep.vi

This file takes the output from the PeltierHysteresisOneCurrent.vi and the First-ThermalKSRS_DUv5CalibrationOnly.vi (for R and T data). It converts Rs to Ts using interpolation and adds the Ts to the output file. It also adds the film resistance determined through the slope to the V/I fit.

PeltierAnalysisPart2-OneCurrentFieldSweep.vi

This vi takes the output from PeltierAnalysis-OneCurrentFieldSweep.vi, prompts the user for Kb and KLegs, and determines the Peltier power, Joule Power, and I^2R.

AMR Experiments

AMR_Film_WithField.vi

Vi for the AMR experiment. This is actually just a film Resistance experiment since it doesnt adjust the magnetic field. Enter the input and final currents and the step size. The slope from the linear fit to V/I gives R for the film.

Master_AMR_Film_WithField.vi

This vi sweeps the field and calls the AMR_Film_WithField.vi at each field. The outputs to this vi are (1) AMR data and (2) raw data with the V and I inputs.

K(T) and α(T) Experiments

FirstThermalKSRS_DU_TEPandSkipV6.vi

This is the BIG vi that runs the K and α experiment as a function of temperature. This vi warrants a chapter in itself, but I'll summarize. It takes inputs: start temperature, end temperature, temperature step size, maximum input current, and the number of currents to apply. It records power data every 3 data points, and calibration data at every data point. Calibration data comes from measuring the Rs once equilibrium is reached for each reference temperature. For example, the step size between reference temperature is usually 2 K. Starting at 78K, the vi measures Rs for a calibration point (with no power) then measures Rs at each power step. A power step size is determined by dividing the maximum input current by the number of currents to apply, which is usually 10. At the end of the 78K data point, there should be 11 entries: 1 with no power data, and 10 tracking the effect of a given input current on the Rs. For the next two data points, at 80 and 82 K, the vi will only record calibration data. It will not record power data for these. This is the what the 'skip' in the vi title refers to. The sequence of taking power data every 3 steps saves time previously spent taking too much data. The experiment takes roughly 3 and 1/2 days using this current logic and if running uninterrupted.

ThermalPropertiesAnalysisV9.vi

This is the analysis vi for the thermal conductivity and thermopower measurements as a function of temperature. The input file is the data file from the FirstThermalKSRS_DU_TEPandSkipV6.vi. The outputs are R,T calibration files for each thermometer, KallPs2Is file, KbKlAll file, TEP file, polynomial fits for each thermometer, and thermometer sensitivity files. All output files are optional so that this vi can be run over and over again as the parameters for analysis are changed for the optimal analysis. There are additional parameters on the front panel to adjust the analysis including a choice between interpolation and a polynomial fit, converting to a log scale before a polynomial fit (for low temperature thermometry), a choice to calibrate in pieces and the number of points in each piece, and cutoffs to inspect fewer powers or to remove the smallest powers on the cold island. This vi will also run for a K experiment where the left island (rather than the usual right island) is heated. There is an option for the skip logic. This enables analysis of data before the skip logic as well as the skip logic data. This vi runs several large sub-vis for the data output. There are several tabs to keep track of the quality of the analysis. One of these is a 'residuals' tab. This is very useful to see if the polynomial fit is optimal. There is a 'Resistance Data' tab to inspect the RT arrays output by the vi and a 'T1, T2, T3 Calibration Fit' tab to inspect the T(R) plots and the polynomial fits applied. Note, if the raw data file includes range (most do after we started measuring the low temperature platforms), then the raw data must be rearranged to move the range columns to the end.

RearrangeRawDataPlusRange.vi

This vi is for moving the 3 range columns from the middle of the raw data sheet to the end of the worksheet. This must be run before the ThermalPropertiesAnalysisV9.vi if range columns are recorded in the raw data.

ResistanceWkshts.vi

A sub-vi for ThermalPropertiesAnalysisV9.vi. This separates the calibration data from the power data. Then it breaks the data file into R,T calibration files for each thermometer.

TvsPPolyInterpFitInPieces.vi

This sub-vi for ThermalPropertiesAnalysisV9.vi determines T1, T2, T3 by either interpolation or polynomial fit. In this version you can cut the whole data file into segments and use lower order polynomials to determine T(R). For example, rather than fitting a 9th order polynomial to calibration points from 78 to 326 K, you can cut the calibration points into 10 point segments and fit a 2nd or 3rd order polynomial to the data. Sometimes this improves the quality of the fits to the data as indicated through the residuals.

TvsPPolyInterpFitV2.vi

This sub-vi for ThermalPropertiesAnalysisV9.vi determines T1, T2, T3 by either interpolation or polynomial fit. This will apply the polynomial fits to the full temperature range.

MakeKallPowers2Islands.vi

This sub-vi for ThermalPropertiesAnalysisV9.vi makes the 'KallPs2Is' worksheet.

ThTsVsPslopes.vi

This sub-vi for ThermalPropertiesAnalysisV9.vi generates Th vs P and Ts vs P plots, calculates Kb and KLegs, calculates α, and the error for Kb and α. It puts all of these together to make the 'KbKlall' worksheet.

ScatterCorrectionAnalysis.vi

Sometimes the small amount of heat transported through the bridge or bridge and film in the first few powers is so small that the increase in temperature on the cold side is within the error bars of the temperature sensitivity. These few first data points can effect the slope of the cold temperature (T_s) versus power plot. The most important quantity in the determination of Kb is the slope of this linear fit so anything that throws off the slope will cause scatter in the data. This vi allows inspection of a single data point to determine the cause of scatter in a data set. The inputs for this vi are the KallPs2Is file and the reference temperature in question. It can be looped to look at more than one data point in a row. It outputs a shorter KbKlAll file with the corrected data points. I import this data file into origin and cut and paste into the worksheet in origin. That way I keep the original KbKlall text file and the scatter correct KbKlall text file unchanged for future reference.

K(H) and α(H) Experiments

KTEPonePoint.vi

This vi runs one power point for a K and α measurement.

Master_K-TEP_WithField.vi

This vi measures K and α vs H for a series of external magnetic fields. The inputs to determine the series of fields are input current (for magnet) end current (for magnet) and step size. The magnetic field selection logic is duplicated from the SSE/PNE experiments. This vi calls the KTEPonePoint.vi sub-vi. This is the OLD version. See improved version below.

Master_K-TEP_hysteresis.vi

This vi measures K and α vs H for an entire external magnetic field sweep up and down. It will accommodate different step sizes between magnetic field inputs. The magnetic field selection logic is duplicated from the SSE/PNE experiments. Note that these three vi's are early versions. They do not include the type of averaging and thermal drift corrections that the SSE/PNE experiments employ to increase the sensitivity of the experiments. This logic was added to the next set of K(H) and α(H) that I'll describe after presenting the analysis vi's for these experimental vi's. This is the OLD version. See improved version below.

AnalyzeK-TEPsweep.vi

This vi analyzes the magnetic field dependence for both the K and α measurements from Master_K-TEP_hysteresis.vi. This vi calls for R(T) files for each thermometer separately. I generate these from the FirstThermalKSRS_DUv5CalibrationOnly.vi raw data output. The 1st output data file: Field, K, Alpha, Alpha error. 2nd Data file outputs temperatures (optional). This is the OLD version. See improved version below.

KTEPonePoint-ZeroAveraging.vi

This vi runs one power point for a K and α measurement. It improves on the previous versions by adding the same quasi-AC logic used in the SSE/PNE experiments. So this vi subtracts off thermal drift and averages the bins to increase the signal-to-noise ratio.

Master_K-TEP_WithField-ZeroAveraging.vi

This vi runs a K and α measurement vs H for a series of fields with input current (for magnet) end current (for magnet) and step size. Quasi-AC method with thermal drift subtracted and bin averaging to increase signal-to-noise ratio. It calls the KTEPonePoint-ZeroAveraging.vi sub-vi.

MasterK-TEP_hysteresis-ZeroAveraging.vi

This vi measures K and α vs H for an entire external magnetic field sweep up and down. It will accommodate different step sizes between magnetic field inputs.

The magnetic field selection logic is duplicated from the SSE/PNE experiments. It includes the quasi-AC method with thermal drift subtracted and bin averaging to increase signal-to-noise ratio.

AveragedTEPsweep-averagedBinData.vi

Analysis vi for MasterK-TEP_hysteresis-ZeroAveraging.vi. This vi fits to thermal drift and subtracts off the drift contribution. Averages the Vs and does bin-averaging to determine K and α vs H.